UNIVERSITÀ DI SIENA 1240

Dipartimento di Biotecnologie, Chimica E Farmacia

Dottorato in

Scienze Chimiche E Farmaceutiche

XXXV ° Ciclo

Coordinatore/Coordinatrice: Prof. Maurizio Taddei

New strategies for the development of nano-engineered catalysts for Fuel Cells and Electrolysers

Settore scientifico disciplinare: *CHIM/03*

Candidato

Francesco Bartoli

Firma candidato

Francesco Bartoli
28.02.2023
14:34:58
GMT+01:00

Supervisore

Hamish Andrew Miller

Istituto di Chimica dei Composti Organometallici (ICCOM-CNR)

Co-supervisore

Francesco Vizza

Istituto di Chimica dei Composti Organometallici (ICCOM-CNR)

Anno accademico di conseguimento del titolo di Dottore di ricerca

2021/22

Università degli Studi di Siena
Dottorato in SCIENZE CHIMICHE E FARMACEUTICHE
XXXV ° Ciclo

Data dell'esame finale
10/03/23

Commissione giudicatrice

Oriana Tabarrini
Cecilia Pozzi
Nicolas Ferr

Supplenti
Vincenzo Summa

Contents:

1 Abstract

The continued depletion of strategic resources like fossil fuels, precious metals and other critical raw materials has put the world economy on the brink of a global crisis. Together with this, the continued emission of large amounts of greenhouse gases represents a significant challenge due to the effects of climate change. It is therefore imperative to find alternatives to fossil fuels that are sustainable, keeping in mind a full life cycle analysis. Clean technologies such as fuel cells and water electrolysis will be a fundamental part of the transition to renewable energy. In this context, a key role will be played by molecular hydrogen as “energy vector”. Thanks to its high specific energy density and clean combustion to water, H_2 represents a high-quality energy carrier and an ideal candidate to replace fossil fuels. Importantly, H_2 can be produced by water electrolysis and can be converted into electricity using Fuel Cells. However, low conversion efficiencies and high capital investment costs, still limit the use of these electrochemical technologies. The search for sustainable, stable and active electrocatalysts will play a key role in reaching the performance required for these devices. The development and characterisation of such materials is the subject of the research described in this thesis.

The first part of this thesis provides an introduction to the field, including a short overview of key electrochemical concepts, and a definition of the two types of devices that are studied, fuel cells and electrolysers, and their respective anodic and cathodic reactions (Chapter 2).

The synthesis and the chemical-physical characterization of all electrocatalysts is reported in Chapter 3. The electrochemical study of these materials in half-cells and their application in complete devices, are described in detail in Chapters 4, 5 and 6.

Chapter 4, describes a study of the effect of metal-CeO_2 interactions in carbon supported electrocatalysts on alkaline hydrogen oxidation and evolution reactions. A series of transition metal nanoparticle electrocatalysts (Pd, Ir, Ru and Rh) with a metal loading of 10 wt%, were prepared using two supports; carbon and carbon-CeO_2 (50:50). Each material is characterized using XRD, XPS, TEM and electrochemical tests, EIS and tafel analysis is performed in order to understand the HER and HOR activities. The presence of CeO_2 enhances the activity of Pd, Ir and Rh. Ruthenium has superior activity in term of mass activity, specific activity and i_0, both

for HER and HOR. The HOR/HER exchange current (i_0) of Ru/C has an average value of 106 A g_{Metal}^{-1}. Importantly, EIS and capacitance measurements show that CeO_2 promotes catalyst utilization and lowers ionic resistance.

Chapter 5 focuses on developing sustainable electrocatalysts for Anion Exchange Membrane Fuel Cells (AEMFC). In this study a high-performance Pd-CeO_2/C hydrogen oxidation reaction (HOR) catalyst is integrated into AEMFCs in combination with different Pt and Pt-free cathodes. A H_2/O_2 AEMFC peak power performance of 2 W cm^{-2} at 80 °C is obtained when using a Pt/C cathode (2 A cm^{-2} is achieved at a cell voltage of 0.6 V), which translates to 1 W cm^{-2} peak power density (0.7 A cm^{-2} is achieved at 0.6 V) at 60 °C with the switch to a cheap, critical raw material (CRM)-free Fe/C cathode catalyst.

In Chapter 6.1, a molecular catalyst for hydrogen evolution was developed and tested in a Polymer Exchange Membrane (PEM) water electrolyser. The dinuclear Ru diazadiene olefin complex, [Ru_2(OTf)(μ-H)(Me_2dad)(dbcot)$_2$], is shown to be an active catalyst for hydrogen evolution. When supported on high surface area carbon black and at 80 °C, [Ru_2(OTf)(μ-H)(Me_2dad)(dbcot)$_2$]@C evolves hydrogen at the cathode of a PEM electrolysis cell (400 mA cm^{-2}, 1.9 V). A remarkable turn over frequency (TOF) of 7800 mol_{H2} $mol_{catalyst}^{-1}$ h^{-1} is maintained over 7 days of operation. A series of model reactions in homogeneous media and in electrochemical half cells, combined with DFT calculations, are used to rationalize the hydrogen evolution mechanism promoted by [Ru_2(OTf)(μ-H)(Me_2dad)(dbcot)$_2$].

Lastly, in Chapter 6.2 the development of a non-precious metal cathode catalyst for Anion Exchange Membrane Water Electrolysis (AEMWE) is reported. This study investigates an active HER catalyst synthesized from $MoNiO_4$ nano-rod arrays on nickel foam using high-temperature reductive annealing. Complete characterization of the nanostructure by SEM, HR-TEM and XPS indicates that during synthesis the crystalline $MoNiO_4$ structure of individual rods segregates a surface enriched polycrystalline MoO_2 layer rather than a Ni_4Mo alloy as reported previously. Mo and Ni electrochemical dissolution was studied by the scanning flow cell technique coupled with inductively coupled plasma mass spectrometry (SFC-ICP-MS). It was found that only Mo undergoes detectable dissolution phenomena, with the MoO_2/Ni cathode prepared at 600°C being the most stable. Tests in an AEMWE with a Ni foam anode demonstrate a current density of 0.55 A cm^{-2} (2 V) at 60 °C and H_2 production was stable for more than 300 h (0.5 A cm^{-2}). The synthesis procedure was scaled up to

prepare electrodes with an area of 78.5 cm^2 that were employed and evaluated in a three-cell AEM electrolyser stack.

In conclusion, the research described in this thesis demonstrates how engineering at the nanoscale can be used to improve the electrocatalytic activity and stability of sustainable catalytic materials for both fuel cells and electrolysers. The work conducted here has also gone beyond the study of materials on a lab scale, describing the scale up and application of electrocatalysts in actual devices.

2 Economic development, energy and environmental impact

The enormous human development over the last two centuries in the medical, technological, chemical and physical fields has resulted in unprecedented economic growth on a global level, which has managed to bring for the first time on such a large scale, well-being and comfort to millions of people; an absolutely non-trivial result, considering the average standard of living of previous centuries.

While on one hand there have been improvements in various aspects of society, on the other hand it is equally true that new types of problems have arisen with which humanity had never had to deal with; the speed with which these changes took place did not allow us to think about the consequences that the impact of mankind was having on the environment. In fact, in order to maintain this new lifestyle, the necessary resources required increased more and more over the years, consequently energy consumption became more and more important. To overcome this, the resources that man had defined as the main sources of energy had to be exploited in an increasingly intensive way, among which the most used was that deriving from fossil fuels[1].

The use of fossil fuels as a source of energy in the vast majority of human activities (machines, factories, etc.) has had, and is resulting in, the release into the atmosphere of large quantities of fine particles, nitrogen oxides and CO_2.

CO_2 is a greenhouse gas, or a substance that once released into the atmosphere, absorbs infrared radiation emitted by the sun, and re-emits it towards the Earth, thus causing a warming of the earth's surface, and preventing its normal cooling cycle. Other greenhouse gases released by combustion are: water vapor, methane (CH_4), nitrogen monoxide (N_2O) and ozone (O_3). The effect of these substances does not depend only on the quantity that is released into the atmosphere, but also on their "global warming potential" (GWP). GWP is a measure of how much heat can trap 1 ton of gas in the atmosphere for a given period, relating to the release of 1 ton of carbon dioxide (CO_2); for example, methane has a GWP of 23 and nitrogen monoxide of 296 [2,3].

With the industrial revolution that took place in the 18th century, human activities became more and more intense, pouring more and more greenhouse gases into the atmosphere. As a result, this phenomenon has had and is having a global impact that has led to a slow but steady rise in temperatures ever since.

The increase in global mean temperature partly affects what are described as Climate Change. They are defined as variations in the earth's climate, i.e. variations in the average values, on different time scales, of environmental and meteorological parameters: temperature, rainfall, cloud cover, ocean temperature, the distribution and development of plants and animals.

The earth's climate is naturally subject to changes of this type, as evidence dating back to the past eras of the Earth show us, however it has been shown how the intervention of man has altered these balances, the spread of violent meteorological phenomena, temperatures well above the norm, and the melting of glaciers are all effects that are occurring and that can be attributed to human activity and their impact on the ecosystem.

To tackle this problem, it is therefore necessary that the production of energy is carried out in the most sustainable way possible, making the most of the renewable resources that we possess. Since the 1970s the concept of sustainability [4] has entered the common vocabulary among those who dealt with finding a system to replace the classic exploitation of terrestrial resources, it has been defined as a "balance between the satisfaction of present needs without compromising the possibility of future generations to make up for their own ".

Returning to renewable resources, many of them originate from the impact of solar radiation on the Earth. For example, the wind comes from thermal convection and currents, hydroelectricity from hydrological cycles (rain and evaporation), and finally biomass is created through photosynthesis which promotes the conversion of CO_2 into polysaccharides such as cellulose and other plant substances.

It is therefore possible to obtain energy from these sources using different types of technologies, photovoltaic panels, wind turbines, hydroelectric plants, etc. The big disadvantage is given by the fact that they have characteristics that make it difficult to use them planned over time, for example photovoltaic depends a lot on the presence of clouds in the sky, operating at full capacity only on clear days, or wind power that needs to be installed in places with constant winds almost all year round. The electricity produced with these systems cannot be stored (or in any case it is difficult), so it must be used immediately; what was thought was precisely to find a means in which to store the excess energy collected from these sources, providing a more reliable supply to the energy system[4,5]. Together with this, the aim of research is also to lower the costs of these solutions, in order to make them competitive in the market.

2.1 Hydrogen: starting point for a new society

Although the listed advantages of renewables may seem like a solution to the world's problems, a hydrogen-based economy seems to be the best solution today.
Hydrogen is an energy carrier that has many advantages, it has a high specific energy density (122 kJ / g about three times that of fossil fuels), it can be produced through the electrolysis of water, which is an abundant resource on Earth, and can be easily converted back into energy through fuel cells, by an oxidative process, simply obtaining water as a final product. Hydrogen is widely used in strategic sectors such as ammonia production, steel production, and the pharmaceutical industry. In 2020, hydrogen demand has approached 90 Mt and this will increase over the coming years[7].
The so-called "Hydrogen Economy"[8], is an economic model, within which various types of energy are conserved in the form of the hydrogen molecule, which can be reused for means of displacement, as a supplement to the electricity grid or to compensate for any energy drop.
Hydrogen does not exist in nature in the gaseous state, except in small percentages in the atmosphere, but is combined with other elements, based on this it is possible to distinguish 2 main production methods:

1) steam reforming of methane: from non-renewable fossil based resources
2) electrolysis of water: using renewable energy

The first case is an industrial process that satisfies up to 96% of world hydrogen needs, using methane extracted from oil fields. The H_2 obtained, is used mainly for the refining of oil and the production of ammonia, from which then urea is produced for fertilizers. The main problem is due to the fact that steam reforming produces large quantities of CO_2, which we have said to be one of the main greenhouse gases, this combined with the fact that methane is not a renewable source, has led scientists to completely re-evaluate production and identify a "greener" source that does not have problems of availability. Figure 2.1 lists the the main contribution to the CO_2 emission defined by energy source.

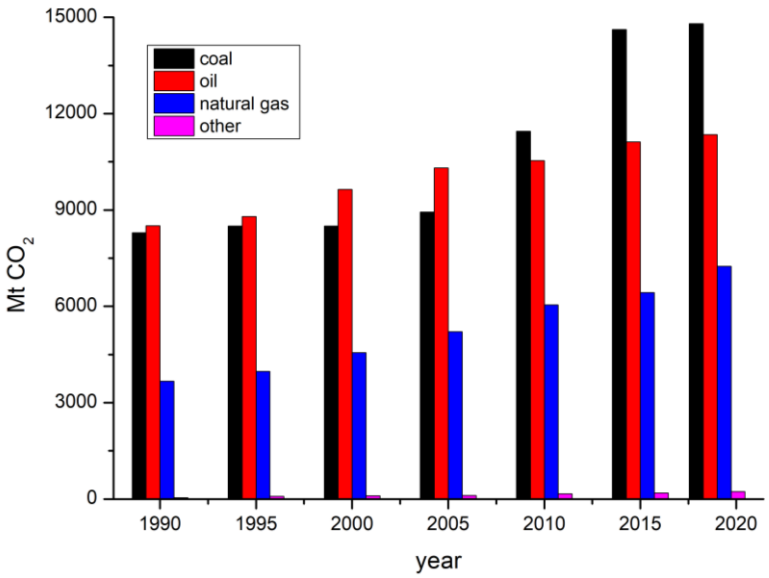

Figure 2.1: CO_2 emissions by energy source, World 1990-2019 (https://www.iea.org/).

The electrolysis of water represents a sustainable alternative; and many efforts are being made in devising new processes to replace the classic ones, such as using the energy obtained through photovoltaics in the electrolysis process; but in general, the obstacles that still prevent these technologies from gaining the upper hand are the low conversion efficiencies, and the high capital investments required. To make competitive the production of green hydrogen with respect to other sources such as coal, methane, etc. (Figure 2.2), the U.S. DOE (Unite States Department of Energy), has stated that the cost of H_2, must go from the current 7 USD/kg to 2 USD/kg by 2025, and finally 1 USD/kg by 2030.

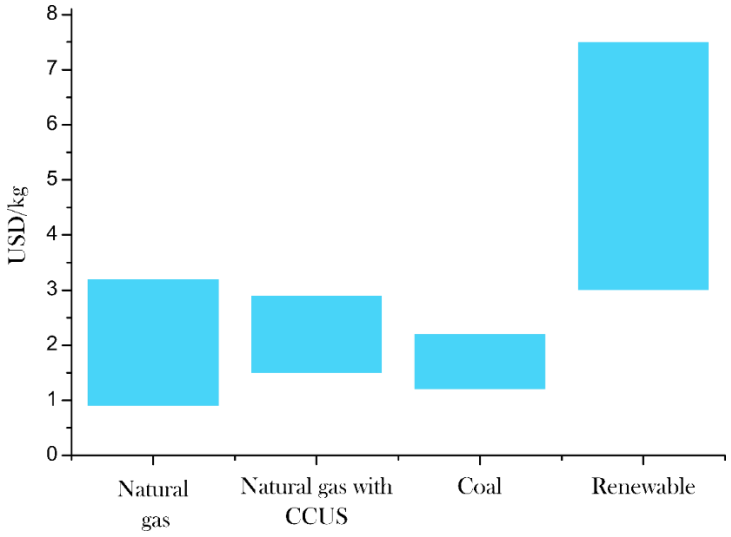

Figure 2.2: hydrogen production costs (USD/Kg) by production source, 2020. (https://www.iea.org/data-and-statistics/charts/hydrogen-production-costs-by-production-source-2018).

The other significant challenge of hydrogen economy is the development of a low-cost storage and transport system. Currently, hydrogen can be stored as a compressed gas (up to 800 bar) and as a liquid in cryogenic containers (at 21 °K), adsorbed on materials with a high surface area, or chemically bonded in various types of compounds, such as metallic hydrides. On the other hand, up to 20% and 40% of the energy contained in hydrogen is spent on compressing and liquefying the gas respectively, to which are added all the safety problems related to the transport of high-pressure and highly flammable gases. The best solution seems to be chemical storage, thanks to which it is possible to store large quantities of fuel, in a safer way and without exceedingly too much weight. However, further studies must be done to improve the storage properties of the materials, allowing good reversibility of the loading and unloading cycles at moderate temperatures, fast hydrogen release kinetics, and finally durability over time. Returning to the possible uses of hydrogen, as already mentioned, as well as to produce ammonia and oil refining, the transport sector could represent a fertile ground for this type of technology. Unlike traditional engines, in which much of the energy deriving from the combustion of petrol, diesel oil, etc. is lost in heat, in an engine based on fuel cell technology, the free energy of the reaction between H_2 and O_2 would be exploited directly, significantly increasing the efficiency, and not producing any type of pollutant.

To date, however, although many devices have been created and work, there are still three main obstacles to the development of the hydrogen economy:

- Reduction of costs for H_2 production
- Development of new H_2 storage systems
- Cost reduction of fuel cells

2.2 Catalysis

Before tackling the electrochemical part, it is good to introduce some concepts concerning catalysis and the role of catalysts in the chemical processes to be considered; as they decorate the surfaces of the electrodes, anodes and cathodes, in which the redox reactions take place which are fundamental for the development of the technologies that this thesis discusses, thus constituting a fundamental part of electrochemical cells.

A catalyst can be defined as a substance that increases the reaction rate but is not consumed by it; they are generally divided into two categories: homogeneous and heterogeneous. In the former the catalyst is in the same phase as the reactants, while in the latter it is formed by a support that can assist the activity or remain inert, the real catalyst is present above it; since the systems used in electrochemical cells are heterogeneous, and from now on reference will be made exclusively to them.

The fact that the speed of the reaction is increased is attributable to the fact that through catalysis a different reaction pathway is provided which has a lower Gibbs free energy of activation ($\Delta G^{\ddagger}$).

It is good to specify that the $\Delta G^{\ominus}$ of the total reaction is not changed, since G is a state function; in fact, as can be seen from the Figure 2.3, the $\Delta G^{\ominus}$ is the same in both energy profiles, precisely for this reason a thermodynamically disadvantaged reaction cannot be favored by catalysis, this is because a catalyst acts only on the reaction kinetics.

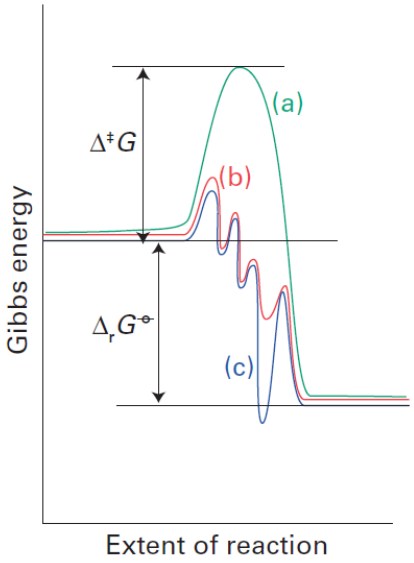

Figure 2.3: schematic representation of the energy profiles of a reaction. The non-catalyzed reaction (a) at a higher $\Delta G^{\ddagger}$ than that present in the catalyzed one (b). The Gibbs energy of the total reaction $\Delta G^{\ominus}$, is the same for the way (a) and (b). Curve (c) shows the profile of a more stable intermediate of the product[9].

Figure 2.3 shows how the energy profile of (b) (catalyzed reaction), has a much lower activation energy, this results in the presence of a peak significantly lower than that of (a), and the presence of more relative maxima, which indicate precisely how the process has taken a completely different path, but which in the end leads to the same products, and at the same time lowering the activation energy.

As can be seen from the curves, one or more types of intermediates can be formed during the process, depending on the complexity of the reaction, therefore another important aspect can be introduced because of this, namely the stability of the intermediates. In fact, if they are too stable, they prevent the catalyst from regenerating and releasing the product, in this way they are unable to accept fresh reagent to transform it, and as can be seen in curve (c), there is an absolute minimum which means that the whole process is blocked. This process is called "poisoning" and may also be due to by-products of the reaction, side reactions or other substances present in the reaction environment, in any case the result is the deactivation of the catalyst and the interruption of the catalytic cycle.

A good catalyst must therefore be able to withstand as many cycles as possible before being deactivated forever, the number of possible cycles that can be performed can be expressed with the so-called "turnover number" TON:

TON (Homogeneous cat.) = moles product/moles catalyst

TON (Heterogeneouss cat.) = moles product /n° active sites or surface area

Determining the number of active sites on a heterogeneous system is particularly difficult, in fact it is often preferred to consider the surface area.
The other fundamental aspect lies in the catalytic efficiency, or having a high conversion rate, even at low concentrations of catalyst; this is expressed with the "turnover frequency" called TOF:

$$TOF = \frac{v}{[Q]}$$

Where v is the reaction rate, and [Q] the concentration of the catalyst. A good catalytic system will therefore possess very fast kinetics even at low Q concentrations, resulting in a higher TOF. Finally, the last fundamental requirement of a good catalyst is its selectivity, for example from the oxygen reduction reaction (see paragraph 1.3.3), it is possible to obtain both water and hydrogen peroxide depending on the number of electrons exchanged, if H_2O is the product of interest, a good catalyst will favor its formation, rather than H_2O_2.
Catalysts have been used for many years, and there are a huge variety of them, for many types of applications, in this thesis work, those used in electrochemical cells will be analyzed. They usually consist of a noble metal, dispersed on the surface of a conductive support in order to increase the surface area, and therefore the contact with the fuel; the cost of these metals usually belonging to the "Platinum Group Metals" (PGM) is very high, relegating the use of these devices to purely academic purposes, in the aerospace sector, or other niche uses, but not for large distribution.
In recent years, enormous efforts have been made in the field of research, aimed precisely at eliminating these intrinsic problems, the decrease in metal loading, or better still the complete removal of precious metals are the most coveted goals in this sense. Furthermore, with the birth of nanosciences, it was possible to engineer these materials on a nanometric scale, thus exploiting their peculiarities to improve catalytic activity.
Unfortunately, however, if on the one hand these materials appear to be very promising, on the other hand they also suffer from some problems, mainly due to their low stability and loss of efficiency during cycles, which make them not yet usable on a

large scale. Moreover, very often their synthesis is also quite complex. At present, therefore, efforts are concentrated on developing highly stable materials that are easy to produce and have affordable costs.

2.3 Electrochemical technologies

2.3.1 Key concepts: Electrochemical cell and reactions

Fuel cells and electrolysers are electrochemical cells, the former converts chemical energy (the free energy of a spontaneous chemical reaction) into electrical energy, and the latter makes the exact opposite converting electrical energy into chemical transformations.

The most important electrochemical reaction for fuel cells is the combination of molecular hydrogen and oxygen to form water, on the contrary, for electrolysers it is the transformation of water into elementary hydrogen and oxygen. The trick of electrochemistry is splitting these reactions into two half-reactions, an oxidation reaction and a reduction reaction, which can occur respectively in distinct regions of the cell, called anode and cathode. Ultimately, we have four half-reactions:

- Hydrogen oxidation reaction (HOR)
- Hydrogen evolution reaction (HER)
- Oxygen reduction reaction (ORR)
- Oxygen evolution reaction (OER)

Each of these will be extensively discussed in the next paragraphs 2.3.2 and 2.3.3.

Another fundamental point of electrochemical cells is to determine their behavior as either a fuel cell or an electrolyser, that is to understand if the cell will produce electrical energy or energy will be required for its supply. In this context, thermodynamic principles play an important role, leading to the definition of the most famous law of electrochemistry, namely the Nernst equation. This law defines the maximum obtainable energy from a fuel cell, or the minimum energy supply required to power an electrolyser. In fact, if we consider the reaction of water formation:

$$\boldsymbol{H_2 + \frac{1}{2} O_2 \rightarrow H_2O} \qquad \text{Eq. 2.1}$$

the associated standard Gibbs free energy (ΔG^0) is -237.2 kJ mol^{-1}, and according to thermodynamic rules this means that the overall reaction is spontaneous. Starting from

the Gibbs free energy is possible to calculate a cell standard potential of 1.23 V as follows:

$$\boldsymbol{E^0 = -\frac{\Delta G^0}{nF}} \quad \text{Eq. 2.2}$$

This means that an electrochemical cell, where H_2 and O_2 are respectively fed (in standard conditions of 1 atm and 298 K) to the anode (for the HOR) and the cathode (for the ORR), gives a maximum voltage of 1.23 V. When there are not standard conditions, the cell potential is calculated through the Nernst equation (Eq. 2.3), which also considers the dependence of the potential on other parameters such as product and reagent activities, the effective temperature and the pH, when H^+ or OH^- species are present in the reaction. In this specific case, liquid water activity is conventionally equal to 1, and H_2 and O_2 activity can be approximated to their partial pressures. Altogether, an increase of partial pressure, temperature and pH cause a more positive potential of the cell, which corresponds to a more spontaneous reaction.

$$\boldsymbol{E = E^0 - \frac{RT}{2F} ln \frac{1}{pH_2 pO_2^{1/2}}} \quad \text{Eq.2.3}$$

The cell standard potential can be also considered as the sum of the half-cell standard potentials. As it is not physically possible to define an absolute potential scale for half reactions, their values are all referred to the so-called standard hydrogen electrode (SHE) that has a conventional 0 V value. The standard electrochemical cell potential (ΔE^0) for water formation is equal to:

$$\boldsymbol{E^0_{H_2O} = E^0_{\frac{O_2}{H_2O}} - E^0_{\frac{H^+}{H_2}} = 1.23\,V - 0.00\,V = 1.23V} \quad \text{Eq. 2.4}$$

The same thermodynamic reasoning is valid for the water splitting reaction into hydrogen and oxygen. In this case, the Gibbs free energy has a positive value (+237.2 kJ mol^{-1}), indicating a non-spontaneous reaction and the behavior of the cell is as an electrolyser. This cell, with OER to the anode and HER to the cathode, will be characterized by the same theoretical cell potential ΔE^0 of 1.23 V [10]. A schematic illustration of a water-splitting electrolyser and a fuel cell, with the respective reactions is represented below:

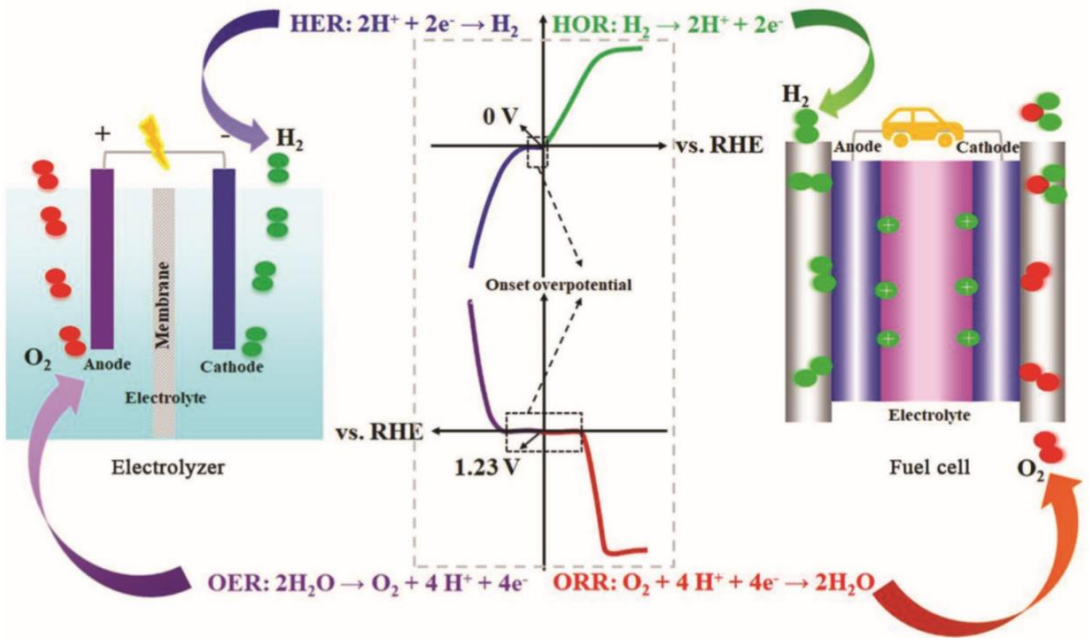

Figure 2.4: Scheme of a water-splitting electrolyser (left) and a fuel cell (right) and the corresponding reactions and potential values. [11]

In practice, because of the large kinetic energy barriers of the four fundamental reactions (HER, OER, HOR and ORR), the theoretical value of 1.23 V is not obtained. This causes a lower cell voltage output in fuel cells (generally E < 0.9 V) and the need for higher input voltage (E > 1.5 V) in the case of water electrolysers[11].

2.3.2 Hydrogen Oxidation and Evolution Reactions

As explained in the previous chapter regarding the hydrogen economy, this molecule, thanks to its high energy density, is considered a promising candidate for substituting fossil fuels. For this reason, research in hydrogen production through water electrolysis and its exploitation through oxidation in fuel cells has been very intensive.

The two related hydrogen electrochemical reactions are the HER and the HOR. The kinetics of the HER, the cathode reaction in electrolysers, and HOR, the anode reaction in fuel cells, are fast if compared to the more sluggish oxygen reactions, OER and ORR. At present, the best electrocatalyst materials for these reactions are Platinum group metals (PGM).

The HER can occur both in acidic (Eq. 2.5) and alkaline (Eq. 2.6) environments as shown in the following equations:

$$H^+ + e^- \rightarrow \frac{1}{2} H_2 \quad \text{Eq. 2.5}$$

$$H_2O + e^- \rightarrow \frac{1}{2}H_2 + OH^-$$ Eq. 2.6

The comprehensive study of the HER reaction mechanism has led to the identification of two possible pathways: the Volmer-Tafel and the Volmer-Heyrovsky. The first step for both pathways is the Volmer reaction, which is the hydrogen adsorption on the metal of the electrocatalyst (Eq. 2.7 and 2.8). After the first step, two adsorbed hydrogen atoms can react together through the Tafel reaction Eq. 2.9 (first pathway), or an adsorbed hydrogen atom reacts with a free water molecule or a proton according Heyrovsky reaction Eq. 2.10 and 2.11 (second pathway).

Tafel analysis is widely used to evaluate and compare HER activities of different

Volmer step

$$M + H^+ + e^- \rightarrow M - H_{ads}$$ Eq. 2.7 *acidic media*

$$M + H_2O + e^- \rightarrow M - H_{ads} + OH^-$$ Eq. 2.8 *alkaline media*

Tafel step

$$2(M - H_{ads}) \rightarrow 2M + H_2$$ Eq. 2.9

Heyrovsky step

$$M - H_{ads} + H^+ + e^- \rightarrow M + H_2$$ Eq. 2.10 *acidic media*

$$M - H_{ads} + H_2O + e^- \rightarrow M + H_2 + OH^-$$ Eq. 2.11 *alkaline media*

electrocatalysts. This analysis consists of acquiring linear sweep voltammetries (LSVs) with a rotating disk electrode (RDE) at low scan rates. The resulting data, plotted as log (i_k) vs. overpotential (η), represents the typical Tafel plot. The fitting of the linear portion of the curve corresponds to the Tafel equation, from which it is possible to extrapolate important electrochemical parameters, the Tafel slope (b) and the exchange current (i_0).

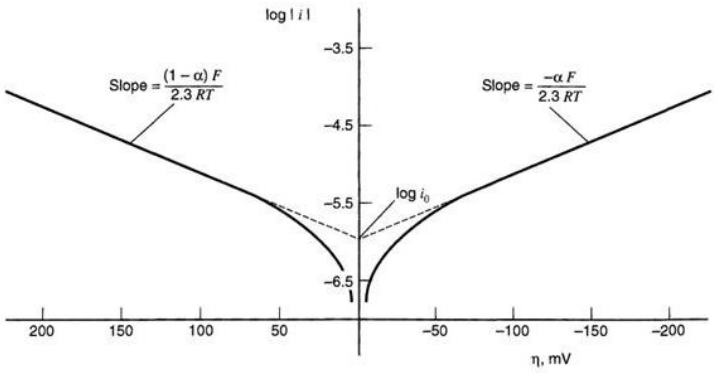

Figure 2.5: Tafel plot for anodic and cathodic branches, with the respective Tafel slopes and the exchange current as intercept of the linear fitting.

The Tafel slope has a different value depending on which of the three steps listed above is the rate determining step (RDS). When the Volmer reaction, the common step of the two mechanisms, is the RDS, the Tafel slope assumes a value of 120 mV dec^{-1}. If Tafel or Heyrovsky step are the RDS, the Tafel slope has a lower value of 30-40 mV dec^{-1} [12].

The exchange current represents the common absolute value of anodic and cathodic currents when the system is at equilibrium; this is a kinetic parameter, and the larger it is the faster the reaction will occour[10,12].

All of these considerations are also valid for the HOR. The mechanism of hydrogen oxidation is the same as for the HER, but the reactions happen exactly in reverse, so in this case Heyrovsky or Tafel step is followed by the Volmer step.

2.3.3 Oxygen Evolution and Reduction Reaction

Electrochemical oxygen reactions are either the reduction (ORR) or the evolution from water oxidation (OER), and they occur respectively at the cathode of fuel cells and the anode of electrolysers. In particular, the kinetics of the ORR is very sluggish, and this is a very crucial point for the energy efficiency of fuel cells. At date, the best electrocatalyst for this cathode reaction is platinum[13,14], but because of its high cost, research is focused on developing alternative catalysts, less expensive and more available. The mechanism of the ORR is very complex and includes different possible pathways, as described in the scheme below, to form either water or hydrogen peroxide as final molecules.

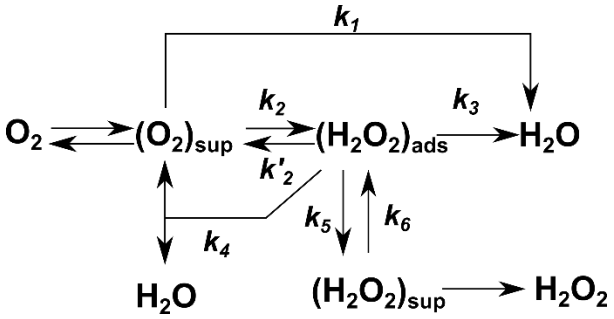

Figure 2.6: Scheme of the possible pathways for ORR to water or hydrogen peroxide. [10]

Oxygen reduction can proceed through a two-electron process to hydrogen peroxide or through a four-electron pathway leading to water.

Rotating disk electrode (RDE) and Rotating ring-disk electrode (RRDE) methods are very common voltammetry techniques used to establish the number of exchanged electrons during ORR, and especially the RRDE is very useful to obtain quantitative information about the amount of hydrogen peroxide formed with respect water. After acquiring LSVs at a slow scan rate and different rotation speeds (ω), it is possible to build a Koutecky-Levich plot, which shows the correlation between $1/i_k$ (at a given chosen potential) *vs.* $\omega^{-1/2}$. According to the Levich equation:

$$\frac{\mathbf{1}}{\boldsymbol{i}} = \frac{\mathbf{1}}{\boldsymbol{i_k}} + \left(\frac{\mathbf{1}}{\mathbf{0.620}\boldsymbol{nFAD}^{\mathbf{2/3}}\boldsymbol{\nu}^{\mathbf{-1/6}}\boldsymbol{C}}\right)\boldsymbol{\omega}^{\mathbf{-1/2}} \quad \text{Eq. 2.12}$$

c (concentration of O_2) = 1.03 x 10^{-3} mol dm^{-3}

D (diffusion coefficient) = 2.1 x 10^{-5} cm^2 s^{-1}

v (kinematic viscosity) = 1.07 x 10^{-2} cm^2 s^{-1}

ω (angular frequency of rotation) = rad s^{-1}

i_K (current in absence of any mass-transfer effects) = C s^{-1}

F (Faraday constant) = 96485 C mol^{-1}

A (electrode area) = 0.1963 cm^2

it is possible to calculate n, the exchanged current during the reaction, from the slope of the plotted curve. So, it is possible to understand if hydrogen peroxide (n=2) or water (n=4) or a mix of the two molecules (2 < n < 4) is electrochemically formed[15].

2.4 Electrochemical Devices: Electrolysers and Fuel Cells

2.4.1 Water electrolysers for hydrogen generation

Water electrolysis is the most popular alternative to the production of hydrogen from fossil fuels. What makes electrolysis so appealing, is the possibility to use renewable energy sources for pure hydrogen production (99.999% assay). Electrochemical splitting of water is a simple process where two electrodes, the anode, and the cathode, are connected to a direct current (DC) supply (electronic conduction) and submerged in a liquid electrolyte (ionic conduction). When a suitable cell voltage (E > 1.23V) is applied to the cell (see paragraph 1.3 for thermodynamic considerations), the non-spontaneous water splitting reaction can occur, producing hydrogen (HER) at the cathode (negative electrode) and oxygen (OER) to the anode (positive electrode).

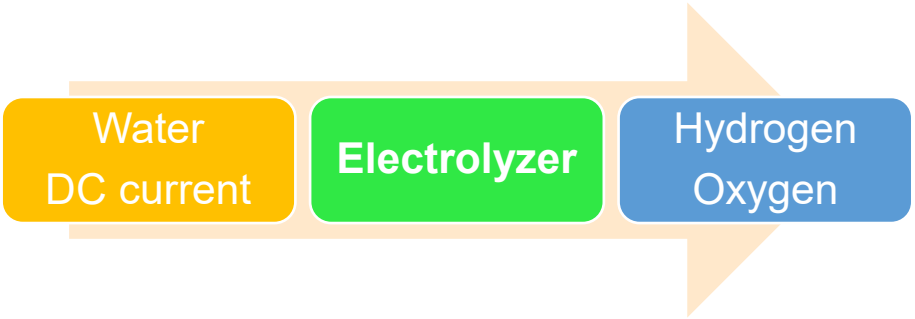

Figure 2.7: Schematic representation of an electrolyser.

Under real operating conditions, an electrolyser suffers from different irreversible losses, including (I) activation overpotentials at the anode (η_{an}) and cathode (η_{cath}), (II) ohmic drops (iR_a) from both ionic and electronic conductors, (III) concentration overpotentials at both electrodes mostly due to mass transport limitations but also to bubble formation. All of these losses in the electrolyser lead to an extra energy request for water decomposition, with a typical cell voltage of 1.8 - 2 V and a respective energy consumption of about 50 kWh for kilogram of hydrogen produced. The real performance of an electrolyser, that considers the different losses, can be represented with a current density versus cell voltage diagram as in Figure 2.8. [10,16.]

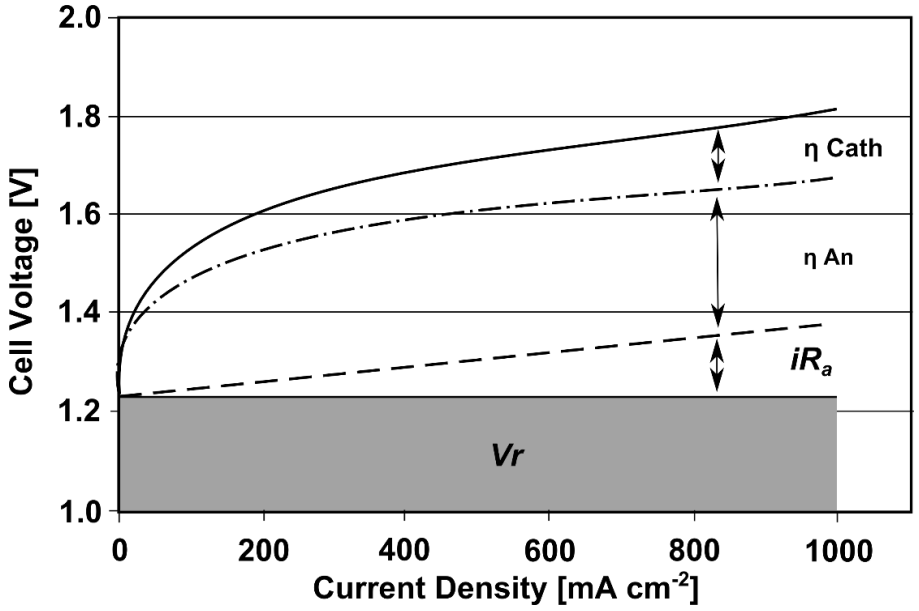

Figure 2.8: Typical current density versus cell voltage diagram of an electrolyser. [10]

We can distinguish different electrolysis processes according to the type of electrolyte used in the electrolyser, the most important are alkaline electrolysis and proton exchange membrane (PEM) electrolysis[16,17].

In particular, in acidic or neutral media, water electrolysers performance is affected by sluggish OER kinetics at the anode, where there is also the need of precious metal oxides as catalysts. For alkaline water electrolysis, less expensive catalysts, such as Ni-based alloys for HER, and transition metal oxides for OER can be used[18].

1.4.2.1 Proton Exchange Membrane Water Electrolysers

Proton exchange membrane electrolysers (PEME) (Figure 2.9) are the best low temperature devices for water splitting into hydrogen and oxygen, operating at a current density of 2000 mA cm^{-2} and a voltage of 2.1 V at 90 °C. Due to the extreme anodic conditions of high potential and low pH, there are some restrictions in the choice of the cell materials, so the typical used catalysts are IrO_2 and RuO_2 for the anode and Pt for the cathode. An acidic membrane, Nafion™ 117 manufactured by DuPont, is used as solid electrolyte to conduct protons (H^+) from anode to cathode and separate the gaseous hydrogen and oxygen produced. An advantage of these devices is the possibility to have high pressure on the cathode side while the anode works at atmospheric pressure[17].

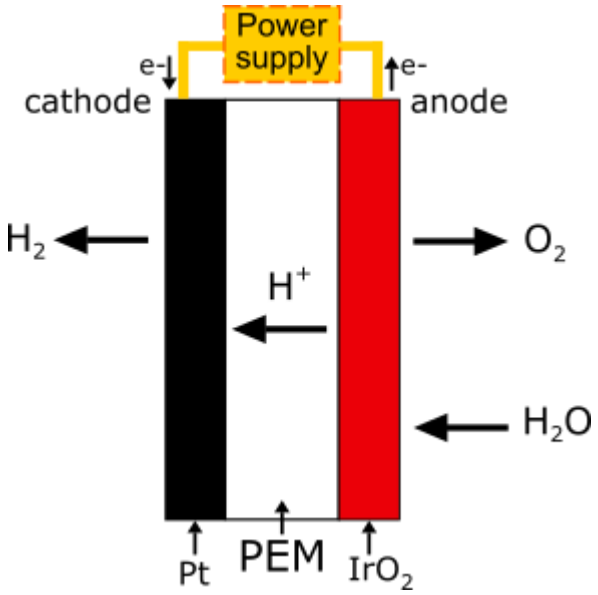

Figure 2.9: Schematic representation of a typical Proton Exchange Membrane Electrolyser.

1.4.2.2 Alkaline Water Electrolysers

Alkaline water electrolysis is a well-known technology. Alkaline electrolysers use cheap electrode materials, such as mixed Ni-Co oxides for the anode, and different Ni-alloys for cathode. The electrolyte is a concentrated KOH solution; this circulates through the electrodes separated by a porous diaphragm, which avoids the mixing of hydrogen and oxygen and guarantees the conduction of hydroxyl ions (OH^-) from cathode to anode. The diaphragms are made of ceramic oxides (asbestos and potassium titanate), or polymers (polypropylene and polyphenylene sulfide). Typical operating conditions of such devices are moderate temperatures of 70–90 °C, a current density of about 400 mA cm^{-2} and a cell voltage of 1.85–2.2 V, and a final conversion efficiency of 60–80%. Over the last few years, polymeric anion exchange membranes (AEM) based on ammonium ion-exchange-groups have been developed for electrochemical devices. The replacement of the diaphragm in the water electrolyser with an AEM offers some advantages, such as a lower cost with respect to the more expensive Nafion-based membranes in PEM, the use of low concentrated KOH solutions, so the absence of leaking caused by corrosive liquid electrolyte, volumetric stability, and handling for reduced sizes. The performance of a state-of-the-art AEM water electrolyser is of 530 mA cm^{-2} at 1.8 V with a lifetime of only 1000 h; it is for this reason that other studies are necessary to improve their efficiency and durability[16,17].

2.4.2 Fuel Cells for electricity generation

A fuel cell is an electrochemical device that converts the free energy of a spontaneous chemical reaction directly into electricity and heat. Fuel cells are closely related to batteries, but unlike these, they work using fuels that are provided to them from outside; while, batteries carry the reagents they need with them. The interest in fuel cells is due to their higher energy efficiency than typical thermal processes used to produce electricity, which are subjected to the Carnot cycle limitations. In fact, the best efficiency of a modern heat engine is about 50%, in a fuel cell this value is as high as to 70%[19].

Figure 2.10: Schematic representation of a fuel cell.

The most common fuel for these devices is H_2 that is oxidized at the anode (negative electrode), while methane or alcohols can also be used[20,21]. Pure or atmospheric oxygen are the oxidant species used at the cathode for the reduction reaction (positive electrode). The two electrodes are separated by an intermediate electrolyte membrane that alloys the flow of only ions (H^+ or OH^-) and acts as an insulator for the electrons that move through the external electrical circuit.

There are several types of fuel cells, classified according to the electrolyte and fuel in six major groups[22]:

- Proton exchange membrane fuel cells (PEMFC):
  - Direct formic acid fuel cells (DFAFC);
  - Direct ethanol fuel cell (DEFC).
- Alkaline fuel cells (AFC):
  - Proton ceramic fuel cells (PCFC);
  - Direct borohydride fuel cells (DBFC).
- Phosphoric acid fuel cells (PAFC).
- Molten carbonate fuel cells (MCFC).

- Solid oxide fuel cells (SOFC).
- Direct methanol fuel cells (DMFC).

These are further divided based on the operating temperature in:

- Low operating temperature (50-250 °C), including PEMFC, AFC and AFC.
- High operating temperature (650-1000 °C), like MCFC and SOFC.

The maximum operating cell voltage of fuel cells is for thermodynamic reasons lower than 1.23 V (see paragraph 2.3.1); due to their low output voltage, it is necessary to stack together different cells to increase their power capacity. The thermodynamic efficiency of the cell depends on the fuel, water management and the temperature; while the electrical efficiency depends on, as seen for electrolysers, ohmic, activation and concentration losses[22].

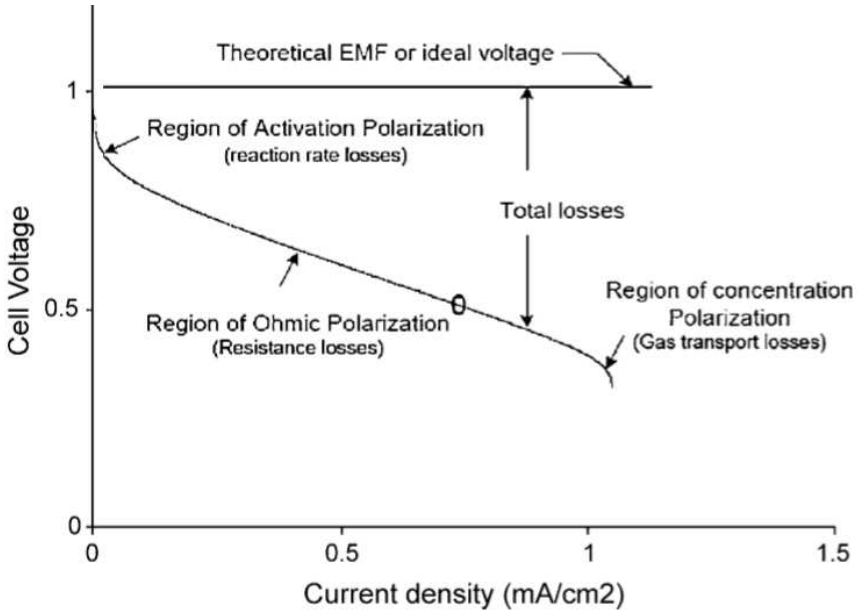

Figure 2.11: Typical fuel cell polarization curve [22]

2.4.2.1 H2/O2 Polymer Electrolyte Membrane Fuel Cells (PEMFC)

The H_2/O_2 fed PEM fuel cells, as PEM electrolysers previously described, use a polymer membrane as solid electrolyte to transport the proton (H^+) from anode to cathode, acting at the same time as an insulator for electrons. The cell (represented schematically in Figure 2.12) requires hydrogen and humidified oxygen gases to work, and so, since it contains water, the operating temperature must be under 100 °C. This characteristic combined with the light structure of the cells makes this technology very appealing for transportation and other commercial applications. Amongst the disadvantages, there are low efficiencies in the range of 40-60 % and the use of

platinum as catalyst for both electrodes. The use of very pure hydrogen is also required because of the intolerance of Pt to carbon monoxide poisoning[19,22].

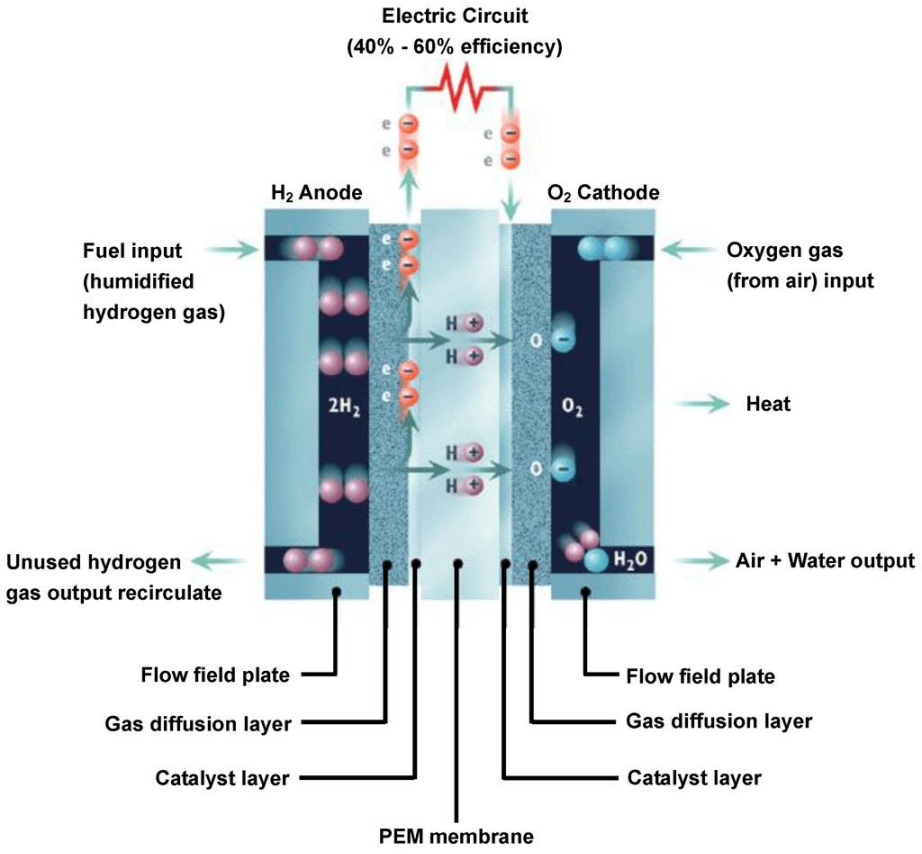

Figure 2.12: Diagram of a PEM fuel cell (fuelcellstore.com).

1.4.2.3 H_2/O_2 Alkaline Anion Exchange Membrane Fuel Cells (AEMFC)

Alkaline AEM fuel cells have recently received more attention because of the possibility of working with non-precious metal catalysts, which reduces the cost of this technology. They also operate at low temperature (< 100 °C) like PEMFCs. At the beginning, the main barrier to the development of these devices was the availability of membranes with high conductivity, so many efforts have been devoted to the development of new polymeric membranes capable of overcoming the problem of limited OH^- conductivity[23,24]. The hydroxyl anion is transported from the cathode to the anode, opposite to the H^+ conduction direction in a PEMFC, as shown in the figure below.

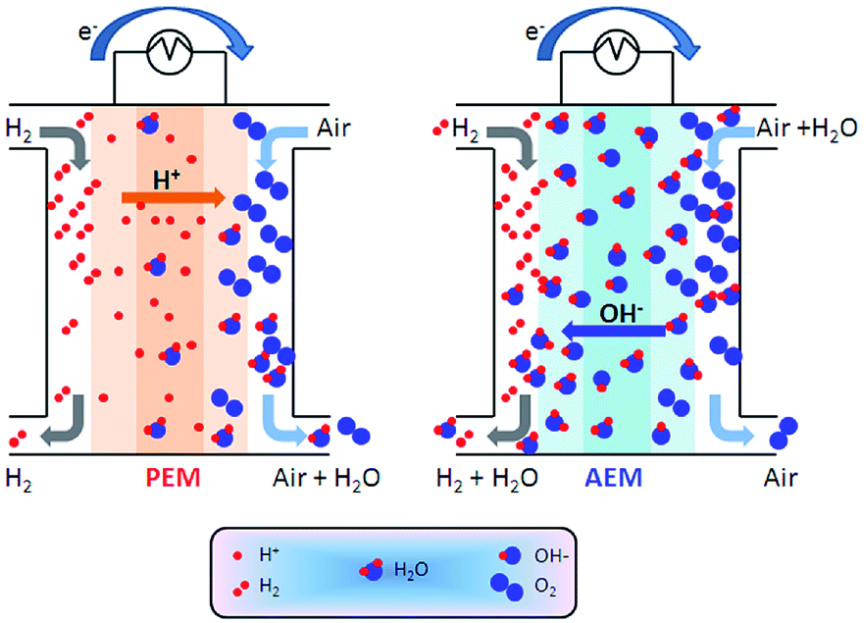

Figure 2.13: Scheme of an AEM fuel cell compared to a PEM fuel cell. [25]

The alkaline pH environment offers several advantages:

- Enhanced ORR kinetics, allowing the use of Pt-free catalysts.
- Wider choice of materials for the construction of the cell.
- Use of less expensive polymeric membranes compared to PEMFCs.

Regarding the performance, H_2/O_2 AEMFCs have recently reached a peak power density of more than 1 W cm^{-2} (at 0.5-0.7 V) and a current density of 2 A cm^{-2} using PtRu/C as highly active catalyst for the HOR. While the best performance with Pt-free catalysts are these reported using Pd-based catalysts, doped with NiO or CeO_2 for HOR, and Ag-based catalysts for ORR[25–27].

2.4.3 Anion exchange membranes for electrolysers and fuel cells

The role of an anion exchange membrane (AEM) is to transport hydroxyl ions (OH^-) from the cathode to the anode, and act as an insulator for electrons. An AEM is formed by a polymer backbone, generally polysulfone (PSF) or polystyrene cross linked with divinylbenezene (DVB), decorated with anion exchange functional groups, which are often quaternary ammonium salts. The polymer backbone has to guarantee the mechanical and thermal stability, while the functional groups the exchange capacity and ionic conductivity. The whole set determines the chemical stability.

A commercially available membrane commonly used is A-201 (Tokuyama Corporation, Japan). The structure is shown in Figure 2.14. The backbone of A-201 is a linear hydrocarbon chain and the functional groups are quaternary ammonium groups[17].

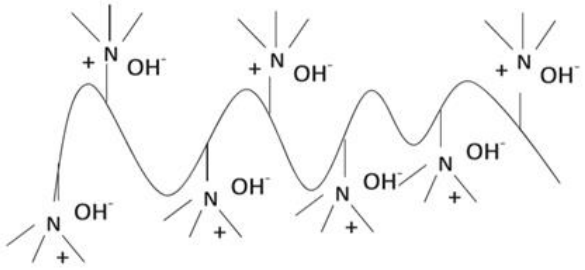

Figure 2.14: Structure of the quaternary ammonium A-201 membrane (Tokuyama Corporation, Japan) [17].

Several other polymer backbones and functional groups for AEMs have been developed and tested in AEM cells. The polymer backbones include PSF, chloromethylated low-density polyethylene (LDPE)[28] or high-density polyethylene (HDPE)[29], methylated melamine, and poly(vinylbenzylchloride). Alternative functional groups to trimethylamine are 1-azabicyclo-[2.2.2]-octane and 1-methylimidazole[17].

3 Electrocatalysts

3.1 Carbon supported catalysts

Electrocatalysts consist of an electrochemically active phase usually based on metal nanoparticles, and a conductive and chemically inert support material, which is generally based on carbon black.

The surface of metal nanoparticles is generally very active and can promote the kinetics of different electrochemical reactions. The choice of metal catalyst is a crucial point in electrocatalysis, concerning not only its specific activity toward the reaction of interest and selectivity for a certain product, but also practical considerations for eventual applications in real devices such as material stability, cost and sustainability. Nanotechnology plays an important role in the synthesis of catalysts with high Electrochemical Active Surface Area (EASA) and high dispersion on the support, and in engineering the contact phase between different metals to promote synergistic effects.

The most commonly used carbon supports are Vulcan XC-72 and Ketjen Black EC 600 JD. They consist of several graphene-like layers aggregated in particles of different

diameters, ranging from 5 to 100 nm. These aggregates are usually assembled into 3D superstructures, which span from 1 to 100 μm, depending on the degree of branching, with a total surface area of 254 $m^2 g^{-1}$ for Vulcan XC-72 and 1300 $m^2 g^{-1}$ for Ketjen Black EC 600 JD54[30].

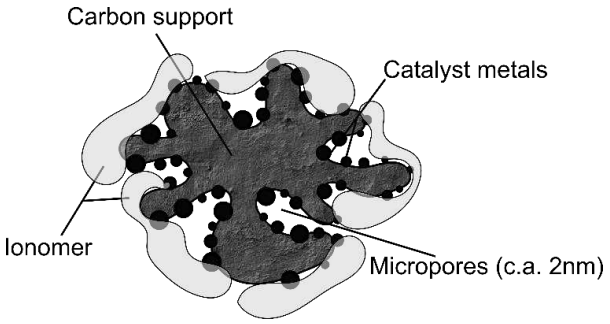

Figure 3.1: Schematic representation of an electrocatalyst (catalyst metal—carbon support – ionomer) [10]

The use of the ionomer can be avoided when operating with fuel cells and electrolysers fed by liquid fuels containing an ionic conductor, e.g., KOH. In this case, another polymer, the binder, which holds all the components of the catalyst layer together ensuring mechanical stability, is used. Usually, PTFE is the most preferred binder material.

In fuel cells fed with H_2 and O_2, the anodic and cathodic electrocatalysts are deposited onto a special support, named Gas Diffusion Layer (GDL). This has the role of distributing the reactant gases homogeneously from the flow field to the catalyst layer, as well as preventing catalyst flooding by removing heat and excess water from the electrode. GDLs are carbon-based fiber materials such as Carbon Paper or Carbon Cloth. They are also electronic conductors; this is necessary to transport electrons to or from a metal collector located on the back of the gas diffusion layer in the cell.

In the next paragraphs, the synthesis and characterization of several carbon supported nanostructured metal catalysts is described, and also carbon-CeO_2 support is described: among them it is important to emphasize Pd-CeO_2/C catalyst (Paragraph 3.1.3.1), prepared in the ICCOM-CNR laboratories, which has maximized Pd-to-CeO_2 interfacial contact and improved activity for the HOR in AEMFCs[31].

3.1.1 Preparation of Fe/C and Ag-Co/C cathodes catalyst for fuel cells

-Fe/C: Ketjen Black EC-600JD (5 g) was added to a suspension of FePc (Aldrich 90%) (1.5 g) in ethanol (200 mL) that had been stirred for 30 min at room temperature and

sonicated for 30 min. The resulting mixture was stirred for 24 h at room temperature and then sonicated for a further 30 min. The solvent was removed under reduced pressure and the solid residue was dried to constant weight. The resulting solid was introduced into a quartz tube and heated at 600 °C under a flow of N_2 (0.1 L min^{-1}) for 2 h. After cooling to room temperature under nitrogen flow, the resulting black powder was milled in a steel ball mill (20 min, 5 s^{-1}) prior to use. The Fe loading in the solid product were analyzed using ICP-OES (Fe, 3.05 wt%) [32].

-**Ag-Co/C**: Ag/C (40 wt %) on XC-72 Vulcan carbon was prepared using a citrate protection method as follows. A solution of sodium citrate (> 99%) (1.777 g) dissolved in 185 mL of water was added under stirring to an aqueous solution of $AgNO_3$ (> 99%) (0.314 g) in 185 mL of water. Then a solution of $NaBH_4$ (>96%) (0.07 g) in 250 mL of water was added dropwise under vigorous stirring to obtain a yellowish-brown Ag colloid. Next, 300 mg of Vulcan XC-72 carbon black (Cabot Corp.) was added into the Ag colloid. The resulting mixture was stirred for 8 h, the black suspension was filtered, washed, and dried at room temperature to obtain the 40 wt Ag/C (Yield 411 mg). CoPc-modified Ag/C was prepared by adsorbing 6.32 mg of CoPc (97%) onto 200 mg 40 wt % Ag/C in 50 mL of dimethylformamide (DMF) (99.8%) by stirring at room temperature for 20 h. The solid product was collected by filtration, washed with ethanol and dried at 60 °C [33].

3.1.1.1 Characterization

The catalysts have been then investigated by x-ray diffraction (XRD). Figure 3.2 shows the spectra for Fe/C and Ag-Co/C, with the reference cathode Pt/C; while in Table 3-1 are summarized the main characteristic of these materials.

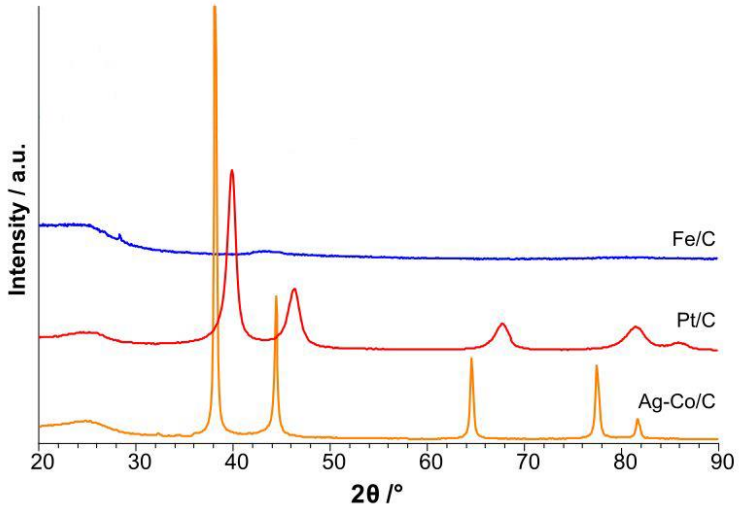

Figure 3.2: XRD pattern of cathodes with reference cathode Pt/C.

Table 3-1: physical characteristics of the catalysts.

Catalyst	Metal loading (%)	ECSA ($m^2\ g_{metal}^{-1}$)	Mean particle or crystallite size (nm)	Catalyst support
Ag-Co/C	40 (Ag)+3(CoPc)	n.d.	100 nm[a]	Vulcan XC-72
Pt/C HiSpec 4000	40	60[b]	4.5 nm[b]	Vulcan XC-72

a=estimated by XRD
b= values provided by manufacturer

3.1.2 Preparation of M(10%)/C (M= Pd, Rh, Ru, Ir)

-Pd/C: According to the Metal Vapor Synthesis procedure, Pd vapors were generated by resistive heating an alumina-coated tungsten crucible filled with Pd (150 mg, powder)[34]. The Pd vapors were condensed simultaneously at a liquid nitrogen temperature with acetone (100 mL) in the glass reactor chamber of the MVS apparatus for 1 h. The reactor chamber was then warmed to the melting point of the solid matrix (ca. -95 °C), and the resulting red–brown solution of Pd NPs, was siphoned at a low temperature into a Schlenk tube and stored at -40 °C. The metal content in the Pd solution was measured using ICP-OES was 1.2 mg mL^{-1} of Pd. A portion (95 mL) of the Pd solution was added to a suspension of porous carbon, Vulcan XC-72 (1.2 g) in acetone (50 mL). The mixture was stirred for 12 h at 25 °C. In this way, the Pd NPs were quantitatively deposited onto the Vulcan XC-72 carbon support. The colorless solvent was then removed by evaporation, and the resulting black solid product was

washed thoroughly with n-pentane (50 mL) and dried under reduced pressure. The Pd loading in the solid product was analyzed using ICP-OES (Pd, 10 wt%) [35].

Table 3-2: physical characteristics of the Pd/C catalyst.

Catalyst	Metal loading (%)	ECSA ($m^2\ g_{metal}^{-1}$)	Mean particle or crystallite size (nm)	Catalyst support
Pd/C	10	26[a]	2 nm[b]	Vulcan XC-72

a=determined by CO stripping voltammetry
b=Pd present as single atoms or very small clusters determined by FT-EXAFS

-Rh/C: Vulcan XC-72 (3.8 g) was suspended in 640 mL of ethylene glycol and sonicated for 80 min. Then the suspension was mechanically stirred (400 rpm) for 1 h under a N_2 atmosphere. A solution of 740 mg of $RhCl_3*6H_2O$ in water (160 mL) was added dropwise to the suspension under stirring. Subsequently an alkaline solution of 15.8 g of NaOH in water (80 mL) and ethylene glycol (200 mL) was introduced to the reactor and the resulting mixture was heated at 120 °C for 3 h. After cooling to room temperature, the resulting solid product was collected by filtration and washed with water to neutral pH and lastly dried in vacuum oven at 40 °C. Yield of Rh/C: 80%

-Ru/C and Ir/C: A suspension of metal salt (starting from 200 mL of aqueous solution of 312 mg of $RuCl_3*6H_2O$ or 183.4 mg of $IrCl_3*3H_2O$) and 900 mg Vulcan XC-72 was prepared in order to have 10 % of metal loading into the catalyst. After 1 h of stirring, 10 mL of aqueous solution of $NaBH_4$ (10:1 mol_{NaBH4}:mol_{Metal}) was added dropwise with the help of peristaltic pump at rate of 1 mL min^{-1}. After 30 min stirring, the solid were recovered by centrifugation, and dried in oven overnight.

3.1.3 Synergistic effect of CeO_2 modified Pd/C electrocatalyst

Ceria (CeO_2) has been the subject of many studies because of its oxygen storage capacity, rapid saturation with OH^- ions in alkaline media and spillover of OH^- to supported metal nanoparticles. It is also a mixed conductor, showing both electronic and ionic conduction, with many applications in catalysis in conjunction with transition metal[36–38].

One of the most interesting features of this material is the ability of Ce to switch between the Ce^{4+} and Ce^{3+} oxidation states, which allows the reversible addition and

removal of oxygen, the so-called oxygen storage capacity. It has been found that a mixed CeO_2/C support enhances the activity of Pd anodes by promoting the transfer of OH^- to form active $PdOH_{ads}$ species. It is for this reason that Pd-CeO_2 catalysts are largely used in a variety of dehydrogenation and oxidation reactions[37]. In particular, in this thesis, a new synthesis of a Pd-CeO_2/C catalyst with a maximized Pd-to-CeO_2 interfacial contact is reported, which presents an enhanced activity and stability for the hydrogen oxidation reaction (HOR) in AEMFCs[27,39].

3.1.3.1 Preparation of Pd-CeO_2/C

Firstly the CeO_2/C support (50/50 wt. %) was prepared adding 4 g of Vulcan XC-72 to a 250 mL aqueous solution of 5.31 g of $Ce(NO_3)_3$•$6H_2O$. The mixture was stirred for 30 min and then sonicated for further 30 min. After adjusting the pH to 12 with 2 M aqueous KOH, the resulting suspension was stirred vigorously for 2 h. The solid product was separated by filtration and washed with H_2O until neutral pH. The product was dried at 65 °C and subsequently heated under air in a tube furnace at 250 °C for 2 h. Cooling to room temperature was undertaken under a flow of Ar. Subsequently, 4 g of the CeO_2/C support as prepared was used for Pd-CeO_2/C synthesis. CeO_2/C was suspended in 500 mL of water, stirred vigorously for 30 min and sonicated for 30 min. To this mixture, a solution of K_2PdCl_4 (1.38 g, 4.23 mmol) in water (60 mL) was added dropwise (1 mL min^{-1}) under vigorous stirring, followed by an aqueous solution of 2.5 M KOH (8.4 mL). 50 mL of ethanol was then added to the resulting mixture, which was then heated at 80 °C for 60 min. The product was filtered off, washed several times with distilled water to neutrality and finally dried under vacuum at 40° C until constant weight. The synthesis yield was 93% [38].

3.1.3.2 Preparation of M-CeO_2/C (M= Ru, Rh, Ir)

200 mL of aqueous solution of metal salt (256 mg of $RhCl_3$*$6H_2O$, or 312 mg of $RuCl_3$*$6H_2O$ or 183.4 mg of $IrCl_3$*$3H_2O$) and 900 mg of CeO_2/C were mixed in order to have 10 % of metal loading into the catalyst. After 1 h of stirring, an aqueous solution of $NaBH_4$ (10:1 mol_{NaBH4}:mol_{Metal}) was added dropwise with the help of peristaltic pump at rate of 1 mL min^{-1}. After 30 min stirring, the solid were recovered by centrifugation, and dried in oven overnight.

3.1.4 Characterization of M/C and M-CeO_2/C

The M/C (Figure 3.3 a) and M-CeO_2/C (Figure 3.3 b) samples were studied by X-ray diffraction (XRD) analysis (M = Pd (black line), Ir (red line), Ru (blue line), Rh (green line)). The diffraction peaks at approximately 24.8° and 41.8°, present in all spectra, are attributed to the graphitic (002) and (100) planes of Vulcan XC-72 [40]. In Figure 3.3 b the peaks located at 28.4°, 32.9°, 47.2°, 56.4°, 59.1°, 69.4°, 76.8°, 78.9° correspond to (111), (200), (220), (311), (222), (400), (331) and (420) planes of cubic ceria structure [41]. The presence of Ru nanoparticles is confirmed by the carbon peak widening at 41.8° due to the nearness of the (100) and (002) metallic ruthenium planes diffraction peaks at 38.3° and 42.1° [42]. Diffraction peaks of the Pd (111) planes at 40° are very evident both in Pd/C and Pd-CeO_2/C catalysts, moreover in Pd/C it is possible to observe the (200) and (220) plane signals at 46.7° and 68.2°, covered by the more prominent ceria signals in the other catalyst. A small peak at 40°, corresponding to iridium (111), is visible in Ir-CeO_2/C spectra; while the same peak is not evident in Ir/C catalyst, probably due to the small size of iridium nanoparticles (as confirmed by TEM). For the same reason, it is not possible to recognize rhodium diffraction peaks in the same spectral region [43].

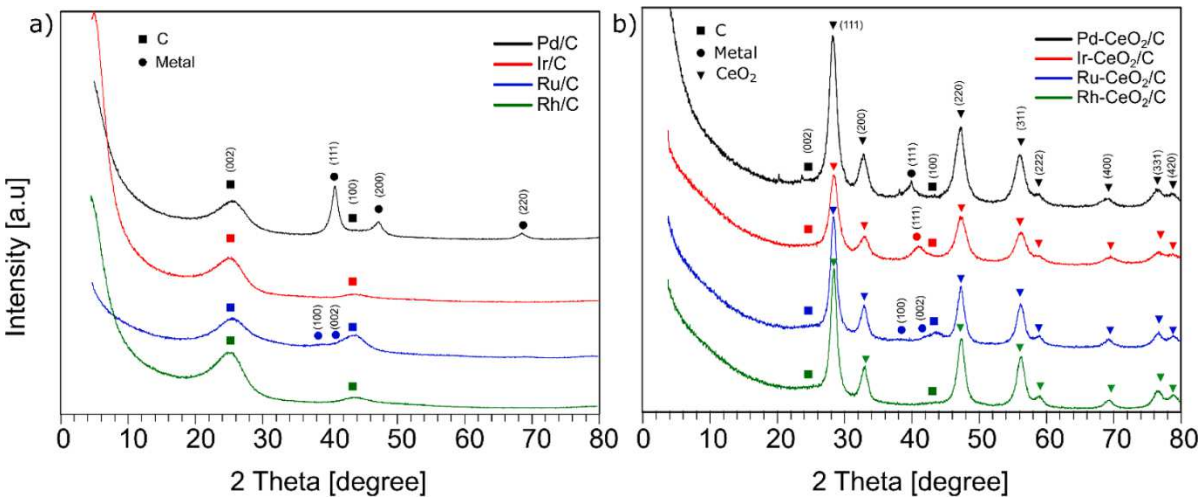

Figure 3.3: XRD of a) M/C and b) M-CeO_2/C catalysts (M = Pd, Ir, Ru, Rh).

The nanoparticle size distribution of the M/C catalysts was estimated using transmission electron microscopy (TEM) of selected portions of the samples where clustering of NPs was not present. For the M-CeO_2/C materials, an estimation was not possible due to the difficulty in distinguishing between the metal and CeO_2 phases. An

image of the Ru/C catalyst with relative size distribution is reported in Figure 3.4; for estimation of mean diameter, the Ru NPs, which have an irregular shape, were approximated to a sphere. TEM images of M-CeO_2/C and M/C catalysts are showed in Figure 3.5. The estimated mean diameter of the samples are as follows; Ru/C 3.5 ± 0.6 nm, Rh/C 2.9 ± 0.4 nm and Pd/C 4.2 ± 0.8 nm. For Ir/C, the extremely small size of the NPs (<2nm) does not allow for an accurate estimation.

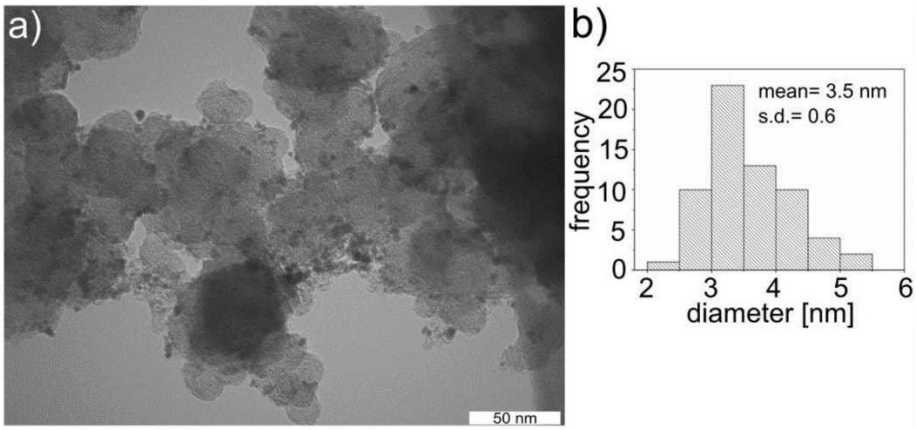

Figure 3.4: a) TEM image of Ru/C (scale bar of 50 nm) and b) corresponding particle size distribution histogram and mean diameter.

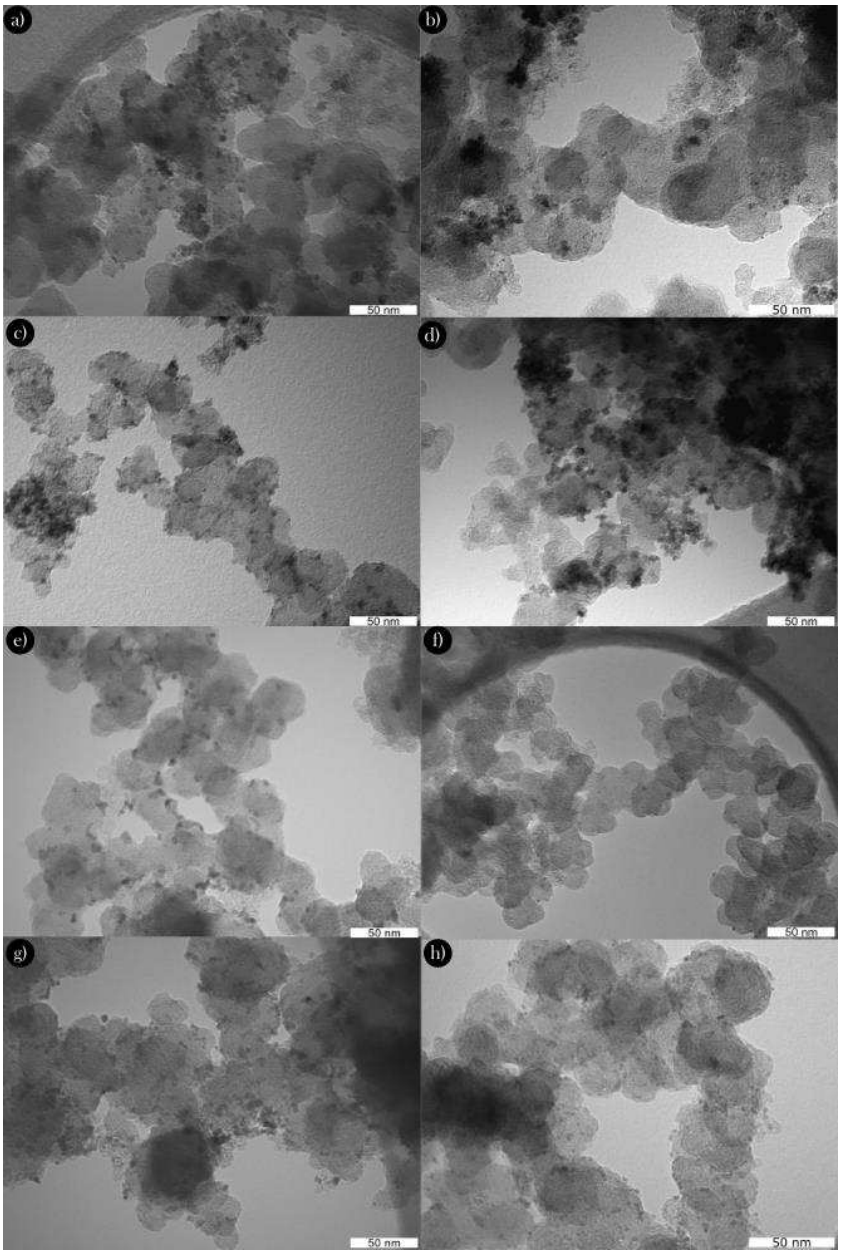

Figure 3.5: TEM images of a-d) M-CeO_2/C catalysts, with M equal to a)Pd, b)Ir, c)Ru, d)Rh; and e-h) M/C catalysts with M equal to e)Pd, f)Ir, g)Ru, h)Rh. Scale bar of 50 nm.

XPS analysis were used to investigate the surface chemical environment of the metals and it reveals a different behavior among them, due to the presence of CeO_2. In fact, as it is possible to see from Figure 3.6, the chemical state of each element appears differently influenced by the presence of ceria (more details in Table 3-3). Generally speaking, the addition of CeO_2 brings the metal system to a general lower oxidation state (i.e. Rh and Ir), to an unchanged scenario for Ru [44] and to a higher oxidation state for Pd.[41] The Pd3d XPS peaks were been fitted with two components at 335.9 eV and 338.3 eV, plus their relative spin–orbit splitting (Δ_{SO}) components (5.3 eV), assigned respectively to Pd(0) and Pd(II); the Ir4*f* has been fitted as well with two components,

one at 61.6 eV and the other at 63.0 eV assigned to Ir^{x+} (Ir_2O_x with $0 < x < 4$) and to Ir^{4+} respectively plus the relative Δ_{SO} components at +3.0 eV [45–47]. Ru3*p*, that is the only one that is not affected by the ceria introduction, can be deconvoluted into two components at 463.0 and 467.4 eV corresponding to Ru(4+) and Ru(6+) (Δ_{SO} 22 eV) [44]. The Rh3*d* spectrum has been deconvoluted with two components, 309.3 eV assigned to Rh^{x+} (with $+3 < x < +2$), whereas the B.E. value at 305.5 eV is assigned to Rh(0) (Δ_{SO} 4.8) [48]. Ceria is mostly composed of Ce(IV) (ca. 85 %) for all elements and the spectra are reported in Figure 3.7 [49].

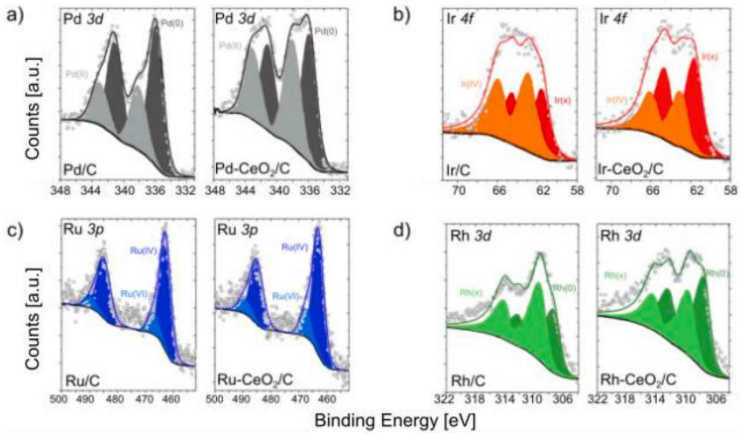

Figure 3.6: XPS peaks with relative curve fittings for: a) Pd3d, b) Ir4f, c) Ru3p and d) Rh3d. For clarity the oxidation number of the relative element has been reported close to the relative component and with the same color.

Table 3-3: XPS results data.

	Pd(0)/Pd(II) %	Ir(x)/Ir(IV) %	Ru(IV)/Ru(VI) %	Rh(0)/Rh(x) %
M/C	67	42	84	44
M-CeO_2/C	52	64	81	59

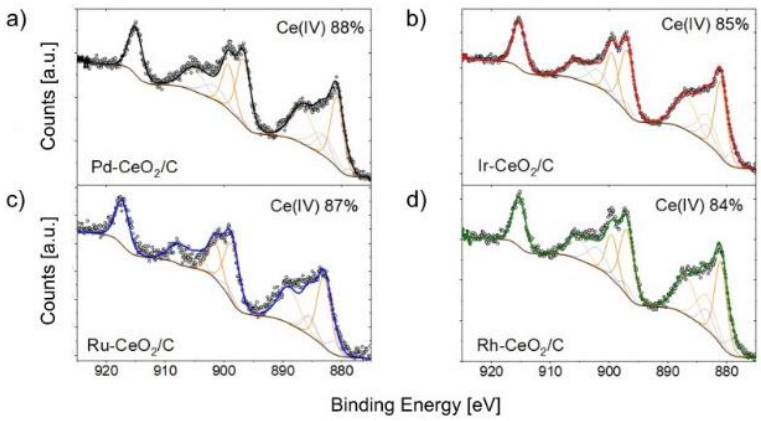

Figure 3.7: XPS spectra of the M-CeO_2 compounds in the region of Ce 3d with a Ce(IV) estimation for each sample.

From BET analysis, all the catalysts result mesoporous systems, where carbon particles have spherical shape with a narrow pore size distribution between 13.8 and 25.3 nm. BET surface areas (c.a. 150–200 $m^2\ g^{-1}$) are in line with carbon Vulcan values reported in literature [50]. All the catalyst containing ceria have a smaller BET surface area. Ceria, in fact, has a coverage effect which reduces the catalyst porosity. BET surface areas, BJH cumulative pores volume and pores width are summarized in Table 3-4.

Table 3-4: Catalysts BET surface area and BJH pores volume and pores width.

Sample	**BET Surface area ($m^2\ g^{-1}$)**	**BJH desorption cumulative pores volume ($cm^3\ g^{-1}$)**	**BJH Desorption average pore width (Å)**
Pd/C	161.3	0.70	208.7
Pd-CeO_2/C	142.5	0.44	159.9
Rh/C	186.0	0.81	227.3
Rh-CeO_2/C	157.7	0.45	138.5
Ru/C	205.3	0.95	252.8
Ru-CeO_2/C	154.2	0.54	182.8
Ir/C	191.4	0.93	253.0
Ir-CeO_2/C	153.5	0.57	182.0

3.2 IrO_2 anode synthesis for electrolyser

247 mg of $IrCl_3$*$3H_2O$ (0.7 mmol) were dissolved in 50 mL of ethylene glycol in presence of 700 mg of polyvinyl-pyrrolidone (PVP). The solution was heated at 120°C for one hour to evaporate residual water and then was refluxed for 60 minutes under magnetic stirring. The solution was concentrated, cooled down and poured in a

crucible, which was placed in a muffle furnace heated at 400°C for one hour (heating ramp: 7°C min^{-1}). The resulting solid was milled in an agate mortar.[51]

3.3 Ruthenium complexes supported onto carbon

So far it has been shown that a nano-scale approach has been adopted to reduce the amount of precious metal and in this regard, nanoengineered materials made it possible to economize in terms of expensive materials; but another promising strategy could be represented by so-called “single atom catalyst”. Unlike nanoparticles, which employ only the surface atoms as active sites, the single atom strategies potentially allow to use each atom as a catalytic centre, leading to an enormous saving of PGMs which result in a higher turnover numbers and molecular activity compared to heterogeneous electrode materials,[52] their properties also can be fine-tuned by well-established methods of organometallic synthesis.[53] Finally, molecular catalysts allow easier elucidation of their mechanisms which drives further improvement.

3.3.1 Synthesis of [RuH(μ-H)(Me_2(dad))($dbcot)_2$] (2).

Route 1: 200 mg of [RuH(μ-H)(Me_2(dad))($dbcot)_2$] (**1**) was mixed with tetrahydrofuran (10 mL), then ferrocenium triflate (106 mg in 6 mL THF) was added dropwise. The mixture was stirred at room temperature for 30 minutes before the solvent was evaporated at reduced pressure. The obtained brown solid was washed with diethylether: dimethoxyethane 9:1 (3x 3 mL). The leftover solid was dissolved in acetonitrile, filtered through a syringe filter and precipitated by layering with diisopropyl ether to obtain a red-brown powder.[54]

Route 2: 100 mg of [RuH(μ-H)(Me_2(dad))($dbcot)_2$] **1** was mixed with 1,2-difluorobenzene (20 mL). At -10 °C, a solution of triflic acid (1.43 mL of a 0.1 M solution in 1,2-difluorobenzene) was added dropwise over 30 minutes. The mixture was then stirred for 15 minutes and left to cool to room temperature. The obtained red-brown solid was washed with toluene (3x2 mL) and 1,2-difluorobenzene (1x2 mL). Subsequently, the solid was dissolved in acetonitrile and layered with diisopropyl ether. After 24 hours, the product was obtained as a red-brown powder. Yield: 167 mg, 69 %.

3.3.2 Synthesis of [Ru(OH_2)(μ-H)(Me_2(dad))($dbcot)_2$]$^{+3}$ (HSO_4^-)(SO_4^{2-}) (3a).

A 50% solution of sulfuric acid in water was degassed by bubbling argon through for 2 minutes. The acid solution (52 μl, 373 μmol) was dropwise added to a stirred dispersion

of [RuH(μ-H)(Me_2(dad))($dbcot)_2$] **1** (130 mg, 187 μmol) in THF (5 mL, 35 mM). The mixture was then heated up to 60 °C for 1 hour. The as obtained solid was washed with THF (3x1 mL) and hexanes (3x1 mL). After drying at HV overnight, a brightly red solid of the composition [Ru(OH_2)(μ-H)(Me_2(dad))($dbcot)_2$]HSO_4·0.34 THF·1.25 H_2SO_4 was obtained. Yield: 110 mg, 62 %.

3.3.3 Synthesis of [Ru(OH_2)(μ-H)(Me_2(dad))($dbcot)_2$]$^+BF_4^-$ (3a)

A 50% solution of HBF_4 in water was degassed by bubbling argon through for 2 minutes. The acid solution (36 μl, 287 μmol) was dropwise added to a stirred solution of [RuH(μ-H)(Me_2(dad))($dbcot)_2$] **1** (100 mg, 144 μmol) in 1,2-difluorobenzene (2.9 mL, 50 mM). The mixture was heated up to 65 °C for 10 minutes whereby a red solid started precipitating from the solution. The mixture was left at room temperature overnight which caused more solid to precipitate. The mother liquors removed by aspiration and the obtained solid was dried at HV overnight at 80 °C. The obtained crude product (119 mg, 104 %) was washed with 1,2-difluorobenzene (2x2 mL) and diethyl ether (2x2 mL), before being dried at HV overnight. A brightly red solid of the composition [Ru(OH_2)(μ-H)(Me_2(dad))($dbcot)_2$]BF_4 was obtained. Yield: 73 mg, 64 %.

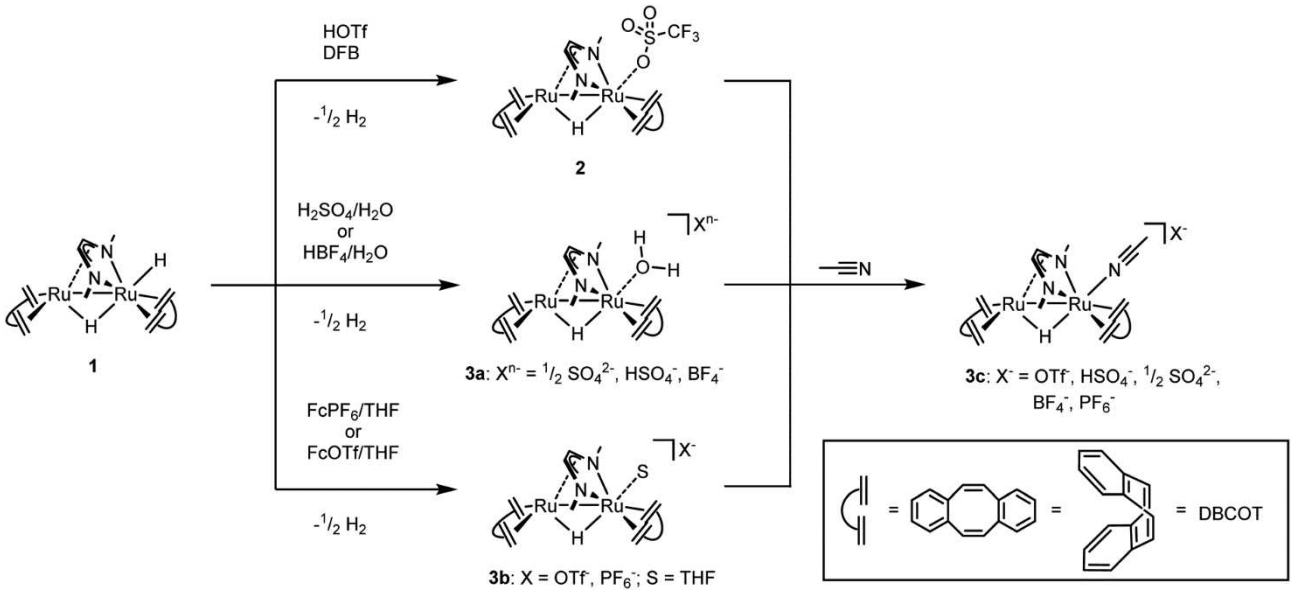

Figure 3.8: Syntheses of complexes **2**, **3a**, **3b**, and **3c** starting from **1**. OTf-= $SO_3CF_3^-$, Fc^+ = ferrocenium$^+$, DFB = 1,2-difluorobenzene.

3.3.4 Impregnation of Ru complex onto carbon

In a 100 mL Schlenk round bottom flask purged with N_2 and vacuum, 36.0 mg of [Ru_2(OTf)(μ-H)(Me_2dad)(dbcot)$_2$] were dissolved at room temperature in 15 mL of distilled acetonitrile. 214 mg of carbon black Ketjen Black EC-600-JD (C^k) (Akzo-Nobel) were milled in an agate mortar and suspended at room temperature in 60 mL of acetonitrile in a 100 mL round bottom Schlenk tube by 30 minutes of magnetic stirring. The two solutions were mixed together under nitrogen flow and the resulting suspension was homogenized at room temperature by 1 hour of magnetic stirring. The solvent was slowly evaporated under vacuum at 50 °C keeping on the magnetic stirring, in order to obtain homogeneous complex dispersion on carbon. The so obtained catalytic powder was then vacuum dried at 50 °C for 1 hour. The final catalyst has a 12.4 wt% complex content (3.06 wt% Ru). A diluted catalyst was synthetized with the same impregnation procedure just adapting the reactants amounts, as described in Table 3-5. The dry catalyst has a 1.86 wt% complex content (0.44 wt% Ru content) with a dilution of seven time respect the concentrated one [55–57].

Table 3-5: Complex impregnation on C^k, 0.04 mg_{Ru} cm^{-2} catalyst loading (0.44% wt.Ru).

Reactants	Quantity
[Ru_2(μ-H)(Me_2dad)(dbcot)$_2$OTf] /C^k	3.6 mg (0.005 mmol complex)
C^K	210 mg
CH_3CN for complex dissolution	5 ml
CH_3CN for C^k suspension	20 mL

3.3.5 Characterization

Electron microscopic images of freshly prepared **2_{dil}@C^k** are shown in Figure 3.9a-c and indicate the homogeneous distribution of the ruthenium complex on the carbon surface. Figure 3.9a shows the evidence of sub-nanometer high Z clusters (bright patches). This evidence is consistent with the presence of the Ru dinuclear units of the complex at the carbon surface. Moreover, HRTEM images show the structure of the carbonaceous support but no evidence of nanoparticles (Figure 3.9b-c), indicating that

the complex is homogeneously distributed over the carbon surface rather than forming aggregates.

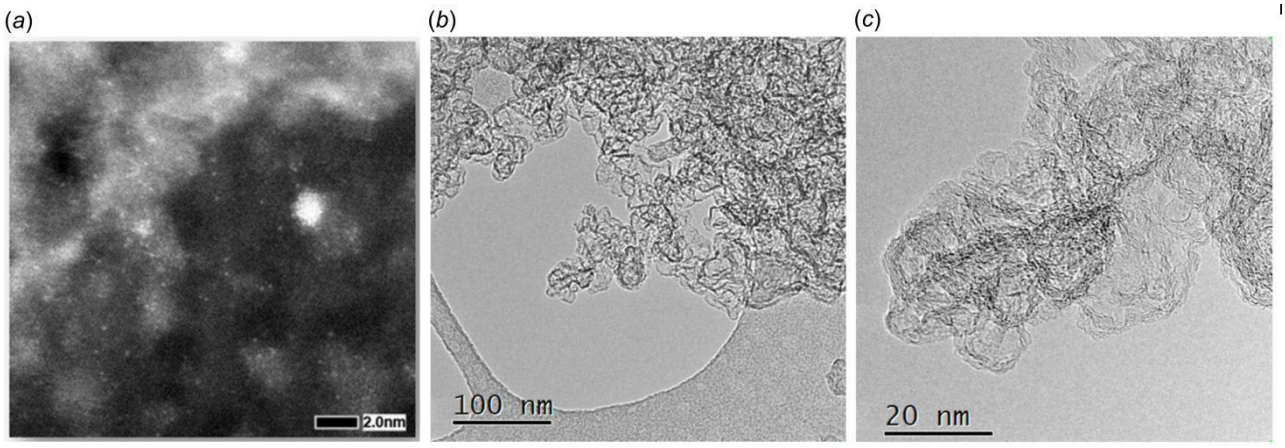

Figure 3.9 Electron microscopy images of pristine $\mathbf{2}_{dil}$**@C**^{k}. (a) High Magnification HAADF-STEM; (b) low magnification HRTEM; (c) high magnification HRTEM.

The crystal structures of $[Ru(OH_2)(\mu\text{-}H)(Me_2(dad))(dbcot)_2]BF_4$ and $[Ru(NCCH_3)(\mu\text{-}H)(Me_2(dad))(dbcot)_2]PF_6$ are reported in (Figure 6.1), while crystal data and further crystallographic details are reported in Table 3-6.

Table 3-6: Crystal data and structure refinement for $[Ru_2(OH_2)(\mu\text{-}H)(Me_2(dad))(dbcot)_2]BF_4$ and $[Ru_2(NCCH_3)(\mu\text{-}H)(Me_2(dad))(dbcot)_2]PF_6$.

	$[Ru_2(OH2)(\mu\text{-}H)(Me_2(dad))(dbcot)_2]BF_4$	$[Ru_2(NCCH_3)(\mu\text{-}H)(Me_2(dad))(dbcot)_2]PF_6$
Empirical formula	$C_{36}H_{35}BF_4N_2ORu_2$	$C_{44}H_{45}F_6N_6PRu_2$
Formula weight	800.10	1004.97
Temperature/K	100.01(11)	100.00(10)
Crystal system	triclinic	monoclinic
Space group	*P*-1	$P2_1/n$
a/Å	9.54690(10)	12.6141(2)
b/Å	10.1082(2)	12.2041(2)
c/Å	17.4002(3)	27.4630(5)
α/°	78.9600(10)	90
β/°	76.8190(10)	98.846(2)
γ/°	85.7730(10)	90
Volume/Å^3	1603.87(5)	4177.47(12)
Z	2	4
ρ_{calc}g/cm^3	1.657	1.598
μ/mm^{-1}	8.098	0.828
F(000)	803.0	2032.0
Crystal size/mm^3	0.042 × 0.036 × 0.02	0.49 × 0.16 × 0.11
Radiation	CuKα (λ = 1.54184)	MoKα (λ = 0.71073)
2Θ range for data collection/°	5.302 to 159.796	3.38 to 58.552
Index ranges	-12 ≤ h ≤ 12, -12 ≤ k ≤ 12, -22 ≤ l ≤ 22	-17 ≤ h ≤ 17, -16 ≤ k ≤ 16, -37 ≤ l ≤ 37
Reflections collected	40297	105366
Independent reflections	6799 [R_{int} = 0.0421, R_{sigma} = 0.0262]	10726 [R_{int} = 0.0602, R_{sigma} = 0.0383]
Data/restraints/parameters	6799/1/432	10726/0/542
Goodness-of-fit on F^2	1.076	1.233
Final R indexes [I>=2σ (I)]	R_1 = 0.0434, wR_2 = 0.0954	R_1 = 0.0462, wR_2 = 0.0982
Final R indexes [all data]	R_1 = 0.0465, wR_2 = 0.0971	R_1 = 0.0621, wR_2 = 0.1033
Largest diff. peak/hole / e Å^{-3}	2.47/-1.67	1.03/-1.00

3.4 Nickel foam supported catalysts

While metal nanoparticles and organometallic compounds have to be synthesised separately and then adsorbed onto the surface of a carbon support, Ni_{foam}-based catalysts can grow directly on it. These types of synthesis are well known in the literature; the high catalytic activity together with elevated surface area make these materials very suitable for electrocatalytic applications.

-MoO_2/Ni cathodes electrodes for water splitting, require two major steps of synthesis: firstly, Ni foam (Alantum Europe GmbH, pore size 450 μm, area density 420 g m^2, thickness 1.6 mm) was cut to 5 cm^2, cleaned using a sonic bath for 10 mins in HCl 6 M solution, then the same treatment was repeated with di water and finally acetone. The clean nickel foam was placed inside a Teflon lined autoclave immersed in 30 ml of an aqueous solution of the metal salts (1.2 mmol of $Ni(NO_3)_2.6H_2O$ and 0.3 mmol of $(NH_4)_6Mo_7O_{24}.4H_2O$); the autoclave was then sealed and heated at 150 °C for 6 h. The modified nickel foam thus obtained as a mixed oxide ($MoNiO_4$/Ni) was washed in di water and dried at 60 °C for 2 hours. In the second step, the modified nickel foam was annealed in a quartz tube oven at for 2 hours, under a flow of the gas mixture H_2:N_2 (5:95, v:v). Samples were prepared by varying the annealing temperature. Five samples were prepared at 400, 500, 600, 700 and 800 °C. Each sample is denoted using the preparation temperature.

-Fe-Mo-Ni/Ni: anode electrodes for oxygen evolution were prepared as follows. The sample prepared at 500 °C in the previous synthesis was immersed in 25 ml of a solution of $FeCl_3$ (1 mmol) for 15 minutes, under vigorous stirring. The modified nickel foam was removed from the solution and washed with di water and dried at 60 °C. The final step consists in an electrochemical activation carried out directly in the electrolyser cell, which consists of a scan voltage from 0 to 2 V at 10 mV cm^{-2}, this leads to the formation of the OER catalyst denoted as Fe-Mo-Ni/Ni.

-Scale-up synthesis of MoO_2/Ni (600 °C)

A 10 cm diameter nickel foam disk (area 78.5 cm^2), cleaned as described previously, was placed inside an autoclave in 90 ml of an aqueous solution of $(NH_4)_6Mo_7O_{24}*4H_2O$); and $Ni(NO_3)_2*6H_2O$ (2.34 and 3.02 g respectively), sealed and heated at 150 °C for 6 h. After the synthesis, the as obtained $MoNiO_4$/Ni was taken out from the autoclave and then washed with di water and dried in air at 60 °C; lastly placed

in a quartz tube furnace at 550 °C under H_2:N_2 (5:95, v:v) flow for 2 h. The material is referred to as MoO_2-Ni/Ni (78.5 cm^2).

3.4.1 Characterization

Hydrothermal treatment of surface cleaned nickel foam in a solution of 1.64 mmol of $Ni(NO_3)_2.6H_2O$ and 0.3 mmol of $(NH_4)_6Mo_7O_{24}.4H_2O$) at 150 °C for 6 hours results in the growth of cluster like structures that form a thick coverage of the nickel foam surface. These structures are composed of multiple rods with smooth surfaces as shown by SEM analysis (Figure 3.10a). This precursor material ($MoNiO_4$/Ni) was further heat treated under flowing 5 % H_2 in N_2 mixture at temperatures ranging from 400 °C to 800 °C (respective SEM images are shown in Figure 3.10 b-f). A clear increase in surface roughness with increasing annealing temperature is observed. In the 500 and 600 °C samples, the rod-like morphology is maintained with the growth of nanostructures on the smooth surface. Above 700 °C, a collapse in the rod structure is observed. The sample prepared at 800 °C shows a collapsed agglomerated structure.

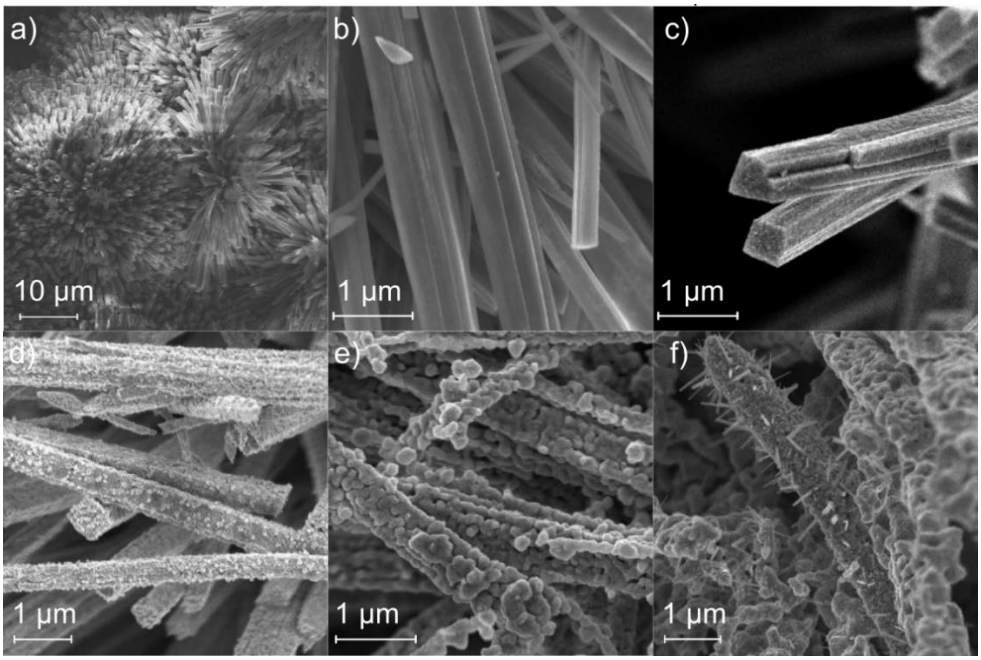

Figure 3.10: SEM images of a) $MoNiO_4$ on nickel foam and (b-f) after reductive heat treatment at 400, 500, 600, 700 and 800 °C, respectively.

XRD traces (Figure 3.11 a) show the trend of the signals of each material as a function of annealing temperature, starting from the precursor up to the sample prepared at 800 °C. It is clear that the patterns are dominated by the contribution of the nickel foam

support. In order to examine the surface grown crystalline phases of the 400 and 600 °C samples, sonication of each sample in ethanol was used to detach the surface structures that were subsequently collected by filtration and examined as powders (Figure 3.11 b). Compared to the sample prepared at 400 °C, the sample prepared at 600 °C shows an increase in the intensity of the peaks at 21.1°, 37.1° and 53.2° (MoO_2) as well as those for the $MoNi_4$ alloy at 43.96°, 51.6°, 64.68°, 75.72° corresponding to (121), (002), (231), (240) planes, along with the disappearance of the peaks at 14.36° and 28.86° assignable to the phase of the precursor $MoNiO_4$. Peaks marked with (*) refer to various stoichiometric compositions of MoNi alloys that are difficult to assign.

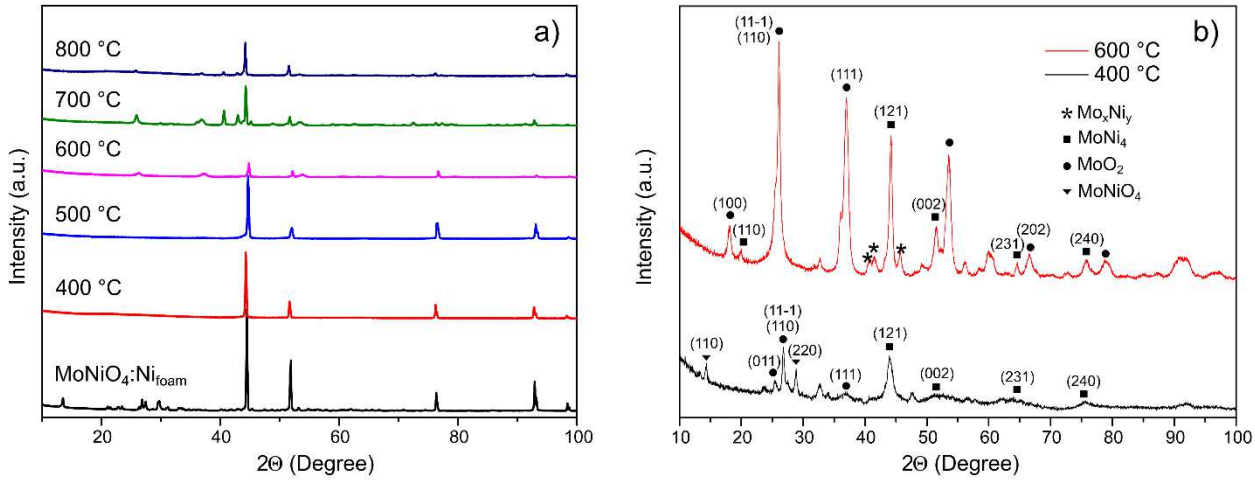

Figure 3.11: a) XRD patterns of cathode electrodes and b) XRD patterns of powdered materials MoO_2/Ni treated at 400 and 600 °C.

The chemical composition of the surface of each sample was investigated by XPS (Figure 3.12). Regarding the precursor, the surface is composed of a mixture of Ni and Mo species. The nature of the Ni component from the XPS is mostly ascribable to $Ni(OH)_2$ and NiO or a mixture of both. Regarding $Ni(OH)_2$ is not clear if it is only the hydroxide or the g-NiOOH.[58] The Mo composition is characteristic of $MoNiO_4$ with Mo(+6) as major species present as has been reported in similar procedures as $MoNiO_4$ nano-rods.[59] Subsequent annealing in H_2/N_2 atmosphere dehydrates and partially decomposes $NiMoO_4$ to form species like $MoNi_4$ and MoO_2, which form on the surface of the undecomposed $NiMoO_4$ host nanorods. The degree of formation of these species was studied as a function of annealing temperature, which was varied from 400 to 800 °C. The XPS results are more complex with the presence of four Mo

oxidation states (0, +4, +5, +6). The high-resolution Mo *3d* signal can be deconvoluted into four typical components at 227.9, 229.2, 230.4, and 232.2 eV corresponding to Mo(0), Mo(4+), Mo(5+), and Mo(6+), respectively. The relative concentrations are listed in Table 3-7.

Table 3-7: surface composition of MoO_2/Ni catalysts by XPS measurements.

$MoNiO_4$/Ni	Mo	Ni	O
Theoretical %	12.5	12.5%	75.0%
Theoretical Stoichiometry	1	1	6
Experimental %	10.6%	9.8%	79.6%
Experimental Stoichiometry	1.1	1.0	8.1

MoO_2/Ni (400)	Mo	Ni	O
Theoretical %	9.1%	18.2%	72.7%
Theoretical Stoichiometry	1	2	8
Experimental %	10.3%	16.2%	73.5%
Experimental Stoichiometry	1	1.6	7.1

MoO_2/Ni (500)	Mo	Ni	O
Theoretical %	8.3%	25.0%	66.7%
Theoretical Stoichiometry	1	3	8
Experimental %	8.2%	23.9%	67.9%
Experimental Stoichiometry	1.0	2.9	8.3

MoO_2/Ni (600)	Mo	Ni	O
Theoretical %	5.3	26.3%	68.4%
Theoretical Stoichiometry	1	5	12
Experimental %	5.3%	25.1%	69.6%
Experimental Stoichiometry	1	4.7	13

MoO_2/Ni (700)	Mo	Ni	O
Theoretical %	3.2%	32.3%	64.5%
Theoretical Stoichiometry	1	10	20
Experimental %	3.2%	32.6%	64.3%
Experimental Stoichiometry	1	10.3	20.4

MoO_2/Ni (800)	Mo	Ni	O
Theoretical %	12.5%	12.5%	75.0%
Theoretical Stoichiometry	1	1	6

Experimental %	12.4%	13.2%	74.4%
Experimental Stoichiometry	1.0	1.1	6.0

Except for Mo(6+) and Ni(2+), the low-valence states of Mo (Mo(5+) and Mo(4+)) imply the formation of MoO_2 with oxygen vacancies. No Ni(0) is observed in the XPS spectra. These spectroscopic results corroborated with the surface $NiMoO_4$ being partially reduced to MoO_2 via annealing in H_2/N_2 reduction atmosphere at high temperature. The XPS analysis shows that the Ni species present do not change significantly with increasing temperature as a mix of oxide/hydroxides (Figure 3.13).[60,61] With the increasing annealing temperature, the low valence species Mo(4+) and Mo(0) are predominant with respect to Mo(6+). At high annealing temperatures (700-800 °C) the Mo(0) signal is suppressed suggesting some decomposition of the structure.

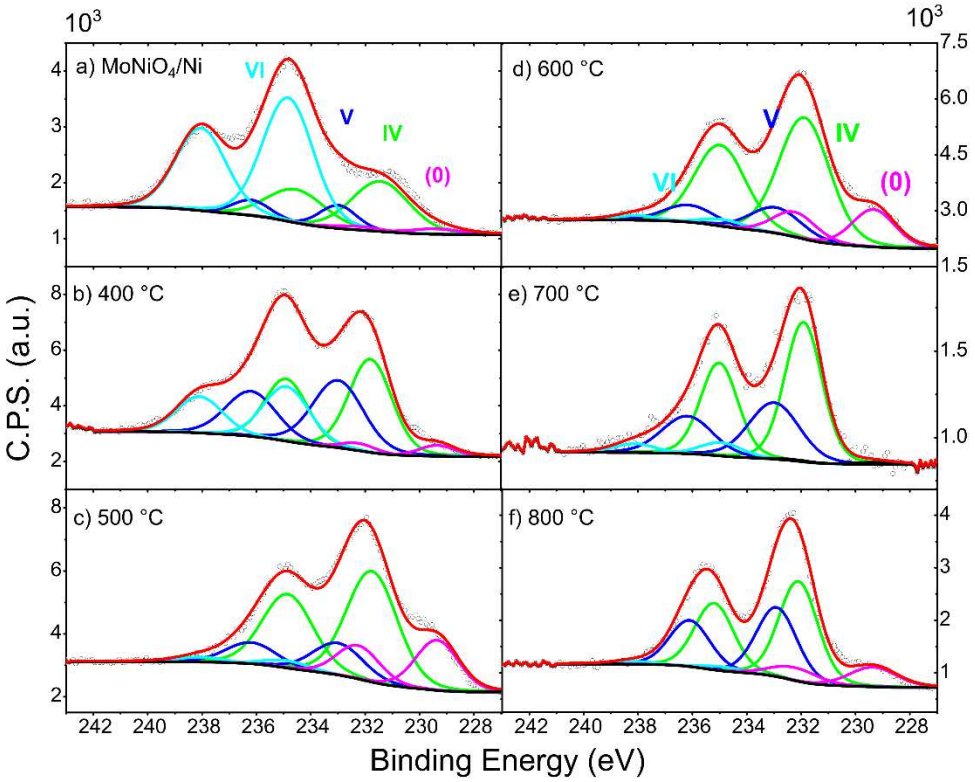

Figure 3.12: Mo XPS spectra of (a) $MoNiO_4$, and (b-f) MoO_2/Ni treated at various annealing temperatures.

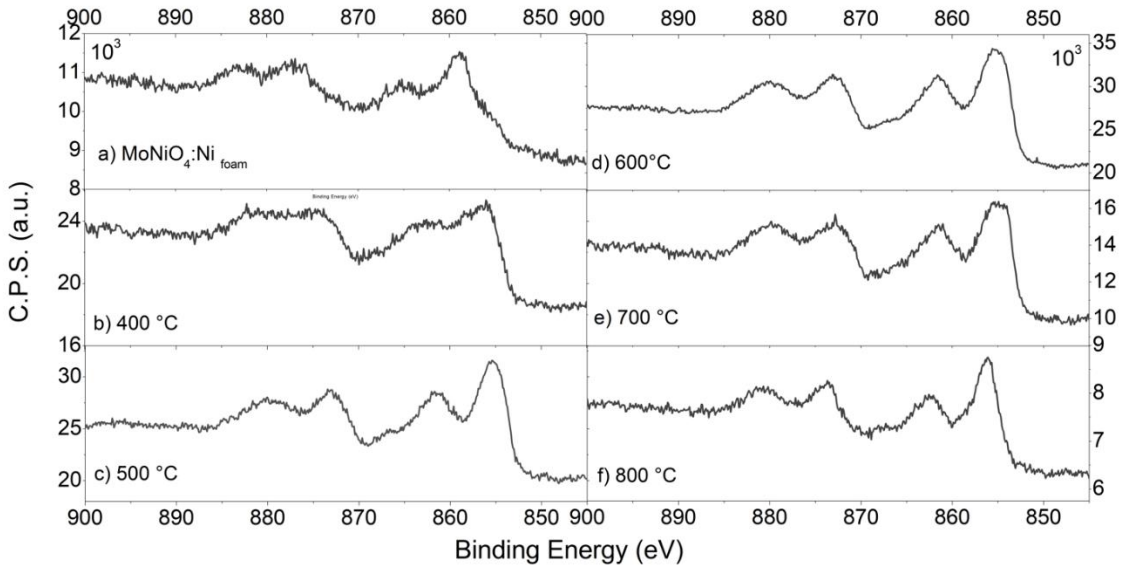

Figure 3.13: Ni 2p XPS of precursor a) and MoO_2/Ni samples prepared at various temperatures b-f).

Transmission electron microscopy (TEM) and scanning TEM (STEM) micrographs (Figure 3.14) of the sample treated at 400°C show a relatively low surface roughness of the rods with no apparent formation of nanoparticle structures. High-resolution TEM (HRTEM) analysis reveals an extended crystalline structure along all the rods. Selected area electron diffraction (SAED) analysis confirms lattice fringes that can be indexed as $NiMoO_4$, in agreement with the XRD results (Figure 3.15).

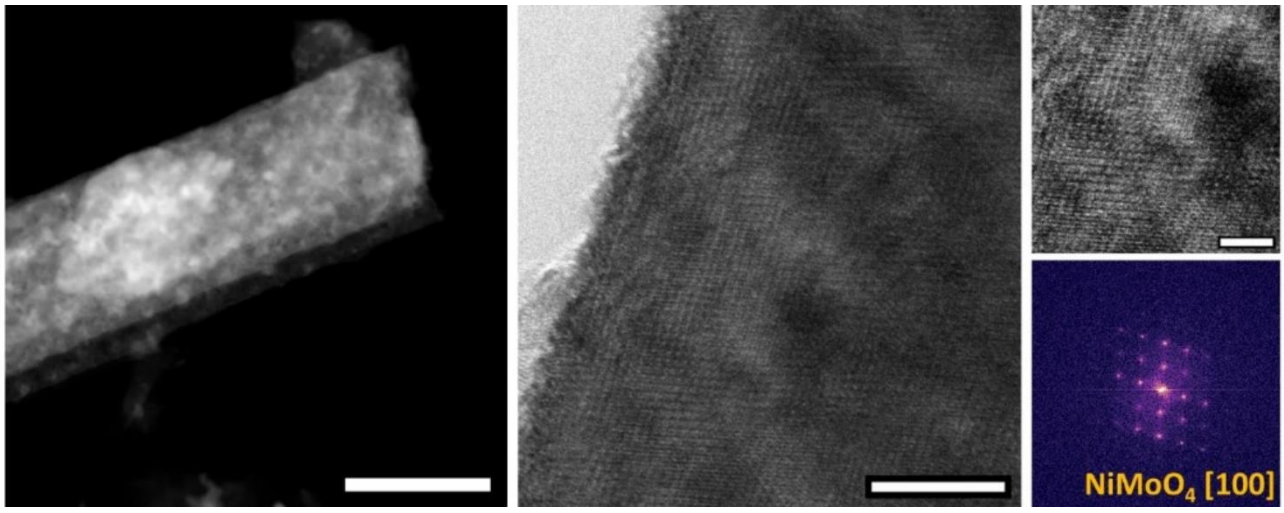

Figure 3.14: MoO_2/Ni (400 °C) sample: representative STEM micrograph (left side, scale bar 200 nm); HRTEM micrograph (center, scale bar 10 nm) and selected area HRTEM image (right side, scale bar 4 nm) whit related FFT (false color).

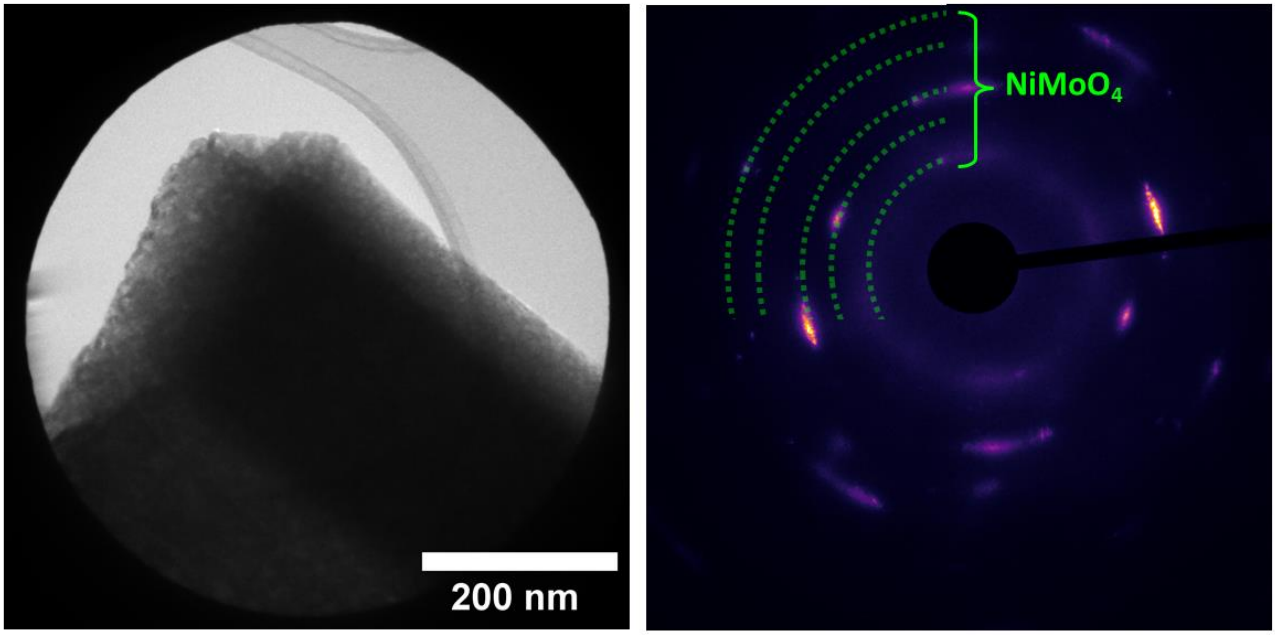

Figure 3.15: Selected Area (TEM micrograph) and related electron diffraction (false color) of sample prepared at 400 °C MoO_2/Ni. Main diffraction rings were indexed as $NiMoO_4$ (-1 1 1); (-1 2 0); (-1 2 2); (-1 2 3) and (0 -2 3) (from the center to the border).

After annealing at 600 °C STEM and TEM micrographs show a marked roughening of the rod surfaces which rather than being smooth appear more like agglomerated particles (Figure 3.16). HRTEM analysis carried out at the surface of this sample shows mainly nanostructured crystallites that by lattice fringes analysis can be ascribed to MoO_2. The results suggest migration of Mo species to the surface of the rods, leading to the formation of a polycrystalline surface including mostly MoO_2 and a smaller amount of Ni-enriched Mo mixed oxide nano-crystallites. STEM EDX mapping and analysis of a selected area transversal to the main rod-length, confirm the Mo-enrichment on the outer layer of about 200-250nm (Figure 3.17).

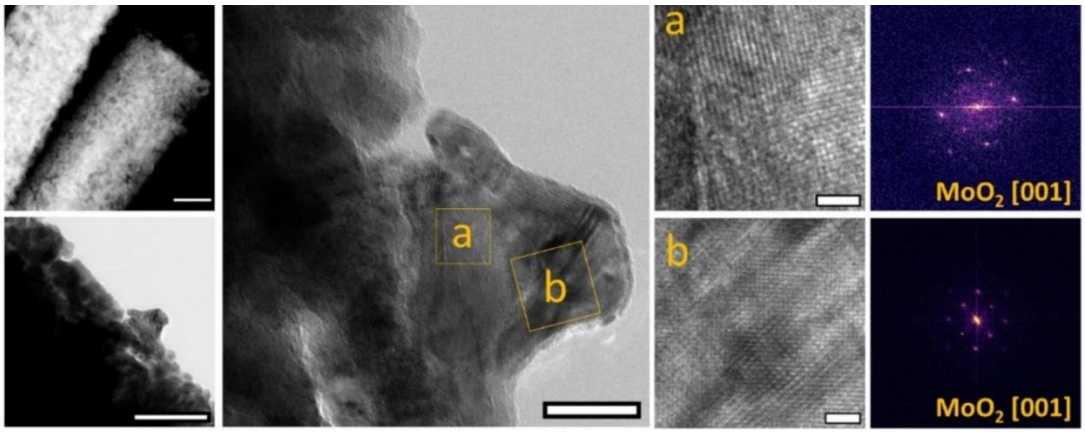

Figure 3.16: MoO_2/Ni - 600°C sample: representative STEM micrograph of (left side top, above scale bar 200 nm); TEM micrograph (left side bottom, above scale bar 100 nm); HRTEM micrograph (center,

scale bar 20 nm) and selected area HRTEM images (right side, both scale bar 2 nm) with related FFT (false color).

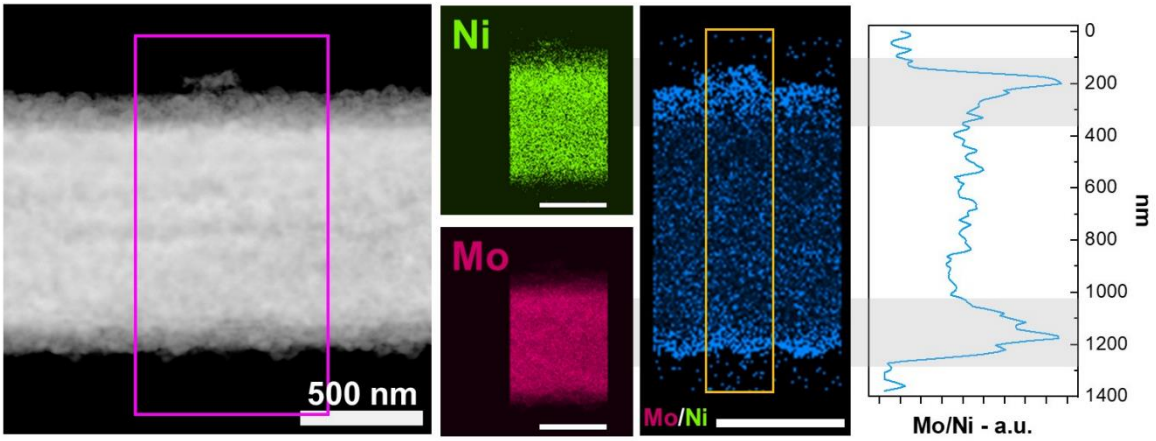

Figure 3.17: STEM micrograph and related EDX elemental mapping for Ni and Mo and calculated Mo/Ni ratio for MoO_2/Ni (600 °C).

STEM analysis of the sample prepared at 800°C reveals a drastic change in the morphology of the sample; the rod-like appearance is replaced by a smoothed and twisted collapsed structure (Figure 3.18).

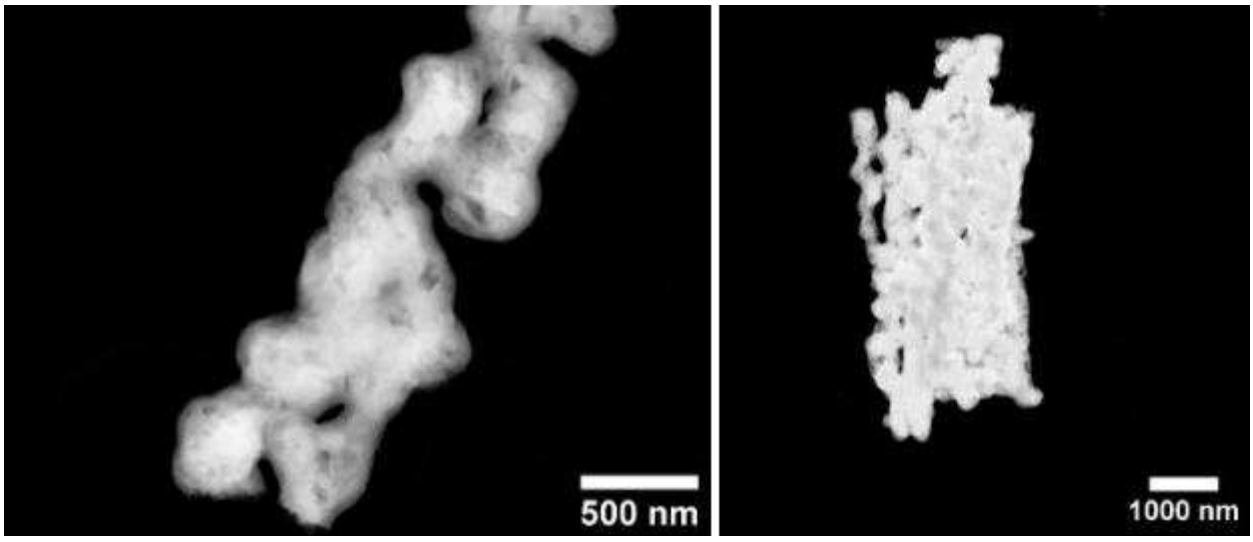

Figure 3.18: Representative STEM micrographs of sample MoO_2/Ni (800 °C).

4 Half reaction study: HER and HOR

4.1 Study of M-C and M-CeO_2 interaction for hydrogen evolution and oxidation in alkaline environment

4.1.1 Introduction

The intensifying energy supply crisis and continuing greenhouse gas emissions drives the search for carbon free and renewable energy sources. Due to the high specific energy density and clean combustion to water, molecular hydrogen (H_2) represents an interesting alternative to fossil fuels [62,63]. The hydrogen oxidation reaction (HOR) and its reverse, hydrogen evolution reaction (HER) are the key processes occurring in the fuel cell anode, and the electrolyser cathode, respectively [64,65]. The first device converts the chemical energy of H_2 into electrical energy, while the second acts as a storage device reconverting electrical energy into H_2. To maximize efficiency, the development of promising HOR/HER electrocatalysts that lower the overpotential of these reactions is of great importance. Research attention is focused on carbon supported metal nanoparticles (M/C) that, thanks to their high surface area and elevated metal dispersion on the support, including the possibility to exploit synergistic effects mixing the metal with other materials (for example certain metal oxides), could provide faster reaction kinetics. Pt-based compounds represent the state-of-the-art of HOR/HER catalysts [66,67]. Amongst noble metals, ruthenium (Ru), rhodium (Rh), palladium (Pd) and iridium (Ir) have attracted attention due to their favorable M-H bond strength that could make them promising candidates [68]. Ruthenium, with the cheapest price (25 % less than Pt) and a medium Ru-H bond strength of 65 Kcal mol^{-1}, has become the first choice to replace Pt. It is well known that platinum group metals show very fast HOR and HER kinetics in acidic environments, while the same reactions are more sluggish under alkaline conditions. However, it is of great interest to develop alkaline devices, because they offer a wider choice of materials for the construction of the cell (given the absence of corrosive electrolytes) and the use of less expensive polymeric membranes; moreover, in the specific case of fuel cells, ORR kinetics are faster [69,70]. In this context, tuning hydrogen binding energy (HBE) of noble metals, mixing them with metal oxides with favorable OH adsorption binding energy (OHBE) could be a promising strategy for the development of a new class of catalysts with enhanced HOR/HER activities in alkaline media. A valid example is the Pd-CeO_2/C

material [31,41,71,72], containing a mixed 50:50 carbon and ceria (CeO_2) support. It has been demonstrated that the addition of CeO_2 enhances the HOR activity of Pd, not only weakening the Pd-H_{ads}, but also promoting a rapid OH^- mobility and the formation of active Pd-OH_{ads} species. Qin et al. [73] reported another example of the strong metal-ceria interaction in the case of HOR electrocatalysts. They synthesized a novel Ir(10 %)/CeO_2-C material (20 % CeO_2 on carbon) and compared it with a simple Ir(10 %)/C; they observed that, unlike from Pd based catalyst, the Ir(10 %)/CeO_2-C hydrogen desorption peak potential does not shift negatively with respect Ir/C, indicating that ceria does not weaken the Ir-H_{ads} bond, but the promoted electrocatalytic activity is principally due to the oxophilic effect of ceria, which confers a higher oxygen storage-release capacity to the catalyst.

More recently, Ogada et al. described the preparation of a Pd-CeO_2/OLC HOR catalyst with an enhanced interfacial interaction and synergy among Pd, CeO_2 and the onion like carbon (OLC), that are beneficial for improved electrocatalysis, both in terms of high-performance and of durability in AEMFC devices. [74] In the case of HER active materials, Wang et al. [75] developed a flower-like CeO_2-supported Ru nanoparticles electrocatalyst, denoted as Ru(3 %)/CeO_2. Their results suggest that the intimate contact between Ru and CeO_2 enables a fast electron transfer at the interfaces, and that the electronic interaction metal-ceria accelerates the H_2O absorption/dissociation kinetic.

Herein, is reported the preparation and the systematic study of a series of carbon supported noble metal nanoparticles (M/C) and the respective M-CeO_2/C electrocatalysts (M = Pd, Ir, Ru, Rh) (Table 4-1).

Table 4-1: Synthesis data of all catalysts.

Catalyst	Metallic precursor	Reducing agent	Yield %
Pd/C	K_2PdCl_4*$6H_2O$	EG	100
Pd-CeO_2/C		EtOH	100
Ir/C	$IrCl_3$*$3H_2O$	$NaBH_4$	97
Ir-CeO_2/C			85
Ru/C	$RuCl_3$*$6H_2O$	$NaBH_4$	99
Ru-CeO_2/C			99
Rh/C	$RhCl_3$*$6H_2O$	EG	70
Rh-CeO_2/C		$NaBH_4$	100

Their HOR/HER performances under alkaline conditions (KOH 0.1 M) have been investigated with the rotating disc electrode (RDE) method. In particular, Tafel analysis were performed in order to extrapolate the Tafel slopes (b) and exchange currents (i_0).

These electrochemical parameters are compared, before and after the addition of CeO_2. It is demonstrated that, Ru/C is the most performing both for the HOR and the HER. It presents the best mass and specific activity at 0.1 V for both the reactions, and it exhibits the highest average value of exchange current of 106 A g^{-1} and the lowest Tafel slope of 43.1 mV dec^{-1} for HOR.

The positive metal-ceria interaction is demonstrated by an improvement of HOR/HER performance of Pd/C, Rh/C and Ir/C, while the beneficial effect is less marked in the case of Ru/C. Surface analysis of the catalysts by XPS evidences a change in oxidation states of Pd, Rh and Ir through the interaction with CeO_2 and EIS and capacitance (C) measurements show enhancement in electrochemically active surface area and conductivity.

4.2 Experimental

4.2.1 Half-cell testing

The working electrode, a glassy carbon disk (0.1963 cm^2) embedded in a PTFE jacket (PINE™) was cleaned by stirring overnight in a 0.05 μm alumina aqueous suspension. After the treatment, the electrode was washed in sequence, in acetone, 2-propanol and Milli-Q water. All the solutions were prepared with Milli-Q water (18.5 MΩ*cm at 25°C) provided with a Millipore Milli-Q^3 apparatus (Nihon Millipore Ltd.). Chemicals were used as purchased from Sigma-Aldrich/Merk unless as differently mentioned. All electrochemical studies were carried out at room temperature (20-25°C) using a Parstat 2273 potentiostat–galvanostat (Princeton Applied Research) equipped with a Model 616 Rotating Disk Electrode (PAR/Ametek). Polarization and chronoamperometric experiments in aqueous environment were acquired in a standard pyrex® three-electrode cell experiments (Princeton Applied Research). The reference electrode was a commercial Ag/AgCl/KCl_{sat} (Princeton Applied Research) and the counter electrode was a gold gauze enclosed in a glass tube with porous bottom. The measured potentials vs. Ag/AgCl were converted to the reversible hydrogen electrode (RHE) scale according to the Nernst equation:

$$E_{RHE} = E_{Ag/AgCl} + 0.059 * pH + E^{\circ}_{Ag/AgCl}$$

Where E_{RHE} is the converted potential vs. RHE, $E^{\circ}_{Ag/AgCl}$ = 0.1976 at 25 °C, and $E_{Ag/AgCl}$ is the experimentally measured potential against Ag/AgCl reference, potential was also was iR corrected to eliminate ohmic loss across the electrolyte. Catalyst inks were

composed of 5.8 mg mL^{-1} catalyst powder in 50:50 (v/v) water/ethanol containing 1 wt % Nafion. The resulting suspension was sonicated (59 Hz, 100 W) for 30 min. Knowing the percentage of the composition, the metal loading was calculated by weighing the dry deposit on the glassy carbon RDE (area = 0.1963 cm^2). Prior to all electrochemical tests, a solution of KOH 0.1 M was prepared by purging for 30 min the solution with H_2 or N_2. All measures were acquired using the software "Powersuite". Hydrogen evolution reaction (HER) and hydrogen oxidation reaction (HOR) were investigated through linear scan voltage (LSV) in H_2 saturated KOH solution, respectively from 0 to -0.4 V and from 0 to 0.6 V vs RHE, at a scan rate of 1 mVs^{-1}, with a rotation speed of 1600 rpm. Tafel analysis of LSVs data was performed by plotting log (i_k) versus overpotential (η), then important electrochemical parameters such as the Tafel slope (mV dec^{-1}) and the exchange current (i_0) were extrapolated by fitting the linear portion of the curve. In order to evaluate the roughness factor (RF) of the catalysts, CVs were recorded under the potential window of 0.6 and 0.7 V at various scan rate of 10, 20, 40, 60, 80, 100 mV s^{-1}. The electrochemical double-layer capacity (C_{dl}), expressed in mF cm^{-2}, was obtained by linear fitting of capacitive current density plotted versus scan rate. Electrochemical impedance spectroscopy (EIS) was performed at open circuit potential (OCP) over a frequency (f) range of 100 kHz - 0.01 Hz. For M-CeO_2/C catalysts, a stability test of 2 h was performed through chronoamperometric measurements at ± 0.05 V in H_2 -saturated aqueous 0.1 M KOH at 1600 rpm.

4.3 Results and discussion

4.3.1 Electrochemical characterization

The alkaline HOR/HER performance of all catalysts (M/C and M-CeO_2/C, M = Pd, Ir, Ru, Rh) were investigated by LSVs in H_2-saturated 0.1 M KOH solution. Measurements were run with a rotating disk electrode (1600 rpm) at a potential scan rate of 1 mV s^{-1}. HOR LSVs are shown in Figure 4.1 a) and c), while HER LSVs in Figure 4.2 a) and c). All extrapolated electrochemical parameters are reported in Table 4-2. Complete CVs in N_2-saturated 0.1 M KOH are reported in Figure 4.3.

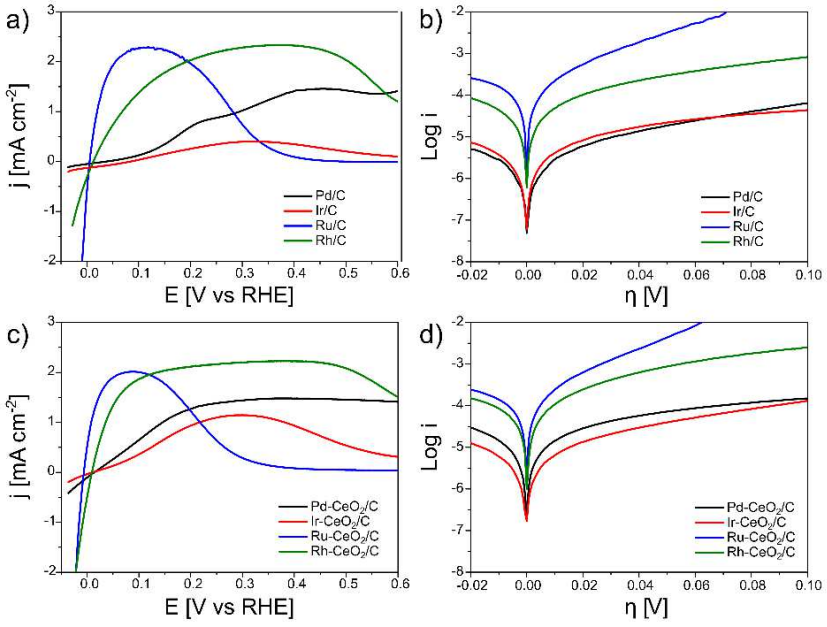

Figure 4.1: a) HOR LSV curves of M/C and c) M-CeO_2/C (M = Pd, Ir, Ru, Rh) in 0.1 M H_2-saturated aqueous KOH solution with a scan rate of 1 mV s^{-1} at a rotating speed of 1600 rpm. HOR Tafel plots of b) M/C and d) M-CeO_2/C (M = Pd, Ir, Ru, Rh).

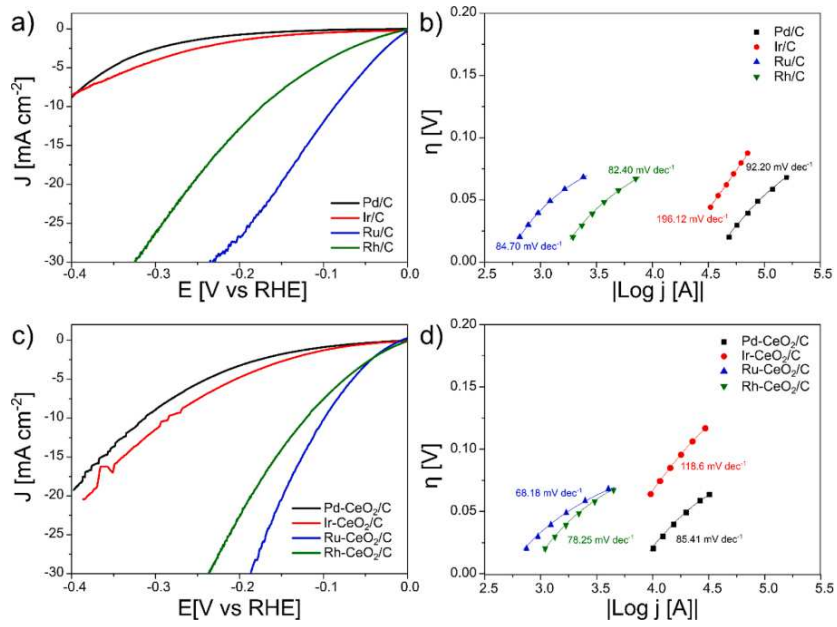

Figure 4.2: a) HER LSV curves of M/C and c) M-CeO_2/C (M = Pd, Ir, Ru, Rh) in 0.1 M H_2-saturated aqueous KOH solution with a scan rate of 1 mV s^{-1} at a rotating speed of 1600 rpm. Comparison of the HER Tafel slopes of b) M/C and d) M-CeO_2/C (M = Pd, Ir, Ru, Rh).

Table 4-2: Extrapolated electrochemical performance of catalysts under alkaline conditions.

Catalyst/C	Specific activity $\lvert[mA\ cm^{-2}]\rvert$ @η = 0.1 V *HOR HER*		Mass activity $\lvert[A\ g^{-1}_{Metal}]\rvert$ @η = 0.1 V *HOR HER*		Exchange current $[A\ g^{-1}_{Metal}]$ *HOR HER*		Tafel slope $[mV\ dec^{-1}]$ *HOR HER*		C_{dl} $[mF\ cm^{-2}]$
Pd/C	0.126	0.175	10.5	14.6	1.5	1.6	72.2	92.2	2.3
Ir/C	0.045	0.520	3.6	42.1	2.6	3.2	102.7	196.1	0.4
Ru/C	2.268	12.024	203.3	1084.0	98.2	114.5	43.1	84.7	19
Rh/C	1.372	4.266	112.2	349.0	27.7	32.9	78.8	82.4	4.0
Pd-CeO_2/C	0.648	0.890	73.5	75.9	11.4	7.4	74.9	85.4	1.7
Ir-CeO_2/C	0.361	1.296	36.6	130.7	4.3	6.8	79.0	118.6	3.9
Ru-CeO_2/C	2.005	10.154	205.1	1038.2	88.6	71.3	35.1	68.2	11.5
Rh-CeO_2/C	1.864	7.556	160.5	650.5	64.3	55.2	66.7	78.2	4.0

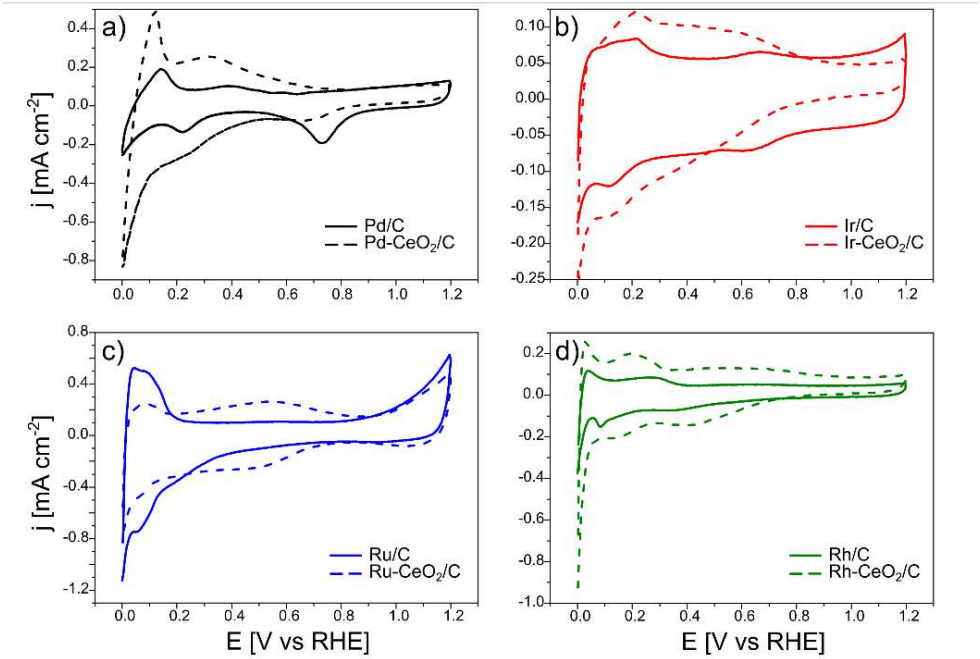

Figure 4.3: CVs of a) Pd/C and Pd-CeO_2, b) Ir/C and Ir-CeO_2, c) Ru/C and Ru-CeO_2, d) Rh/C and Rh-CeO_2 at scan rates of 20 V s^{-1} in N_2-saturated 0.1 M aqueous KOH solution.

Ru/C exhibits an outstanding HOR activity, both in terms of specific activity (mA cm^{-2}) and mass activity (mA g^{-1}_{Metal}). At an overpotential of 0.1 V, the HOR mass activity of M/C catalysts follows the trend Ru > Rh > Pd≫Ir, in particular Ru is respectively 1.8, 19.4, 30.5 times more active than Rh, Pd and Ir. The same metal trend order is valid for specific activity, where Ru/C reaches the value of 2.27 mA cm^{-2} at 0.1 V, demonstrating that the catalyst performance is not limited by the metal activity, but only by the hydrogen diffusion to electrode surface at the 1600 rpm fixed rotating speed. Rh/C has also a good HOR activity, but only at overpotentials above 0.3 V. While Pd/C, does not reach the hydrogen diffusion limiting current.

The presence of CeO_2 improves the HOR activity of all catalysts, in particular in the case of Pd-CeO_2/C and Ir-CeO_2/C. Our previous studies had demonstrated how ceria

is able to enhance Pd activity through a weakening of the Pd-H_{ad} bond strength and facilitating OH- spillover to metal nanoparticles [38,76]. Pd-CeO_2/C and Ir-CeO_2/C exhibit respectively an increase of over two and eight times in terms of specific activity. To further explore the HOR electrocatalytic performance of the catalysts the Tafel analysis was performed. Tafel plots obtained from HOR LSVs data are shown in Figure 4.1 b) and d). Between M/C catalysts, Ru/C displays the lowest Tafel slope value (43.1 mV dec^{-1}) and the highest exchange current density of 98.2 A g^{-1} (see in Table 4-2). In the case of M-CeO_2/C catalysts, Ru-CeO_2 does not show significant variation (b = 35 mV dec^{-1}, i_0 = 88.6 A g^{-1}), while Pd-CeO_2, Rh-CeO_2 and Ir- CeO_2 show a conspicuous increase in the exchange current suggesting an enhanced catalyst performance thanks to the metal-ceria synergy during the HOR [27,73].

The HER performance of all catalysts was also investigated. Ru/C displays the best catalytic efficiency reaching a specific activity of -12 mA cm^{-2} at the overpotential of 0.1 V (Table 4-2), immediately followed by Rh with -4.3 mA cm^{-2}; while Pd/C and Ir/C show current density lower than -10 mA cm^{-2} at an overpotential of 0.4 V. Also, in the case of HER, the addition of ceria has a beneficial effect, improving the specific activity of Pd, Rh, Ir; while Ru-CeO_2 is less affected by the presence the oxide species, presenting similar values of mass and specific activity with Ru/C. Tafel analysis was carried out for a more quantitative evaluation of the LSV data. The linear fitting of log J vs η curves are directly reported with respective Tafel slopes values in Figure 4.2 b) and d). Comparing Tafel slopes, values are lower for M-CeO_2/C catalysts, indicating faster HER kinetics of these materials at low overvoltages near the equilibrium zone.

The roughness factor (RF) of the all-synthesized catalysts was evaluated by capacitance measurements through CVs at different scan rates (from 0.01 to 0.1 V s^{-1}) in the double layer region (Figure 4.4) [77].

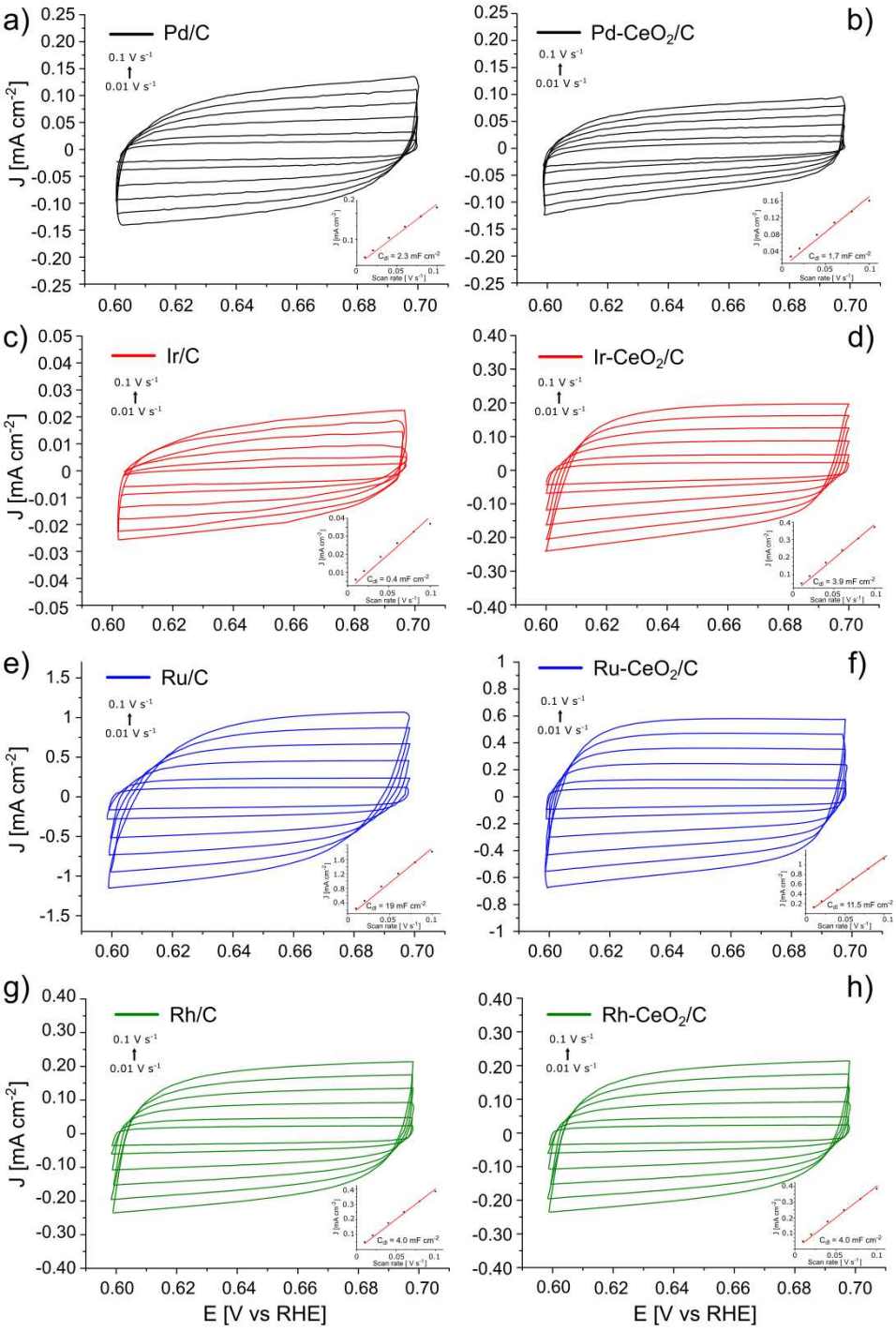

Figure 4.4: CVs of a) Pd/C, b) Pd-CeO_2, c) Ir/C, d) Ir-CeO_2, e) Ru/C, f) Ru-CeO_2, g) Rh/C, h) Rh-CeO_2 at scan rates of 10, 20, 40, 60, 80, 100 mV s^{-1} in 0.1 M KOH (insets: the corresponding capacitive current at 0.65 V *vs* scan rate).

As summarized in Table 4-2, the C_{dl} of Ru/C is 19 mF cm^{-2}, which is 4.8 times of Rh/C (4 mF cm^{-2}), 8.3 times of Pd/C (4 mF cm^{-2}), and 47.5 times of Ir/C. The respective M-CeO_2/C catalysts show higher RF values, all except Ru-CeO_2/C, where it is noticed a lowering of about 40 %. This trend is consistent with previous electrochemical

HOR/HER performances. Additionally, electrochemical impedance spectroscopy (EIS) was recorded. Nyquist plots are shown in Figure 4.5, the intercept at high frequency in the Z'(Ω) real axis represents the sum of the solution resistance Rs and the charge-transfer resistance Rct which assumes similar values for all catalysts (between 35 and 43 Ω); then a Warburg-trend response is observed (45° of slope), which could be related to ion/electron migration thorough the catalyst layer. At lower frequency, the impedance plot curves up to a limiting capacitance value, which corresponds to the total capacitance of the catalyst layer, which is proportional to active surface area.

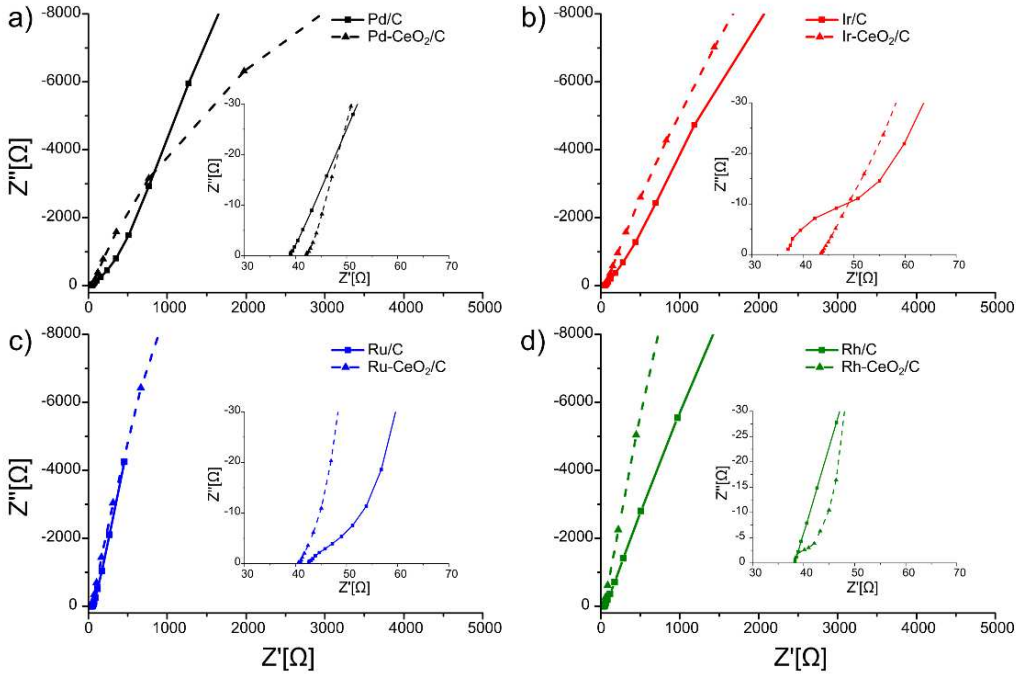

Figure 4.5: Nyquist plot of M/C and M-CeO_2/C catalysts in N_2 saturated 0.1 M KOH at OCV: a) Pd, b) Ir, c) Ru and d) Rh. Inset with zoom at low Z' [Ω] values.

Capacitance plots, shown in Figure 4.6, were obtained plotting capacitance values (C) versus the real part of impedance Z'(Ω). Capacitance was calculated using the following equation:

$$C = \frac{1}{2\pi f Z''}$$

The graphs show how the ionic resistance increases with the decreasing of the frequency (f), as more catalyst surface area becomes involved, while the steepness of the initial slope of the capacitance plot gives an idea of the conductivity within the catalyst layer.

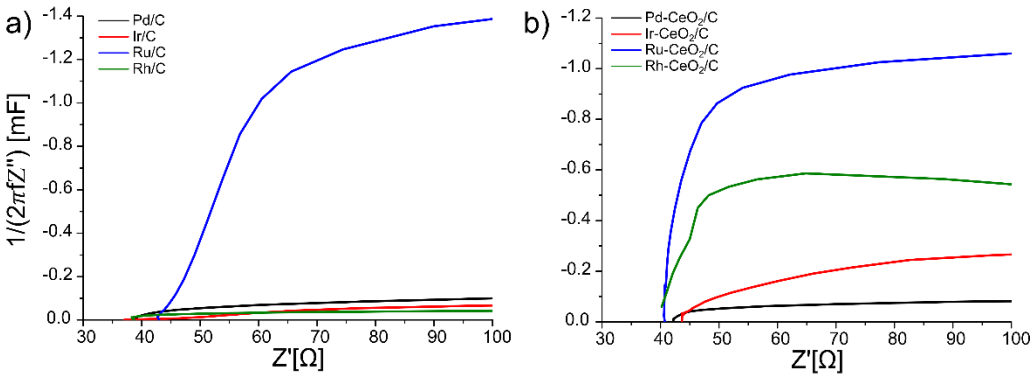

Figure 4.6: Capacitance plot of a) M/C and b) M-CeO_2/C electrocatalysts.

These results are quite in agreement with the previous observed HOR/HER trend of the materials; Ru/C and Ru-CeO_2/C catalysts, reaching capacitance plateau before the other catalysts, show the highest active surface area. This is consistent also with the RFs calculated through CVs (Figure 4.4).

Besides the addition of ceria does not change particularly the activity of Ru, but clearly improves the Pd, Ir and Rh based catalysts [78,79]. The stability of M-CeO_2/C catalysts during HOR and HER was verified performing chronoamperometric measurements for 2 h (Figure 4.7). The measures were recorded at ± 0.05 V at 1600 rpm in H_2-saturated aqueous 0.1 M KOH solution using the same theoretical metal loading of 5 ug on the working electrode for all samples. As expected, Ru-CeO_2/C outperforms all catalysts showing the highest and stable current density for both reactions (2.4 mA cm^{-2} for HOR and 4.9 mA cm^{-2} for HER on average). On the contrary Rh-CeO_2/C, although initially it shows the HOR/HER current density near to ± 1.9 mA cm^{-2}, its catalytic activity decreases rapidly reaching current density values similar to Pd-CeO_2/C and Ir-CeO_2/C. Pd-CeO_2/C shows a very stable performance during all over the time for both HOR and HER.

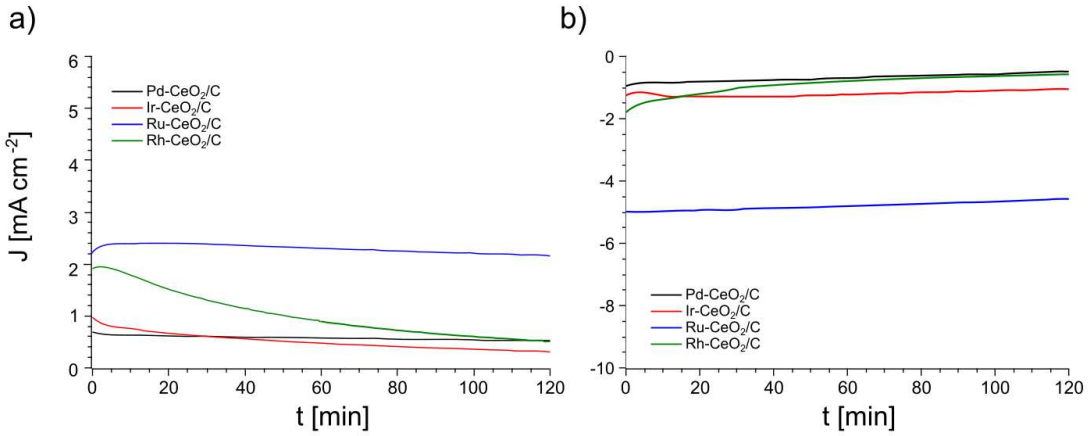

Figure 4.7: Chronoamperometric measurements (2 hours) of M-CeO_2/C catalysts at a) +0.050 V to test HOR stability and b) -0.050 V to test HER stability, at 1600 rpm in H_2-saturated 0.1 M KOH aqueous solution.

4.4 Conclusion

In this work, a series of M/C and M-CeO_2/C (M = Pd, Ir, Ru, Rh) electrocatalysts were prepared by chemical metal deposition and subsequent reduction on carbon or mixed ceria-carbon support (50:50 wt %). The successful synthesis of this series of materials was verified through physical characterization methods (XRD, TEM, XPS, BET). Subsequent they were electrochemically tested to study their HOR/HER performances in alkaline media. Among the M/C catalysts, the Ru based material has the best activity for both the reactions, exhibiting the highest exchange current and the lowest Tafel slope values. Its superior catalytic performance is attributed principally to an optimal Ru-H bond strength (65 Kcal mol^{-1}), the high roughness factor (19 mF cm^{-2}) together with the high electrochemically surface area, as evidenced by EIS analysis. The effect of the ceria addition on the electrocatalysts was investigated through XPS analysis, and electrochemically, comparing their catalytic performance with their respective metal on carbon materials. XPS evidences a change in the surface oxidation state of Pd, Ir, and Rh, proving a strong metal-ceria interaction (no modification in the case of ruthenium). This is reflected on the extraordinary improvement of HOR/HER performance of Pd/C, Rh/C and Ir/C, while the beneficial effect is less marked in the case of Ru/C. For example, the HOR mass activity of Pd, Rh and Ir is improved of 7.0, 10.2 and 1.4 times, while the HER mass activity of 5.2, 3.1 and 1.9 times respectively, while in the case of Ru is quite the same. Their better behavior is also evidenced by an improved electrochemically active area as pointed out by EIS results. This study

provides a promising strategy for designing highly efficient hydrogen oxidation and evolution catalysts for use in alkaline fuel cells and electrolysers, as shown also in the next paragraphs. This strategy can be used in the future with the aim of removing as much PGMs in the electrodes as possible to help the future commercialization of such devices.

5 Fuel cells

5.1 Employment of a low Pd content anode with several cathode catalysts.

5.1.1 Introduction

Anion exchange membrane fuel cells (AEMFCs) are becoming more attractive in recent years than the more established proton exchange membrane fuel cells (PEMFCs), this is essentially due to the employment of cheaper materials for the construction of the cells themselves, catalyst for ORR, and less expensive polymer electrolyte options, AEM and AEIs. The latter, have represented a big issue for many years due to their low ionic conductivity and stability in high alkaline environment, representing a limiting step that hampered the correct evaluation of the catalysts. The role of AEI, is fundamental as it serve to bind catalyst particle to the thin electrode layer, creating a porous anion conducting architecture to facilitate the transport of anions, electrons, reactants, and products, like H_2O[80].

The alkaline environment of AEMFCs potentially allows for the use of Pt-free catalysts for both the oxygen reduction reaction (ORR) and the hydrogen oxidation reaction (HOR), but unfortunately the HOR kinetics of Pt catalyst are very low, at least 2 orders of magnitude lower compared to acidic media[81].

The best performances in AEMFCs have been obtained with PtRu anode-based materials, for example Mandal et al., obtained 3.5 W cm^{-2} and current densities approaching a very impressive 10 A cm^{-2} when using crosslinked, low swelling, ca. 10 µm thick polynorbornene-type AEMs with a PtRu/AEM/Pt configuration.[82]

Ru is well known for having a favorable effect during HOR, weakening the hydrogen bonding energy (HBE) and make easier the bond cleavage[83,84]; also, a favorable OH_{ads} binding energy (OHBE) (e.g., metal oxides), is desirable to enhance the general

activity. To this regard, in this chapter will be discuss a new class of catalyst based on Pd nanoparticles and ceria oxide supported onto carbon (50% CeO_2, 50% carbon). The addition of ceria oxide helps Pd nanoparticle with the OH^- mobility on the surface of the catalyst and the formation of active Pd-OH_{ads}, with the simultaneous weakening of the H bonding (HBEs).[38]

This work has consisted in assembling an AEMFC containing Pd-CeO_2/C anode with a more crystalline high-density polyethylene-based RG-AEM (HDPE-AEM)[85]. Using this MEA has allowed to test several kinds of cathode: Pt/C benchmark, a Pt-free PGM type (Pd/C), a PGM-free precious-metal type (Ag-Co/C), and a CRM-free type (Fe/C).

5.2 Experimental

5.2.1 Half-cell testing

Measurements were performed as discussed in paragraph 4.2.1; in Table 5-1 are listed the metal loadings onto the working electrode:

Table 5-1: metal loading onto RDE working electrode for ORR measurement.

Catalyst	Catalyst loading µg	Metal loading µg
Pt/C	13.7	5.48
Pd/C	29.7	2.97
Ag-Co/C	31.3	12.5 (0.1)
Fe/C	27	0.81

All the measure shown here were reported with the reversible hydrogen electrode (RHE) potential scale. Electrochemical oxidation of adsorbed CO was used to measure the electrochemically active surface area (ECSA) of Pd catalysts were in 2 M KOH.[35]
In the first place, CO was purged into the KOH solution for 20 min to allow the complete absorption of CO onto the metal surface of the catalyst with the working electrode (WE) kept at 250 mV (RHE). Then, the excess CO in the electrolyte was purged out with N_2 for 20 min. Cyclic voltammetries were acquired from 0 to 1.5 V, the amount of CO_{ads} was then determined by integration of the CO_{ads} oxidative stripping peak (Figure 5.1). The corresponding ECSAs were calculated assuming a value of 420 µC cm^{-2} for a monolayer on Pd. [86,87]

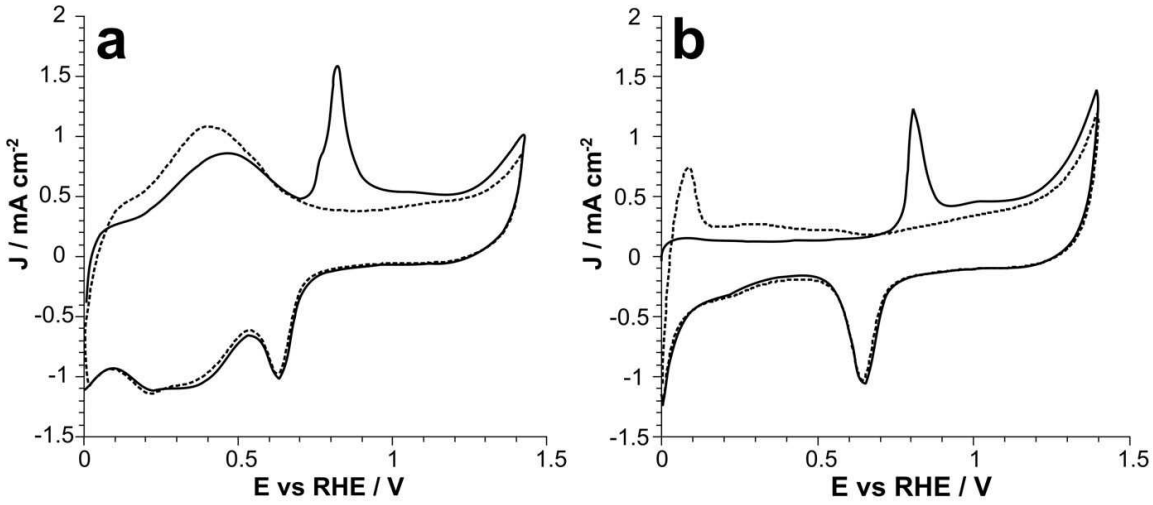

Figure 5.1: CO stripping voltammetry in KOH 2 M (a) Pd-CeO_2/C and (b) Pd/C. Pd loading; Pd-CeO_2/C (5.3 µg) and Pd/C (5.1 µg), monolayer CO coverage on Pd equivalent to 420 µC cm^{-2}.

HOR polarization (LSV) test for Pd-CeO_2/C, were performed in a 0.1 M KOH solution saturated with hydrogen (30 minutes of pure hydrogen bubbling) with 1 mV s^{-1} scan rate, rotating the WE at 1600 rpm. The hydrogen oxidation reaction was investigated in the range from 0 to 0.6 V vs RHE.

ORR polarization experiments for the Pt/C, Pd/C Ag-Co/C and Fe/C were carried out in a 0.1 M KOH solution saturated with oxygen, with 5 mV s^{-1} scan rate, rotating the WE at various speed from 400 to 2400 rpm. The oxygen reduction reaction was investigated performing the scans between 1 and 0.4 V vs RHE.

5.2.2 Fuel cell testing

In the first place, the Membrane Electrode Assembly (MEA) was prepared. The catalyst-coated gas diffusion electrode (GDE) method was used for fabricating the AEMFC electrodes. ETFE-based RG-AEI powder (containing benzyl trimethylammonium (BTMA) functional groups with an ion-exchange capacity (IEC) of 1.26 ± 0.06 mmol g^{-1}) synthetized by the group of prof. J. Varcoe, from the university of Surrey,[88] was ground with a pestle and mortar for 10 min. For each cathode GDE, the catalyst powder and the AEI powder (the latter always set to 20 wt % of the total solid mass) were mixed together with 1 mL of water and 9 mL of propan-2-ol. This cathode catalyst ink was homogenized with ultrasound for 30 min and then sprayed onto a Toray TGP-H-60 carbon paper gas diffusion substrate (Alfa Aesar, 10%

poly(tetrafluoroethylene) (PTFE)) using an Iwata spray gun, with intermittent (<10 s) drying on a hotplate (80 °C) and weighing to ensure correct loadings. For the anode GDEs, Pd-CeO_2/C was used as a catalyst (along with 20 wt % AEI). All electrodes and RG-AEMs (made from the radiation grafting of 10 μM HDPE (electron-beamed to 100 kGy absorbed dose) with a vinyl benzyl chloride monomer (a mixture of 3- and 4-isomers) followed by amination with aqueous TMA (45 wt %), IEC = 2.56 mmol g^{-1}) [89] were immersed in an aqueous 1M KOH solution for 1 h, with an exchange of the KOH solution with fresh solution midway through, and then washed thoroughly in ultrapure water (UPW, to remove excess KOH), before assembly into a 5 cm^2 fuel cell fixture (Scribner Associates) using a 5 N m torque.

-**Fuel Cell Performance Data Collection**. An 850e fuel cell test station (Scribner Associates) was used for testing and data collection. The fuel cell temperature was varied between 60 and 80 °C. H_2 and O_2 gas feeds with flow rates of up to 1 and 2 L min^{-1} (SLPM) were supplied to the anode and the cathode, respectively, with no back-pressurization. At 80 °C cell temperature, the dewpoint for both the anode and cathode gas supplies was 76 °C (calculated relative humidity (RH) = 85%). All followers (heated lines between the fuel cell tester and the fuel cell fixture) were heated to prevent premature condensation before the entry of humidified gases into the flow field. The MEAs were activated by discharging the cell at a constant voltage of 0.5 V during cell heating and leaving the cells at this voltage until a steady current density was observed. Beginning-of-life AEMFC performance data were collected under controlled galvanostatic discharge steps, where data (at each current density) was recorded after the potentials had stabilized. The internal ohmic resistances were estimated using the 850e instrument's internal current interrupt method.

5.3 Result and discussion

As discussed in chapter 3.1.1 all catalysts were used as-prepared in laboratory, except for Pt(40%)/C that is commercially available. Platinum catalysts were studied extensively for ORR in AEM fuel cell, proving a favored $4e^-$ pathway mechanism [90]. From what concern the anode, Pd-CeO_2/C exhibits enhanced HOR activity under alkaline conditions with an HOR Tafel slope of 60 mV dec^{-1} and an exchange current density of 20 A g_{Pd}^{-1} (Figure 5.2a); it also can be seen that the mass transport limited current plateau for hydrogen oxidation is reached at ca. 100 mV overpotential.

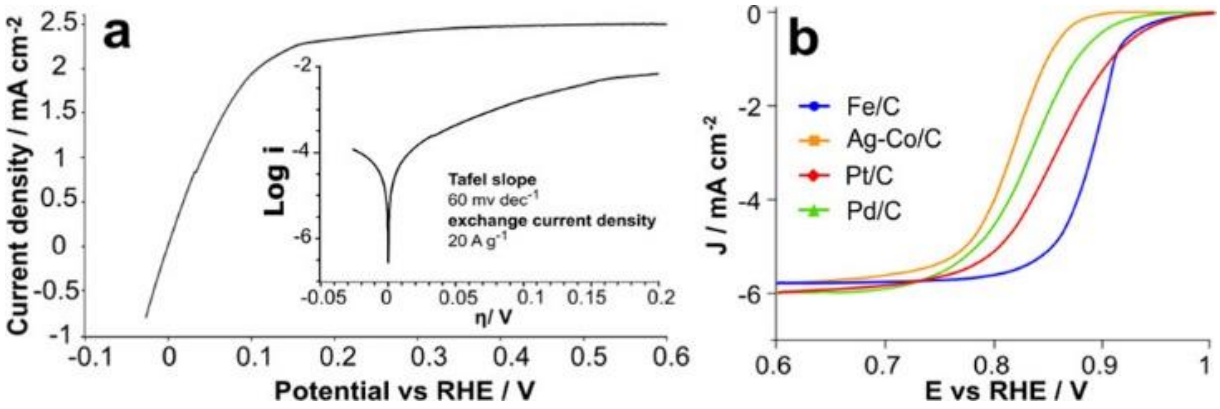

Figure 5.2: (a) Electrochemical HOR activity (RDE linear sweep voltammetry (LSV) at 1 mV s^{-1} 1600 rpm with the Tafel analysis inset) of Pd-CeO_2/C in H_2 saturated aqueous 0.1 M KOH (WE loading of 4 µg of Pd); (b) polarization curves for the ORR. Experimental conditions: KOH 0.1 M, O_2 saturated, RDE LSV at 5mV s^{-1} 1600 rpm.

The electrochemical activity of Pt/C, Pd/C, Ag-Co/C, and Fe/C for the ORR in O_2-saturated 0.1 M KOH was investigated by linear sweep voltammetry at room temperature (18−22 °C) using a rotating disk electrode (RDE); ORR polarization curves of the various cathode are compared in Figure 5.2b, while in Figure 5.3 are shown the measures carried out a various rotation speed, from these, the number of electrons involved during the reaction was compared at different potential, by using Kouteky-Levich plot (Figure 5.3). All cathodes show selectivity for the $4e^-$ ORR, and Pt/C has the best onset potential. Interestingly, the CRM-free Fe/C material shows excellent attributes such as a low Tafel slope, an early onset potential, and $4e^-$ ORR mechanism.

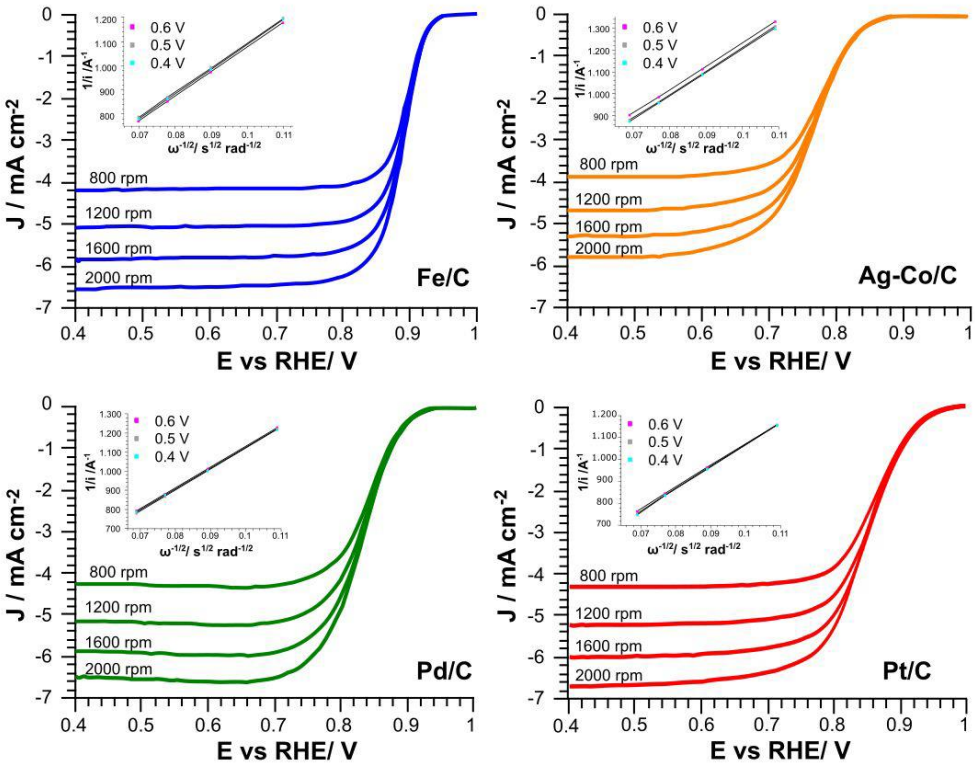

Figure 5.3: ORR polarization curves at different rotating speeds and the corresponding K-L plots (inserts). All cathodes show selectivity for the 4e⁻ ORR, and Pt/C has the best onset potential. Interestingly, the CRM-free Fe/C material shows excellent attributes such as a low Tafel slope, an early onset potential, and 4e⁻ ORR mechanism.

Relevant electrochemical parameters for the ORR catalyzed by the materials investigated in this work are listed in Table 5-2.

Table 5-2: Electrochemical Parameters for the ORR Determined by LSV (O_2-Saturated 0.1 M KOH)

Catalyst	ORR n° e⁻	Tafel slope mV/dec 1600 rpm	E_{onset} V vs RHE 1600 rpm	E@1/2 J [V] 1600 rpm
Pt/C	4.0	60	0.944	0.853
Pd/C	4.0	49	0.907	0.834
Ag-Co/C	4.0	47	0.843	0.766
Fe/C	3.9	49	0.928	0.889

As shown in previous work, switching from using LDPE to more crystalline HDPE as a thin RG-AEM substrate led to a remarkably improved overall performance in simple single-cell AEMFC tests,[89] with enhanced tensile properties and in situ durability. The current hypothesis (still to be fully explained) is that the thin HDPE-AEM exhibits rapid H_2O transport characteristics, meaning that high current densities can be sustained, as high AEMFC performances rely heavily on the back-diffusion of electrogenerated

water from the anode to the cathode (where H_2O is a faradic reactant in the alkaline ORR). In Table 5-3 are summarized the main characteristics of the HDPE-AEM used in this study. Another key development that is partly responsible for the recently reported improvements in AMFC performance is the RG-AEI powders that allow high ionic conductivity and water transport in the catalyst layers of GDE-type electrodes [88].

Table 5-3: main characteristic of HDPE-AEM.

	HDPE-AEM	ETFE-based RG-AEI
IEC (mmol g^{-1})	2.56 ± 0.28	1.26 ± 0.06
average thickness (μm)	25 ±2	94 ± 55 a
water uptake (%)	22 ± 15	b
thickness swelling and area swelling (%)	22 ± 9 and 20 ± 2	b
Cl^- conductivity at 60 °C in water (mS cm^{-1})	40.8 ± 2.8	b

[a]: Average RG-AEI particle size. [b]:Not easily determined, as not in the membrane form.

5.3.1 AEMFC TESTING

Catalysts were deposited at the desired loading onto Teflon-treated Toray paper GDL by aerographic deposition of ink composed of catalyst particles and (insoluble) ionomer powder (20 wt % dry). A summary of metal loading use is given in Table 5-4. Prior to cell testing, the (AEI-containing) electrodes and the HDPE-AEM were soaked in an aqueous 1 M KOH solution for 1 h to replace Cl^- counter ions with predominantly OH^- anions (with trace HCO_3^-/CO_3^{2-} as no CO_2 was excluded) in the AEM.

Table 5-4: Summary of AEMFC test conditions and key performance parameters.

Catalyst	catalyst loading/metal loading (mg cm^{-2})	thickness GDL + catalyst layer μm (sd)	@ 0.6 V W cm^{-2} (A cm^{-2})	peak performances W cm^{-2} (A cm^{-2})	current density @ 0.1 V (A cm^{-2})
Pt/C	1.0/0.40	220 (4)	1.2 (2.0)	2.0 (5.0)	7.5
Pd/C	2.5/0.25	230 (8)	0.72 (1.2)	1.3 (3.9)	6.5
Ag-Co/C	1.8/0.75 (Ag)	220 (9)	0.54 (0.9)	1 (3.6)	6.0
Fe/C	1.0/0.03	190 (10)	0.43 (0.71)	0.96 (2.7)	4.0

Pd-CeO_2/C anode containing 0.25 mg_{Pd} cm^{-2}, all electrodes containing 20 wt % ETFE-based RG-AEI with inks sprayed on Toray TGP-H-60 10% PTFE, and HDPE-based RG-AEM ca. 25 μm thick when hydrated.

The electrodes and the HDPE-AEM were then washed with UPW to remove excess K^+ co-ions and OH^- counter ions before assembly in the fuel cell hardware. The HDPE-AEM was sandwiched between the anode and cathode electrodes and pressed between the graphite flow fields using appropriate gaskets to optimize the compression and sealing (no ex-situ hot pressing was performed). The exact test conditions used to obtain fuel cell data are summarized in Table 5-4. All gases were supplied without back-pressurization. The MEAs were "activated" via operation at 0.5 V until a steady current was achieved (minimum of 1 h). During the experiments, the cell temperature, gas humidification, and flow regime were adjusted to reach a suitably stable cell performance.

The fuel cell polarization and power density curves obtained for MEAs are shown in Figure 5.4 with important performance parameters summarized in Table 5-4. First, stable open-circuit voltages (OCVs) ranging from 0.9 to 1 V suggest that the ultrathin HDPE-AEM is now showing excessive resistance to gas crossover. The ranking of cathode catalyst performances in terms of power densities and maximum current densities is Pt/C > Pd/C >Ag/C ≈ Fe/C. The use of the fuel-cell grade Pt/C benchmark enables the MEA to produce a maximum power density of 2.0 W cm^{-2} with the ability to discharge at 7.5 A cm^{-2} (at 0.10 V).

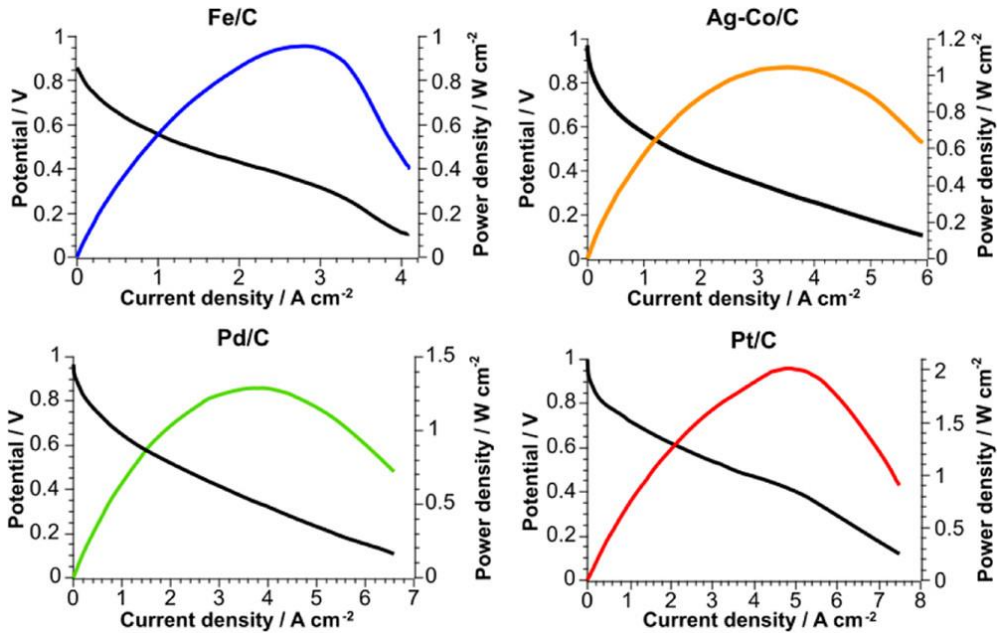

Figure 5.4: H_2/O_2 (1 SLPM/2 SLPM) AEMFC performance data with the Pd-CeO_2/C anode catalyst (0.25 mg cm^{-2} Pd loading) and various cathode catalysts. Both electrodes contain 20 wt % ETFE based RG-AEI powder. The cell temperature was 80 °C (apart from the Fe/C test, which was limited to 60 °C due to cathode thermal stability limitations).

The same anode and cathode combination is limited to 1.4 W cm^{-2} under the same cell conditions using an LDPE-based RG-AEM membrane (of comparable thickness but made using a lower crystallinity substrate), highlighting the importance of membrane characteristics toward obtainable fuel cell performance [91]. The replacement of the Pt/C cathode with an in-house synthesized Pd/C catalyst (Pd diameter ca. 2 nm, 10 wt % loading) produced a peak power of 1.3 W cm^{-2}. To obtain a metal loading approaching that of the Pt electrode (60% compared to the Pt electrode), larger quantities of the catalyst are required, which ultimately creates large mass transport limitations and increased ohmic resistances.

Figure 5.5a shows the change in the ASR of the MEAs over the course of the power curves shown in Figure 5.4. The effect of increased catalyst layer thickness on fuel cell performance is seen for Pd/C compared to Pt/C (approx. 35 and 30 Ω·cm^2, respectively). The Fe/C electrode has the highest ASR (40−50 Ω·cm^2) but at the same time has the thinnest catalyst layer (Table 5-4).

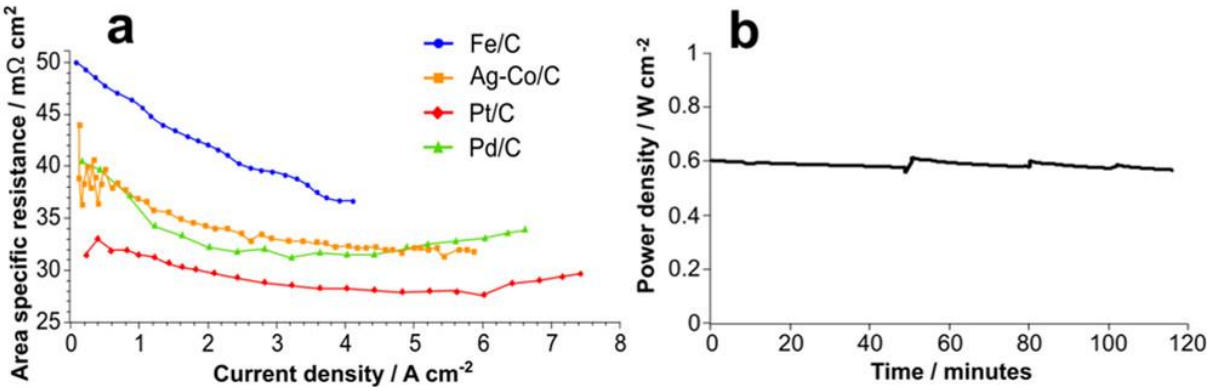

Figure 5.5: (a) Change in area-specific resistance (ASR) with current density during power curves; (b) short-term AEMFC stability test at 80 °C: discharge at 1.0 A cm^{-2}, H_2/O_2 (0.1:0.2 SLPM). Dewpoint for the anode and cathode gas supplies was 60 °C. Pd-CeO_2/C anode catalyst (0.25 mg cm^{-2} Pd loading) and Pt (0.4 mg cm^{-2} Pt loading).

During the LSV testing described above, Fe/C outperformed the Ag and Pd materials and had a comparable activity to the Pt/C cathode suggesting that a low metal loading reduces the effective fuel cell performance. Ultimately, the challenge lies in increasing the active-site concentration in the Fe/C catalyst to around 10−20 wt %. This will avoid the need for excessive catalyst loading and increases in catalyst layer thickness. The Ag-Co/C catalyst performed adequately (ca. 1 W cm^{-2}) but required a higher metal loading (0.75 mg_{Ag} cm^{-2}). The CRM-free Fe/C catalyst (3 wt %) achieved a comparable

peak power density to the precious-metal Ag-Co/C cathode. The electrode containing Fe has a much lower metal loading (0.03 mg_{Fe} cm^{-2}) with a sustainable and cheaper source metal, US $580,000 for Ag versus US$90 for Fe (prices per metric ton). It is essential to operate fuel cells (including AEMFCs) at high cell voltages to maximize efficiencies, so we also highlight the power and current densities obtained at a 0.6 V cell voltage (Table 5-4). The best cathode catalyst in this regard is clearly Pt/C with threefold the current density obtained with the non-PGM Fe/C and Ag-Co/C catalysts. Performance stability remains a key parameter to be optimized for AEMFCs, which depends on the chemical and mechanical durability of the AEM and AEI polymer electrolytes, catalyst durability, and maintaining optimal catalyst|AEI|AEM interfaces. A preliminary short-term stability study was undertaken with the best performing MEA (the Pd-CeO_2/C anode catalyst and the Pt cathode). The cell voltage remained stable for 2 h at a respectable 1 A cm^{-2} constant current density (Figure 5.5b). This stability test also used realistic fuel feeds (0.1 and 0.2 SLM for the anode and the cathode, respectively).

5.4 Conclusions

In this work, membrane electrode assemblies for anion exchange membrane fuel cells (AEMFCs) were prepared and tested. For the first time, a Pd-CeO_2/C anode catalyst has been combined with both Pt and non-Pt cathodes, including a critical resource material (CRM)-free exemplar. To obtain high AEMFC performances, it was crucial to use high-performance polymer electrolyte components: an HDPE-based radiation grafted anion exchange membrane along with the ETFE-based radiation-grafted ionomer powder (in the electrodes) was used in this study. The availability of such materials enables catalyst developers to more realistically evaluate new catalysts in AEMFC tests. As an example, it was shown that Pd-CeO_2/C with a low Pd loading is a viable alternative to the commonly used PtRu/C anodes allowing for peak power densities up to 2 W cm^{-2} to be obtained. This catalyst can be paired with both Pt and non-Pt cathode catalysts. Quite importantly, a CRM-free cathode (composed of cheap Fe as the metal component) gave an interesting power density (1 W cm^{-2}) in a H_2/O_2 AEMFC operated at 60 °C. Note that, this particular Fe/C catalyst did not show stable performance in an AEMFC operating at 80 °C. However, AEMFC funding in the EU and UK is considering the use of AEMFCs in non-automotive applications (i.e., as “silent” non-fossil fuel-based replacement for diesel electric generators), hence

operating at <80 °C is a valid proposal (the developing US DOE AEMFC automotive focused targets are not wholly applicable until such catalysts are shown to be stable above 80 °C) [92]. These studies stress that future improvement of AEMFC performances is only possible via the optimized integration of catalytic, electronically conducting, and ionically conducting components, along with evaluation of the durability of all components in combination.

6 Electrolysers

6.1 Ru-complex catalysts for hydrogen evolution reaction

6.1.1 Introduction

Molecular catalysts capable to produce hydrogen occur in nature, namely hydrogenase and nitrogenase enzymes. They can evolve hydrogen with very high efficiencies (10^2–10^6 mol_{H2} $mol_{catalyst}^{-1}$ s^{-1})[93,94]. These enzymes contain earth-abundant metal centres like iron and nickel in their active sites. Despite their high activity, these catalysts are not suitable for use on electrochemical devices like PEM-ECs, due to their limited stability in the presence of oxygen, their limited operative range with respect to a very narrow pH and temperature window (pH 7 and 37 °C are the optimal conditions), a bad electrode–catalyst contact that which often requires a redox mediator, as well as difficulties in obtaining sufficient amounts of hydrogen for large scale applications.[95–99] Many efforts have been made in order to mimic and improve natural molecular catalyst, but very few has found a real employment in electrolysis [53,100,101]. In this work, Ru-Ru complex adsorbed onto conductive carbon has been employed as cathode for hydrogen evolution in PEM electrolyser feeded with pure water, showing remarkable stability along the entire measure This material was used to assemble a polymer exchange membrane electrolysis cell fed with pure water. This device is capable to evolve H_2 (28 L_{H2} g_{Ru}^{-1} min^{-1}) with a turnover frequency (TOF) of 7800 mol_{H2} $mol_{catalyst}^{-1}$ h^{-1} and remains stable without loss of activity for at least 7 days.[102]

6.1.2 Experimental

All experiments were performed under an inert atmosphere of argon using standard Schlenk and vacuum line techniques or in an MBraun glove box. *N,N'-*

dimethylethylenediamine was purified by vacuum distillation. Dry solvents were obtained from an Innovative Technology solvent purification system and stored under argon. Deuterated solvents were purchased from Eurisotope and Cambridge Isotope Laboratories Inc., distilled with the proper drying agent and stored under argon with 3 Å (acetonitrile, ethanol[D6]) 4 Å (other solvents) molecular sieves.

Crystallographic structures

X-ray diffraction experiments were performed on a XtaLAB SynergyDualflex diffractometer, equipped with a Pilatus 300K hybrid pixel detector and a copper (1.5406 Å) microfocus tube and a Bruker D8 Venture Dual source diffractometer equipped with a PhotonII detector, respectively. Suitable crystals were selected, protected by polybutene oil and mounted under a cold nitrogen stream. The crystals were kept at 100 °K during data collection. The data reduction was performed using CrysAlisPro and Apex3, respectively. Using Olex2 [103], the structures were solved with SHELXT [104], followed by least-squares refinement against full matrix (versus F2) with SHELXL.[105] All non-hydrogen atoms were refined anisotropically.

DFT calculations

All calculations were carried out with ORCA 4.2.0.[106] Geometry optimizations were performed at the PBE0-D3BJ/def2-SVP/def2-TZVP(Ru) level of theory.[107–109] Solvent effects were taken into account implicitly by using the cpcm model with water as solvent and a gaussian charge scheme.[110,111] Numerical frequency calculations were carried out to confirm the nature of stationary points found by geometry optimizations. The RIJCOSX approximation was used for density functional theory (DFT) calculations.[112,113] Approximate transition states were generated using the nudged elastic band (NEB) method implemented in ORCA, followed by a saddle-point optimization.

NMR

Solution NMR spectra were recorded on Bruker Avance 500, 400, and 300 spectrometers. The chemical shifts (δ) are expressed in ppm relative to TMS for ^{1}H and ^{13}C. Coupling constants *J* are given in Hz as absolute values. Where a first order analysis is appropriate, the multiplicity of the signals is indicated as s, d, t, q, or m for singlets, doublets, triplets, quartets, or multiplets. The abbreviation br. is given for

broadened signals. Aromatic units are indicated as H^{ar} or C^{ar} when not noted otherwise. Quaternary ^{13}C are indicated as C^{quat}. The olefinic protons and ^{13}C atoms of the two coordinated C=C moieties in dbcot (dibenzo[a,e]cyclooctatetraene) are indicated as H^{olef} and C^{olef}, respectively. The protons and carbon atoms of the diazabutadiene moiety are denoted as H^{dad} and C^{dad}, respectively. [$Ru_2H(\mu$-$H)(Me_2(dad))(dbcot)_2$], [$Ru(\mu$-$H)(Me_2(dad))(dbcot)_2]PF_6$, and [$Ru(OTf)(\mu$-$H)(Me_2(dad))(dbcot)_2$] were synthesized following well know procedures.[54]

ICP

The ICP-OES analysis was performed using a Varian 720 ES ICP-OES with SPS-3 Autosampler. Exhaust solutions were directly injected in the instrument. For calculating the ruthenium content in the **2@C^k** catalyst, 5 mg of the sample were dissolved in a PTFE vessel in 8 mL of aqua regia (6 mL of HCl 37% and 2 mL of HNO_3 conc.). The resulting mixture was then digested in a microwave oven and diluted to 50 mL adding bidistilled water.

Gas chromatography

GC-TCD was measured on an Agilent Technology 7890A GC System on a HP-Molsieve (19091P) column.

Scanning Transmission Electron Microscopy

The scanning transmission electron microscopy (STEM) investigations were performed on the aberration-corrected HD-2700CS (Hitachi; cold-field emitter) or a Jeol F200 equipped with a cold field emission gun and a 16 MPixel camera, both operated at an acceleration potential of 200 kV. On the HD 2700CS, a probe corrector (CEOS) is incorporated in the microscope column between the condenser lens and the probe-forming objective lens providing excellent high-resolution capability (beam diameter ca. 0.1 nm in the selected ultra-high resolution mode). Images (1024 x 1024 pixels) were recorded with a high-angle annular dark field (HAADF) detector with frame times of ca 15 s. These imaging conditions give rise to atomic number (Z) contrast, a highly sensitive method to detect even atoms of strongly scattering elements (high Z) on light supports.

6.1.2.1 Half-cell testing

Measurements were performed following the procedures discussed in paragraph 4.2.1. The ink was prepared suspending $[Ru_2(OTf)(\mu\text{-}H)(Me_2dad)(dbcot)_2]/C$ in ethanol and water in order to obtain a catalyst concentration of 0.53 wt%, also a 5% wt Nafion® solution in 2-propanol was added, in order to act as a binder (Table 6-1); the ink was then sonicated for 1 hour to homogenize the mixture. The working electrode WE was coated with a drop of the catalyst ink (c.a. 9 µL) by means of a micropipette; the final weight was then determined by weighing the dry catalyst; the resulting metal loading onto the WE spans from 6.3 to 7.5 $\mu g_{Ru}\ cm^{-2}$. All the potentials were reported versus the Reference Hydrogen Electrode RHE without compensating the resistance.

Polarization (LSV) experiments were performed in a 1 M H_2PO4^-/HPO_4^{2-} buffer solution (pH 7.4) or 0.25 M $HClO_4$ aqueous solution (pH 0.6) saturated with hydrogen with 1 mV s^{-1} scan rate, rotating the WE at 1600 rpm. HER was investigated performing the scans between 0.1 and -0.5 V vs RHE. Chronoamperometric studies were conducted at the same conditions, keeping the potential at 300 mV vs RHE and rotating the working electrode at 1600 rpm for one hour.

Electrochemical impedance spectroscopy (EIS) measures were carried out in a 0.25 M H_2SO_4 solution, under N_2 atmosphere, with frequency range spanning from 100 KHz to 0.01 Hz. Measures were acquired at OCP condition and at – 300 mV vs RHE, with a DC amplitude of 10 mV. Data were analyzed with Z-view software.

Table 6-1: Ink preparation.

Reactants	Quantity
$[Ru_2(\mu\text{-}H)(Me_2dad)(dbcot)_2OTf]/C^k$ (3.06% wt.Ru)	7.0 mg (0.008 mmol complex)
Milli-Q water	600 mg
EtOH	600 mg
Nafion 5%wt.	12 mg

6.1.2.2 Electrolyser cell testing

The Membrane Electrode Assembly was obtained sandwiching a Nafion 117 membrane between the anode and the cathode in a 5 cm^2 Scribner cell fixture using a 4 Nm screwing torque. The anode was realized mixing in an agate mortar 40 mg of IrO_2 with 20 mg of C^k and 100 mg of a Nafion 5%wt ionomer solution; the resulting

paste was spread onto titanium web (Beakert). The electrode has the 66.6% wt IrO_2 loading (c.a. 7 $mg_{catalyst}$ cm^{-2}) and the 3% wt of pure Nafion amount. Cathodes were obtained mixing 200 mg of the Nafion 5% wt. ionomer with 60 mg of $[Ru_2(OTf)(\mu H)(Me_2dad)(dbcot)_2]$ /C^k catalyst (3.06% wt. Ru or 0.445% wt. Ru); the so obtained dense paste was spread onto carbon cloth (CeTech). The resulting cathode has a total Nafion content of ca. 3.9 wt% and a Ru content of ca. 1 mg_{Ru} cm^{-2} **2@C^k** or 0.04 mg_{Ru} cm^{-2} for the seven-time diluted catalyst **2_{dil}@C^k.** Anodic and cathodic compartments were fed respectively with 50 mL of Milli-Q water and 50 mL of a 0.1 M H_2SO_4 solution or H_2O at 1 mL min^{-1} flow rate. The cathodic vessel head was equipped with a flow meter to quantify the hydrogen produced during the electrolysis experiments.

The electrolysis efficiency in hydrogen production was calculated evaluating the hydrogen evolution reaction faradic efficiency FE as described in Eq 6.1.1.

$$FE = \frac{mol_{H_2}^{real}}{mol_{H_2}^{theoretical}} * 100 \qquad \text{Eq. 6.1.1}$$

The real hydrogen amount produced during the electrolysis was calculated with the flow meter placed at the cell outlet while the theoretic amount was calculated electrochemically applying the Faraday's law (Eq 6.1.2) assuming 100% of coulombic efficiency for hydrogen evolution reaction (HER): I is the current load applied to the cell during the experiment, F is the Faraday's constant (96485.3 C mol^{-1}) and 2 is the number of electrons moles involved in HER.

$$mol_{H_2}^{theorethic} = 2F \int I(t)dt \qquad \text{Eq. 6.1.2}$$

The cell energy consumption required for electrolysis was calculated integrating over time the charging energy and dividing this value with the total hydrogen amount produced (expressed in kg_{H2}) as described in Eq 6.1.3.

$$\boldsymbol{Energy\ consumption}\left(\boldsymbol{KWh\ Kg_{H_2}^{-1}}\right) = \frac{\int \boldsymbol{V(t)I(t)dt}}{\boldsymbol{Kg_{H_2}^{real}}} \qquad \text{Eq. 6.1.3}$$

The electrochemical measurements were performed with an 8 channel Arbin LBT21084 battery test station (Arbin Instrument) potentiostat/galvanostat and the hydrogen amount produced during electrolysis was quantified with a Brockhorst El-Flow (3 mL min^{-1} or 1 L min^{-1}) flow meter.
Polarization experiments were recorded by applying a linear voltage ramp with a 10 mV s^{-1} scan rate between 1.2 to 2.2 V in H_20 or H_2SO_4 0.25 M solution, both at 25 and 80°C. Chronopotentiometry experiments were performed applying a constant electrolysis current of 50 mA/cm^2 at 25 °C, and 400 mA/cm^2 at 80 °C, in pure water and H_2SO_4 0.25 M solution.

6.1.2.3 Model reaction

In situ catalytic turnover

In a J-Young NMR tube with a Teflon screw-cap, $[Ru(\mu\text{-}H)(Me_2(dad))(dbcot)_2]PF_6$ (6 mg, 7.1 µmol, 1 eq.) was mixed with THF-*d*8 (0.4 mL). After recording a ^{1}H-NMR spectrum, KC_8 (1.9 mg, 14 µmol, 2.0 eq.) was added to the top of the tube, which was closed and shaken. A ^{1}H-NMR spectrum was acquired and D_2O (0.15 µL, 7.5 µmol, 1.1 eq.) was added to the tube. After measuring ^{1}H-NMR, H_2SO_4 (50%, 1 drop) was added, and the tube heated to 80 °C for 2 hours during which red crystals formed. NMR shows the formation of a new complex and the crystals were found to be of composition $[Ru(OH_2)(\mu\text{-}H)(Me_2(dad))(dbcot)_2]_3(SO_4^{2-})(HSO_4^-)$.

Verification of Stoichiometric H_2 Production by GC-TCD

In a 10 mL Schlenk tube capped with a rubber septum, $[RuH(\mu\text{-}H)(Me_2(dad))(dbcot)_2]$ (30 mg, 43 µmol, 1 eq.) was dissolved in THF (3 mL). Degassed sulfuric acid (50%, 0.2 mL, 10 eq.) was added, and the stopcock closed. The mixture was heated to 80 °C for 1 hour, before a sample was taken from the headspace via syringe. The sample was subjected to GC-TCD, which allowed the identification of H_2 by its retention time.

Recovery of the exhaust cathode after electrolysis experiments

The exhaust catalyst **2@C^{k}** was recovered after the electrolysis experiments scratching the catalytic powder with a spatula from the electrode; the recovered amount was washed three times with bidistilled water and dried under vacuum at room temperature. The powder was suspended in dry CD_3CN (c.a. 2 mL) by one hour of magnetic stirring under nitrogen atmosphere and the suspension was filtered over a celite plug. The brown filtrate was collected into a 5 mm NMR tube (under nitrogen) and subjected to ^{1}H-NMR analysis (Figure 6.3). The spectrum shows the characteristic (**3c**) signals: (δ 7.46 (s, 2H, CH^{dad}), 7.35-7.18 (m, 2H, CH^{ar}), 7.13-7.02 (m, 2H, CH^{ar}), 6.92-6.85 (m, 8H, CH^{ar}), 6.84-6.74 (m, 2H, CH^{ar}), 6.75-6.61 (m, 2H, CH^{ar}), 4.86 (d, J_{HH} = 9.1 Hz, 2H, CH^{olef}), 4.78 (d, J_{HH} = 9.3 Hz, 2H, CH^{olef}), 4.08 (d, J_{HH} = 8.7 Hz, 2H, CH^{olef}), 4.02 (d, J_{HH} = 8.5 Hz, 2H, CH^{olef}), 2.07 (s, 6H, CH_3), -7.37 (s, 1H, Ru-H)).

6.1.3 Result and discussion

All Ru-Ru complexes were synthetized by the group of professor Grützmacher at the Department of Chemistry and Applied Biosciences at ETH of Zürich.

Due to the low stability of these compounds in the air and water, complex **1** was oxidized with triflic acid, HOTf, in difluorobenzene (DBF) to obtain [Ru_2(OTF)(μ-H)(Me_2-dad)(dbcot)$_2$] **2** (Figure 3.8).[54] The reaction between **1** and aqueous sulfuric acid (50%) or tetrafluoroboric acid (50%) in THF gives after 10 minutes at 65 °C the aquo complexes [$Ru_2(OH_2)$(μ -H)(Me_2dad)(dbcot)$_2$]$^+$(X^{n-}) (X^{n-} = ½ SO_4^{2-}, HSO_4^-, BF_4^-) **3a**. The oxidation with ferrocenium hexafluorophosphate, $FcPF_6$, or ferrocenium tetrafluoroborate, FcBF4, in THF gives a cationic solvato complex [Ru_2(S)(μ-H)(Me_2dad)(dbcot)$_2$]+(X^-) **3b** (S = THF; X^- = PF_6^-, BF_4^-). All reactions proceed under the elimination of H_2. The new compounds **3a** and **3b** are obtained as bright red crystals. Single crystals of **3a** with X^{n-} = HSO_4^-, SO_4^{2-} and those with X = BF_4^- were subjected to an X-ray diffraction analysis. Only the latter gave a data set of sufficient quality to determine the structure with high resolution and a plot is shown in Figure 6.1.

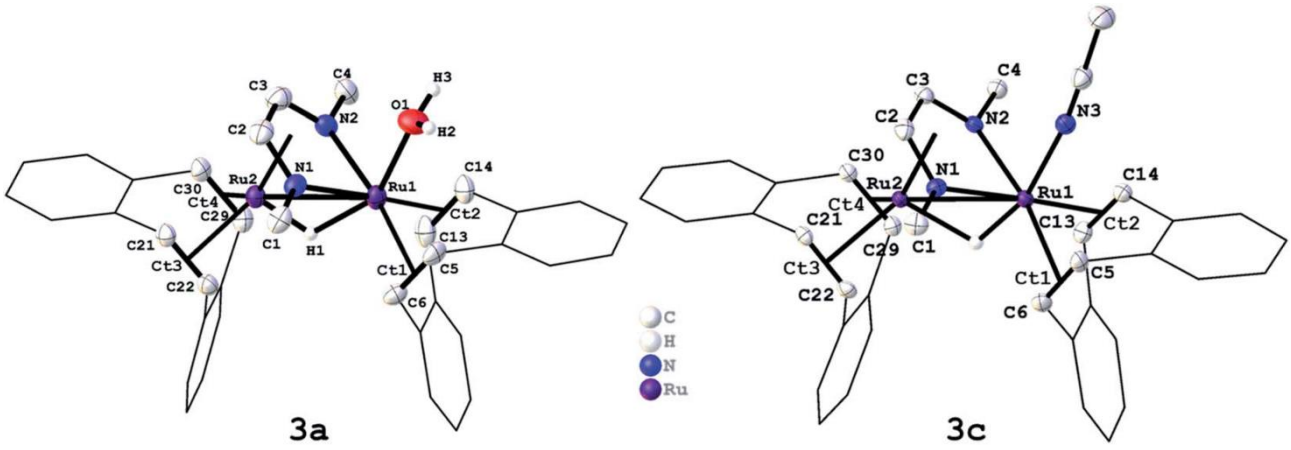

Figure 6.1: Molecular structure of $[Ru_2(OH_2)(\mu\text{-}H)(Me_2(dad))(dbcot)_2]BF_4$ (**3a**, left) and $[Ru_2(NCCH_3)(\mu\text{-}H)(Me_2(dad))(dbcot)_2]BF_4$ (**3c**, right) in the solid state. Ellipsoids are drawn at 50% probability level. Carbon-bound hydrogen atoms, solvent molecules, and the BF4 (**3a**) and PF_6 (**3c**) anions are omitted for clarity.

Like [Fe,Fe] and [Fe,Ni] hydrogenases, these type of dinuclear Ru complexes with redox non-innocent diazadiene ligands show a remarkable structural invariance within the $\{Ru_2(dad)\}$ core. The Ru1–Ru2 bonds in previously reported neutral complex $[Ru_2H(\mu\text{-}H)(Me_2dad)(dbcot)_2]$ **1** with a terminal hydride bound to Ru1 (2.730 Å),[54] triflate complex **2** (2.6730 Å),[54] aquo complex **3a** (2.6892 °A), and solvato complex **3c** (2.6932 Å), they do not present major differences and are at the shorter edge within the range of more than 4000 Ru–Ru bond lengths reported in the CCDC database (2.6–3.2 °A).40 The C–N bonds (1: 1.375 °A; 2: 1.370 Å; 3a: 1.376 °A, 3c: 1.368 Å) and C–C bonds (1: 1.398 Å; 2: 1.402 Å; 3a: 1.406 Å, 3c: 1.397 Å) of the N1–C2–C3–N2 unit indicate a reduced form of the diazadiene (dad) ligand, which in its fully oxidized form can be described as neutral diimine (N=C–C=N: C=N ≈ 1.29 Å; C–C ≈ 1.46 Å) and in its fully reduced form as bis(amido) ethylene (–N–C=C–N–: C=N ≈ 1.38 Å; C–C ≈ 1.35 Å). The positions of the μ_2-hydride ligands were located in the difference map and were freely refined in both structures. The resulting Ru–H bond lengths in the structures of **3a** (Ru1–H: 1.859 Å, Ru2–H: 1.422 Å) and **3c** (Ru1–H: 1.586 Å, Ru2–H: 1.774 Å) are within the usual range of distances found in more than 2800 Ru–H compounds with a Ru–(μ_2H)–Ru fragment. The mean value of 1.78 Å is in good agreement with the DFT-calculated bond length in **3a** (Ru1–H: 1.738 Å, Ru2–H: 1.754 Å). It is important to notice that hydrogen centers in the proximity of a metal atom are not accurately determined with data from X-ray diffraction experiments which also explains the rather large range of Ru–H distances reported in the CCDC database (1.4–2.2 Å).

The Ru1-$NCCH_3$ bond length of 2.073 Å in **3c** is within the range of > 1800 Ru-$NCCH_3$ bond lengths reported in the CCDC database (1.98 – 2.42 Å) and is comparatively short.[114] The Ru1–O bonds in **2** (2.189 Å) and **3a** (2.180 Å) are within the range of more than 500 Ru-OH_2 bond lengths reported in the CCDC database (2.05 Å – 2.365 Å).[114] In comparison to the Ru-$NCCH_3$ bond of **3c**, the Ru-O bond of **2** and **3a** is more than 0.1 Å longer. This observation is in accord with the lability of the triflate anion or water ligand in **2**/**3a** which can be easily replaced by coordinating solvent molecules like acetonitrile (ACN) to give **3b** or **3c**. Hence the ^{1}H-NMR spectra of the triflate complex **2** (Figure 6.2) and aquo complexes **3a** (Figure 6.3 and Figure 6.4) in CD_3CN as solvent are identical to the ^{1}H-NMR spectra of the solvato complexes **3c** (Figure 6.5), while free water is observed in the spectra of **3a**. A characteristic deshielded signal at δ = –7.4 ppm is observed for the bridging H nucleus. In the dihydride complex **1**, this signal is shifted by about 6.5 ppm to higher frequencies (δ = – 0.74 ppm; $THF[D]_8$).

Also, in less coordinating solvents like THF, the terminal coordination site is partially occupied by solvent and partially by triflate (**2** and **3b** in equilibrium) or water (**3a** and **3b** in equilibrium), as described in the literature for **3b**.[54] Acetonitrile replaces the triflat anion or water molecule from the terminal coordination site. The NMR spectra in acetonitrile show only one species which is the same for **2**, **3a** and **3b** and thus is assumed to be $[Ru(\mu\text{-}H)(NCCD_3)(Me_2(dad))(dbcot)_2]^+$ (**3c**).

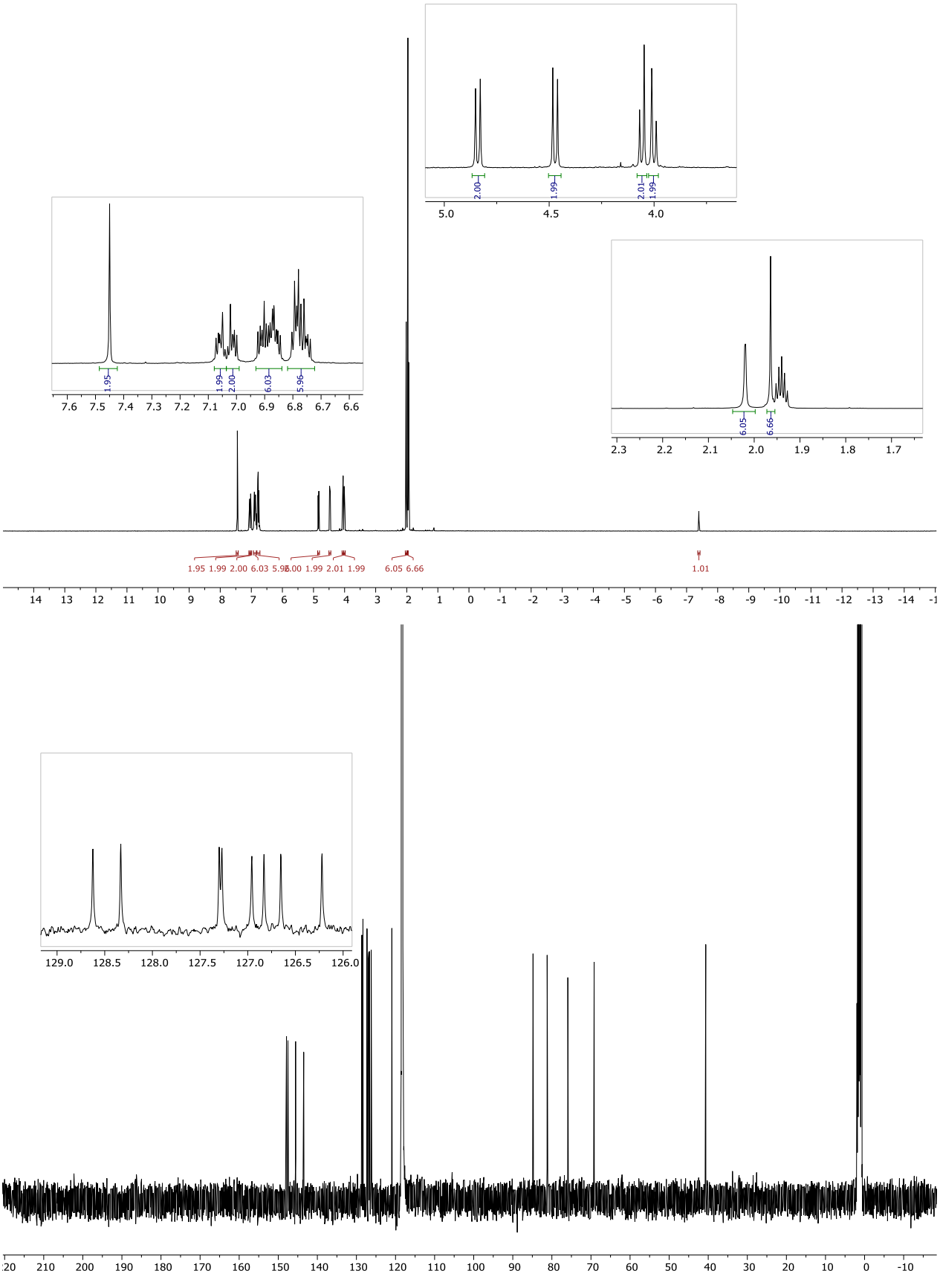

Figure 6.2: ^{1}H- (top) and ^{13}C- (bottom) NMR spectra of $[Ru(NCCH_3)(\mu\text{-}H)Me_2(dad))(dbcot)_2]OTf \cdot 2CH_3CN$ (**3c**), formed from 2 recrystallized in CH_3CN).

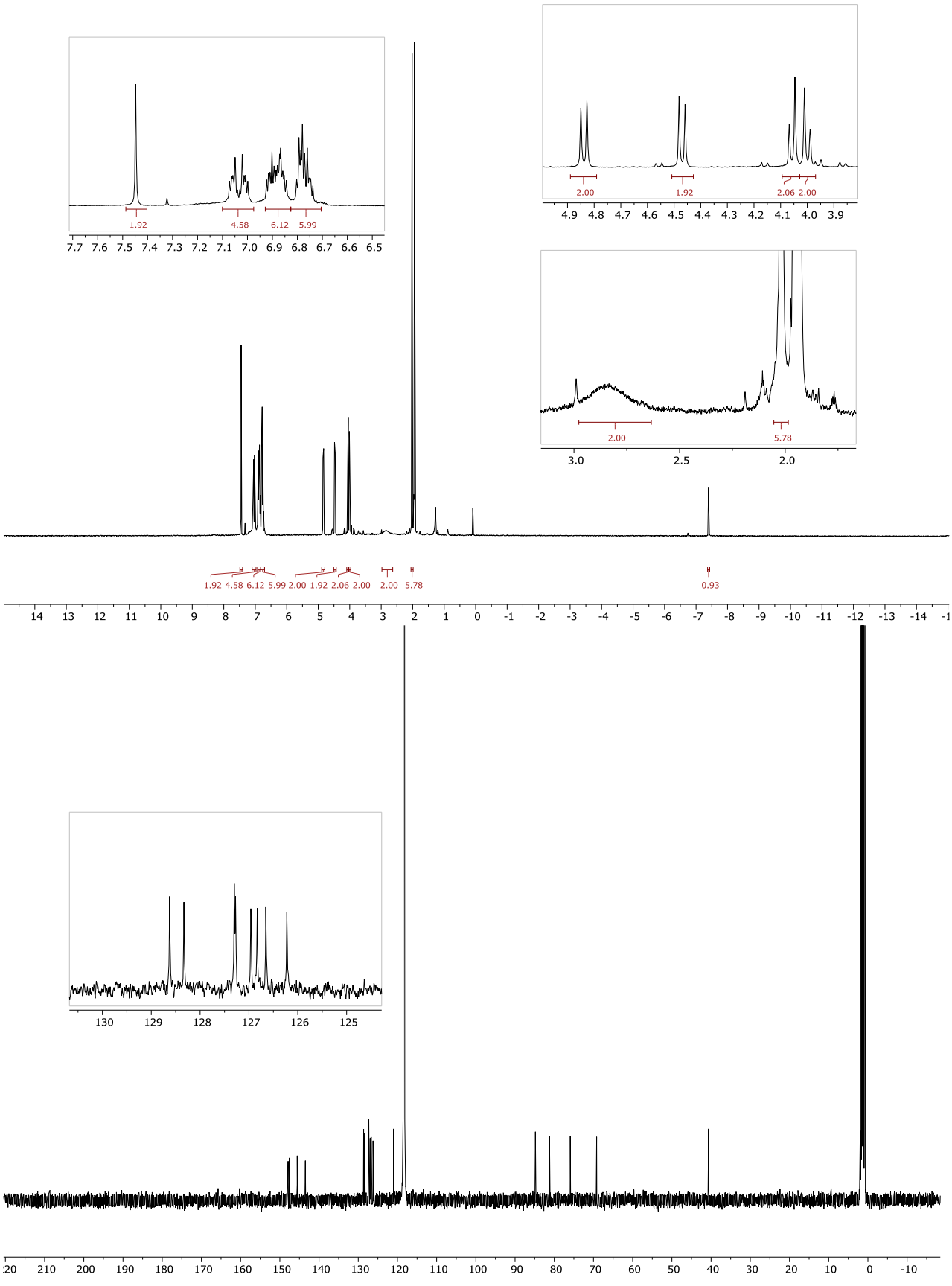

Figure 6.3: ^{1}H- (top) and ^{13}C- (bottom) NMR spectra of $[Ru(OH_2)(\mu\text{-}H)(Me_2(dad))(dbcot)_2]_3BF_4$ (**3a**) in CD_3CN (in-situ forms **3c** and free H_2O).

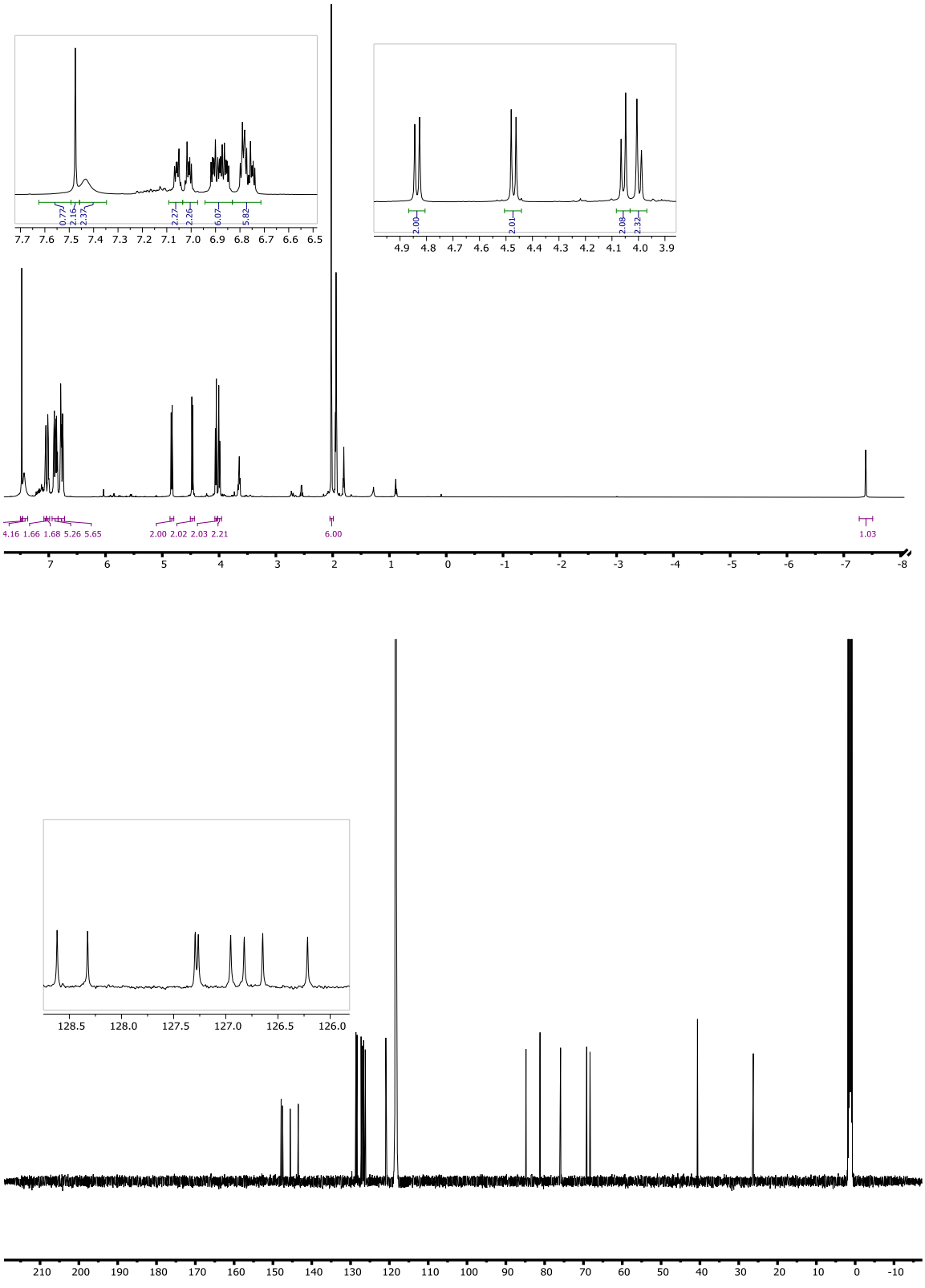

Figure 6.4: ^{1}H- (top) and ^{13}C- (bottom) NMR spectra of $[Ru(OH_2)(\mu\text{-}H)(Me_2(dad))(dbcot)_2]_3(HSO_4)(SO_4)\cdot 0.34\ THF\cdot H_2SO_4$ (**3a**).

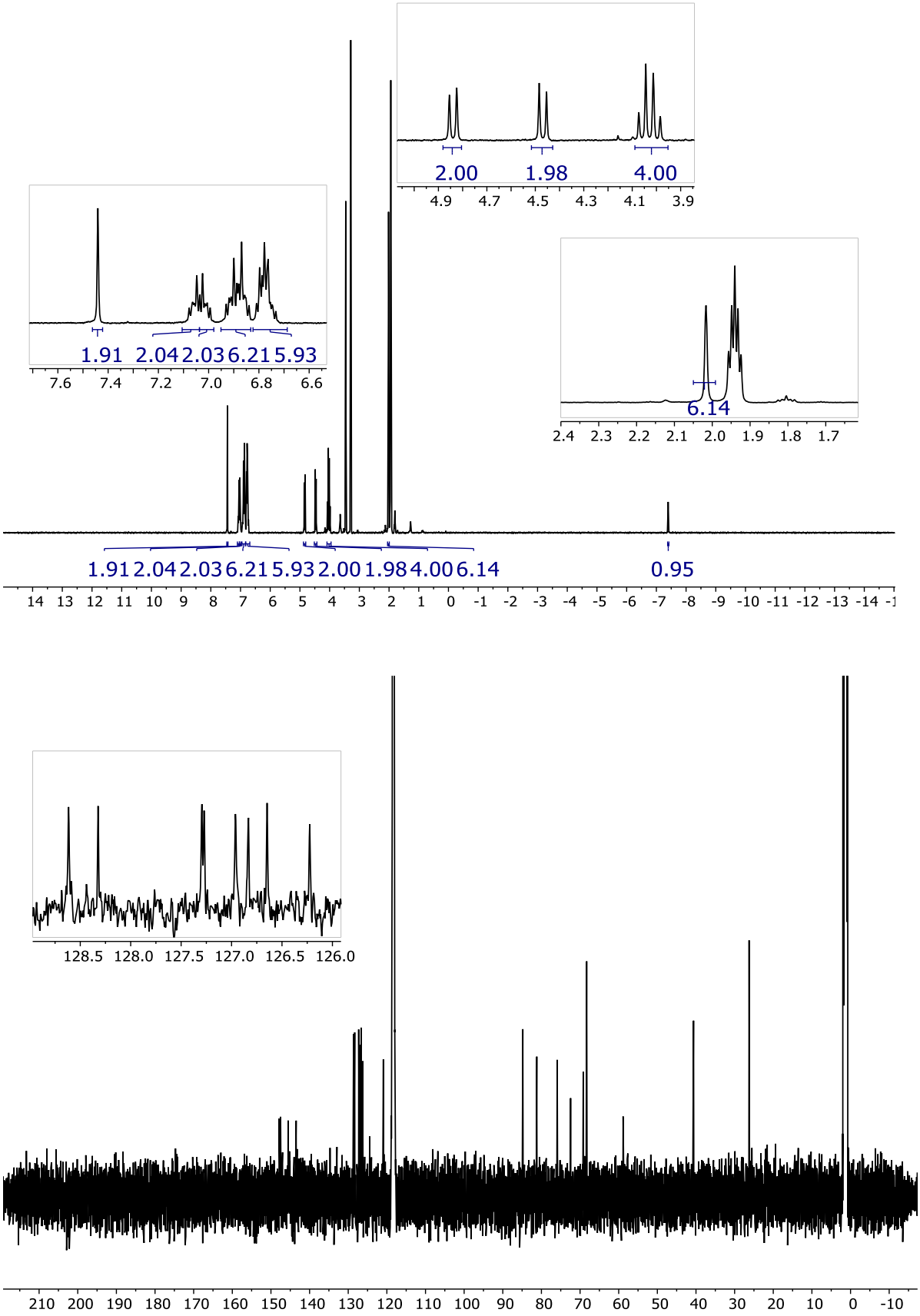

Figure 6.5: ^{1}H- (top) and ^{13}C- (bottom) NMR spectra of $[Ru(OH_2)(\mu\text{-}H)(Me_2(dad))(dbcot)_2]_3(HSO_4)(SO_4)\cdot 0.34\ THF\cdot H_2SO_4$ (**3a**).

The aquo complexes **3a** and the acetonitrile complex **3c** were investigated by thermal gravimetric analyses which showed that all compounds are thermally stable up to >230 °C, temperature at which they begin to lose water (**3a**) or ACN (**3c**) (Figure 6.6, Figure 6.7 and Figure 6.8). Moreover, TGA data suggest that in the solid, H_2O is indeed coordinated to the complex and not just co-crystallised.

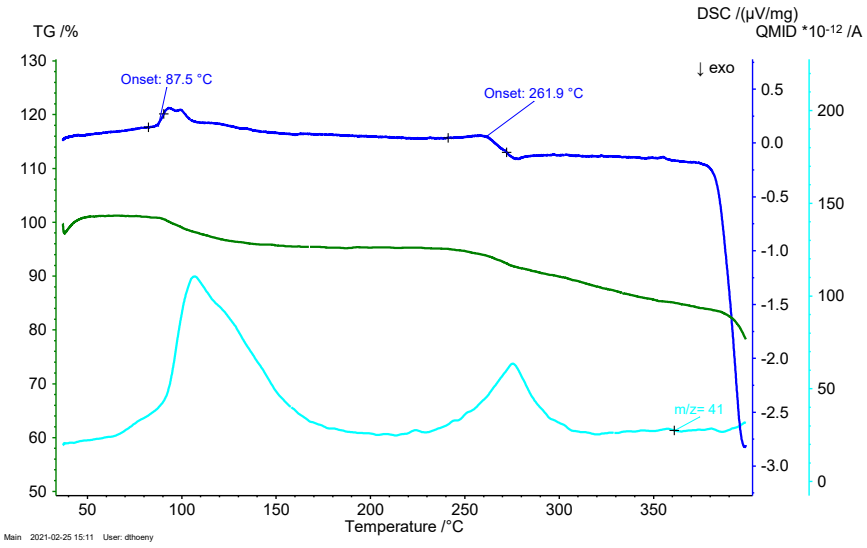

Figure 6.6: Thermal gravimetric analysis (green) and differential scanning calorimetry (deep blue) experiment of $[Ru(NCCH_3)(\mu\text{-}H)Me_2(dad))(dbcot)_2]OTf{\cdot}NCCH_3$ (**3c**) at a heating rate of 7 K/min. Mass trace of acetonitrile (m/z = 41, light blue). At an onset temperature of 87.5 °C, the co-precipitate acetonitrile evaporates. At an onset temperature of 262 °C, the coordinated acetonitrile is lost and the complex decomposes.

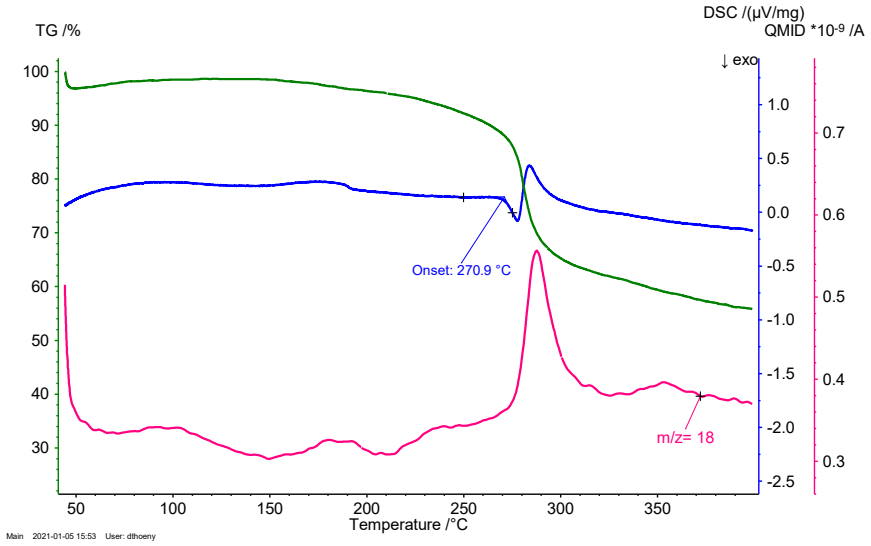

Figure 6.7: Thermal gravimetric analysis (green) and differential scanning calorimetry (blue) experiment of $[Ru(OH_2)(\mu\text{-}H)(Me_2(dad))(dbcot)_2]_3(HSO_4)(SO_4)$ (**3a**) at a heating rate of 7 K/min. Mass trace of water (m/z = 18, pink). At an onset temperature of 271 °C, the coordinated water is lost and the complex decomposes.

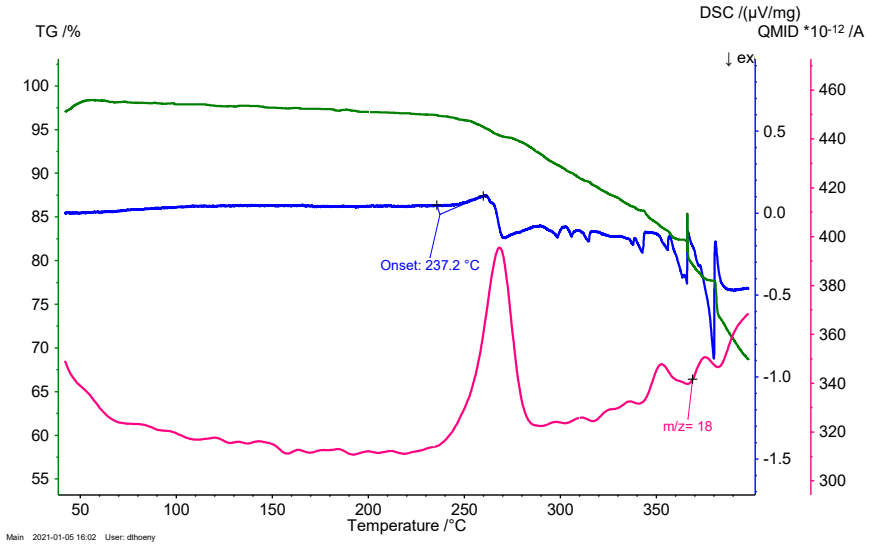

Figure 6.8: Thermal gravimetric analysis (green) and differential scanning calorimetry (blue) experiment of $[Ru(OH_2)(\mu\text{-}H)(Me_2(dad))(dbcot)_2]BF_4$ (**3a**) at a heating rate of 7 K/min. Mass trace of water (m/z = 18, pink). At an onset temperature of 237 °C, the coordinated water is lost and the complex decomposes.

The complexes $[Ru_2(OTf)(\mu\text{–}H)(Me_2dad)(dbcot)_2]$ (**2**) or $[Ru_2(OH2)(\mu\text{–}H)(Me_2dad)(dbcot)_2]^+(X^{n-})$ (**3a**) were adsorbed onto conductive carbon support Ketjenblack EC-600 JD (**C^k**), following a well-established wet impregnation procedure.[50,55–57] Two different electrocatalyst concentrations were used, one

designated as **2@C^k** with a 3.06 wt% of Ru and one with a sevenfold lower catalyst loading (0.44 wt% Ru) designated as **2$_{dil}$@C^k**. These electrocatalytic materials can be readily applied in a MEA by standard techniques and subsequently assembled in a PEM electrolysis test cell. It was assumed that the molecular complex adsorption onto **C^k** is driven through CH-π interactions between the protons at the benzo groups of the dibenzo[a,e]cyclooctene (dbcot ligand) and the 6π-electron system of the C_6 rings of the carbon support.[115] KetjenBlack has a very high surface area, 1400 $m^2\ g^{-1}$, due to a high pore volume and carbon porosity and thus favors high dispersion of the isolated **2@C^k** molecules.[50]

6.1.3.1 Electrochemical characterization

The electrochemical HER activity was firstly investigated in a three-electrode set-up by deposition of **2@C^k** onto a glassy carbon disk electrode (6.3 – 7.5 $\mu g_{Ru}\ cm^{-2}$ loading). Linear Sweep Voltammetry (LSV) and chronoamperometric experiments were performed in 0.25 M $HClO_4$ (pH 0.6) and in 1 M $H_2PO_4^-/HPO_4^{2-}$ buffer solution (pH 7.4). As shown in Figure 6.9a, **2@C^k** achieves a higher mass activity at pH 0.6: -8.56 mA μg_{Ru}^{-1} were recorded at -600 mV vs. RHE respect the 1.04 mA μg_{Ru}^{-1} recorded at pH 7.4 (at -600 mV vs. RHE). HER tafel slopes were determined under acidic and neutral conditions, 135 mV dec^{-1} at pH 0.6 and 132 mV dec^{-1} at pH 7.4, respectively. Ketjenblack EC 600 JD has a negligible activity for the HER reaction (Figure 6.9b and Figure 6.9c). Chronoamperometric experiments at a constant applied potential of -300 mV (RHE) demonstrate the stability of **2@C^k** for hydrogen evolution over 1 hour of water reduction (Figure 6.9d).

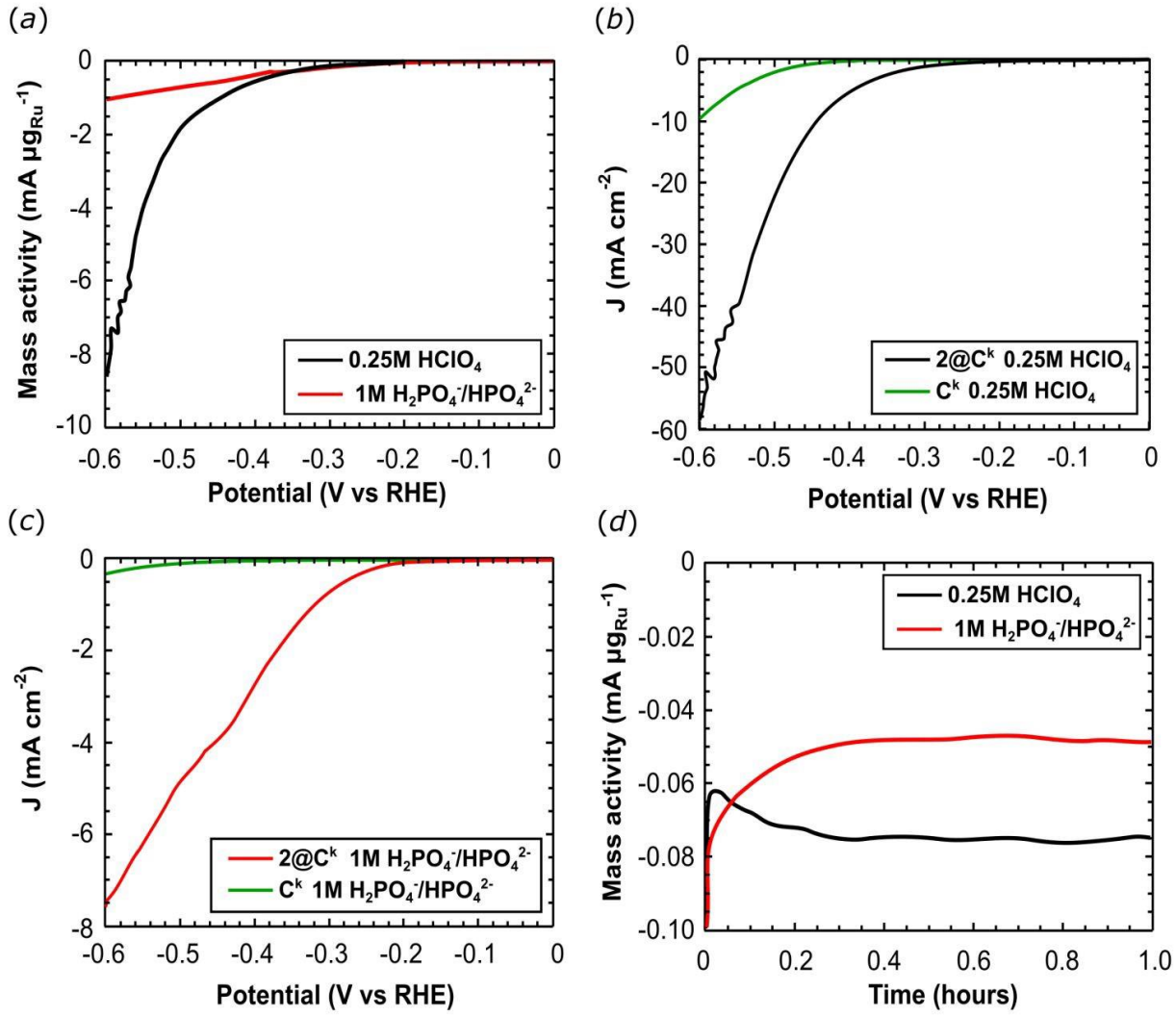

Figure 6.9: Electrochemical characterization of a glassy carbon electrode coated with **2@C^K**. (a) LSV in 0.25 M $HClO_4$ (black line) and 1 M $H_2PO_4^-/HPO_4^{2-}$ buffer (red line); (b) LSV in 0.25 M $HClO_4$ and (c) in 1 M $H_2PO_4^-/HPO_4^{2-}$ buffer solution of **2@C^K** (black line and red line) and pure **C^k** (green line). (d) Chronoamperometry at the constant voltage applied of -300 mV vs. RHE in 0.25 M $HClO_4$ (black line) and 1 M $H_2PO_4^-/HPO_4^{2-}$ buffer (red line). All LSV were acquired at 1 mVs^{-1} scan rate; all the half-cell electrochemistry was acquired with a 1600 RPM working electrode rotation.

A constant current of ca. -75 μA μg_{Ru}^{-1} was recorded at pH 0.6, corresponding to 1.7 μmol of H_2 produced with a turnover number (TON) of 135 mol_{H2} mol_{cat}^{-1}. While -50 μA μg_{Ru}^{-1} were recorded at pH 7.4, with the production of 1.0 μmol of H_2 and a TON = 71 mol_{H2} mol_{cat}^{-1}. Electrochemical impedance spectroscopy (EIS) measurements produced Nyquist plots for **2@C^k** and pure **C^k** under hydrogen evolution at -300 mV vs RHE (Figure 6.10a and Figure 6.10b) and open circuit potential (Figure 6.10c and Figure 6.10d).

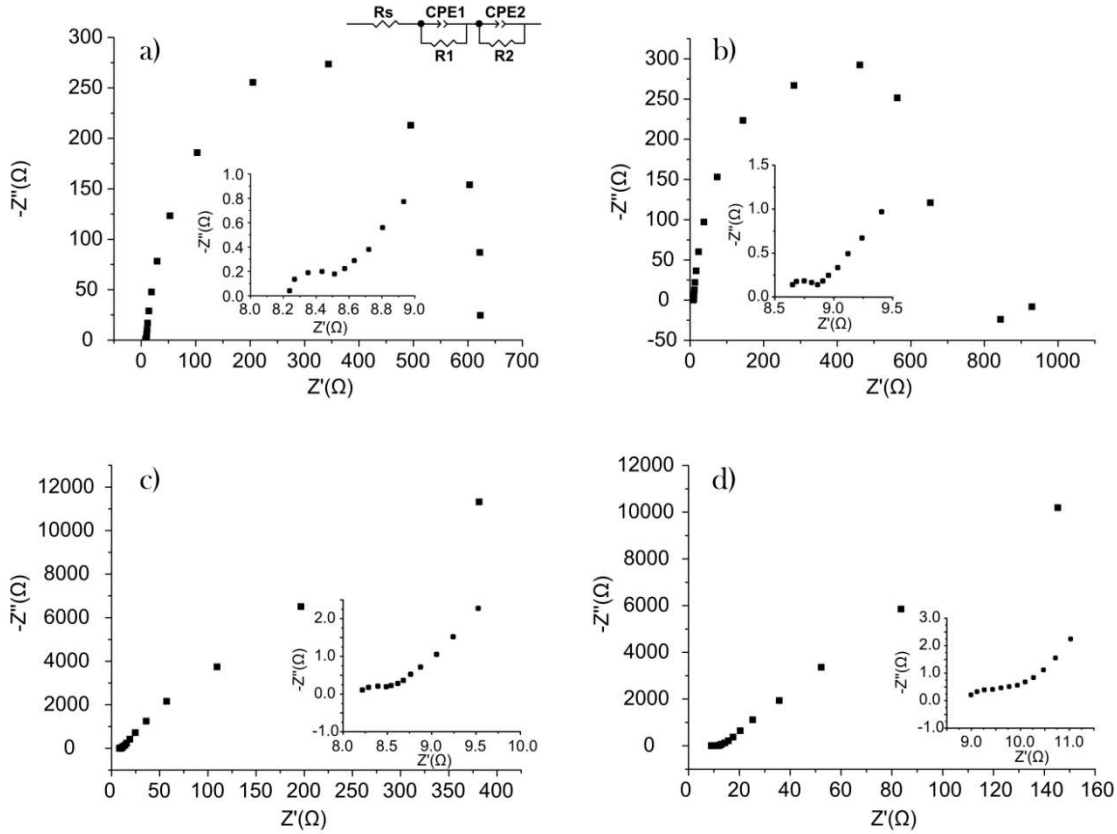

Figure 6.10: Nyquist plot of (a) **2@C^{k}** and (b) **C^{k}** at -300 mV vs RHE. (c) Nyquist plot of **2@C^{k}** and (d) of **C^{k}** at open circuit potential.

Carbon black component of the catalyst provides the major contribution to the EIS spectra, while the Ru complex contributes poorly due to its high dispersion and the low ruthenium content in the catalytically active material. Diffusion phenomena are predominant under open circuit conditions.

6.1.3.2 Electrolyser tests

In the second phase of these studies, the behavior in the complete cell was analyzed, to do so, an ink composed of **2@C^{K}** and Nafion® ionomer (14 wt%) was applied onto a 5 cm^2 carbon cloth electrode support (1 mg_{Ru} cm^{-2}; 9.8 μmol_{Ru} cm^{-2}) and used as a cathode. Combined with a Nafion® 117 membrane and an IrO_2 anode, this assembly was tested in an organometallic PEM water electrolyser (Figure 6.11).

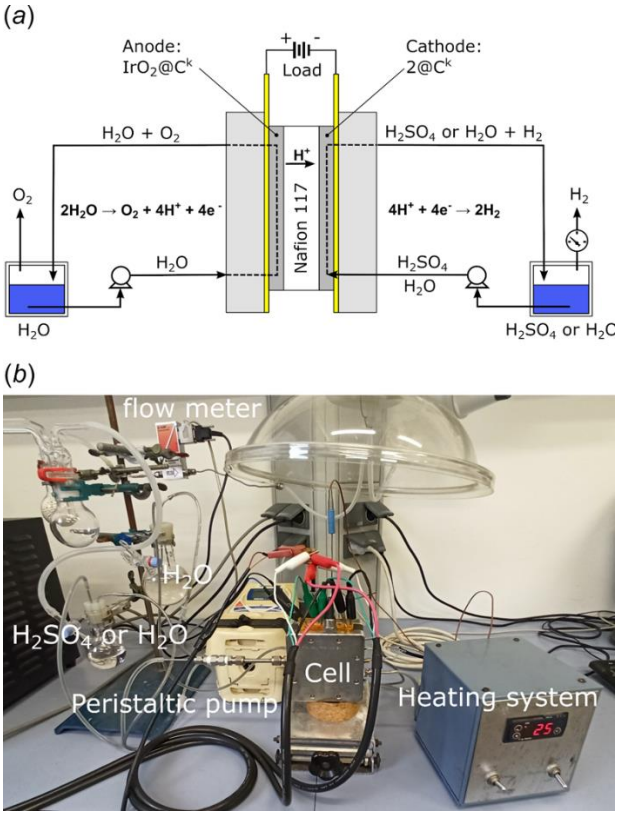

Figure 6.11: (a) Scheme of the electrolysis test cell experimental set up. (b) Picture of the electrolysis test station.

The cell cathode was fed using pure water or a 0.1 M H_2SO_4 aqueous solution. Cell voltage scans were acquired at 25 °C (Figure 6.12a, Table 6-2, entry 1 and 4) and 80 °C (Figure 6.12b, Table 6-2, entry 2 and 5). General performance improves when the solution is switched from pure water feed to 0.1 M H_2SO_4. Phosphoric acid act as additional proton source improving proton migration inside the thick electrode layer (ca. 100 μm) of **2@C^k** providing evidence that the catalyst layer structure requires further optimization in order to fully exploit all active sites of the deposited catalyst. In 0.1 M H_2SO_4 solution, a current density of 310.2 mA cm^{-2} flows in the cell at 25 °C (Table 6-2, entry 4) which increases to 1330 mA cm^{-2} at 80 °C (Table 6-2, entry 5). In the cell fed with water, about half of these current densities were recorded [170.4 mA cm^{-2} at 25 °C (Table 6-2, entry 1); 752.4 mA cm^{-2} at 80 °C (Table 6-2, entry 2)].

A constant current load was applied to the cell for 24 hours (galvanostatic experiments) and the MEA voltage and the hydrogen produced were measured: 0.25 A (50 mA cm^{-2}) were applied to the PEM–ECs operating at 25 °C (Figure 6.12c, Table 6-2, entries 1 and 4) while 2 A (400 mA cm^{-2}) were applied to the cells operating at 80 °C (Figure 6.12d, Table 6-2, entries 2 and 5). At low temperature, the cell produces 3.0 L_{H2} min^{-1}

m^{-2} (87% Faradaic efficiency) which results in a TON of 5.6×103 mol_{H2} mol_{cat}^{-1} using 57.9 kWh kg_{H2}^{-1} of electric energy (see Table 6-2, entry 1). The performance of the cell was evaluated during the first 24 hours of operation, which gives a TOF^{24h} of 230 mol_{H2} mol_{cat}^{-1} h^{-1}. Similar results were obtained using an acidic electrolyte: The hydrogen production rate amounts to 2.9 L_{H2} min^{-1} m^{-2} (86% Faradaic efficiency), leading to a TON of 5.5×103 mol_{H2} mol_{cat}^{-1} (TOF^{24h} = 229 mol_{H2} mol_{cat}^{-1} h^{-1}) at an electric energy consumption (see Eq 6.1.1) of 60.1 kWh kg_{H2}^{-1} (Table 6-2, entry 4). Increasing the operating temperature to 80 °C improves the hydrogen production rate without affecting the stability of **2@C^k**: 23 L_{H2} min^{-1} m^{-2} (83% Faradaic efficiency) were evolved from the cell fed with neutral water with a TON = 4.1×10^4 mol_{H2} mol_{cat}^{-1} (TOF^{24h} =1700 mol_{H2} mol_{cat}^{-1} h^{-1}). In a cell fed with 0.1 M H_2SO_4, 24 L_{H2} min^{-1} m^{-2} (85% Faradaic efficiency) were produced which results in TON = 4.2×10^4 mol_{H2} mol_{cat}^{-1} (TOF^{24h} = 1800 mol_{H2} mol_{cat}^{-1} h^{-1}; see Table 6-2, entries 2 and 5).

Table 6-2: Data for water electrolysis in a complete electrolysis cell operating under acidic and neutral conditions.

Entry	Cat	Water feed	Temp (°C)	J @ 2.2 V (mA cm^{-2})	Time (h)	Current load (mA cm^{-2})	Flow H2 (L min^{-1} m^{-2})	TON	TOF24h (h^{-1})
1	**2@C^k**	H_2O	25	170.4	24	50	3.0	$5.6*10^3$	230
2	**2@C^k**	H_2O	80	752.4	24	400	23.0	$4.1*10^4$	1700
3	**2_{dil}@C^k**	H_2O	80	345.5	168	250	12.1	$1.3*10^6$	7800
4	**2@C^k**	0.1 M H_2SO_4	25	310.2	24	50	2.9	$5.5*10^3$	229
5	**2@C^k**	0.1 M H_2SO_4	80	1330.0	24	400	23.6	$4.2*10^4$	1800

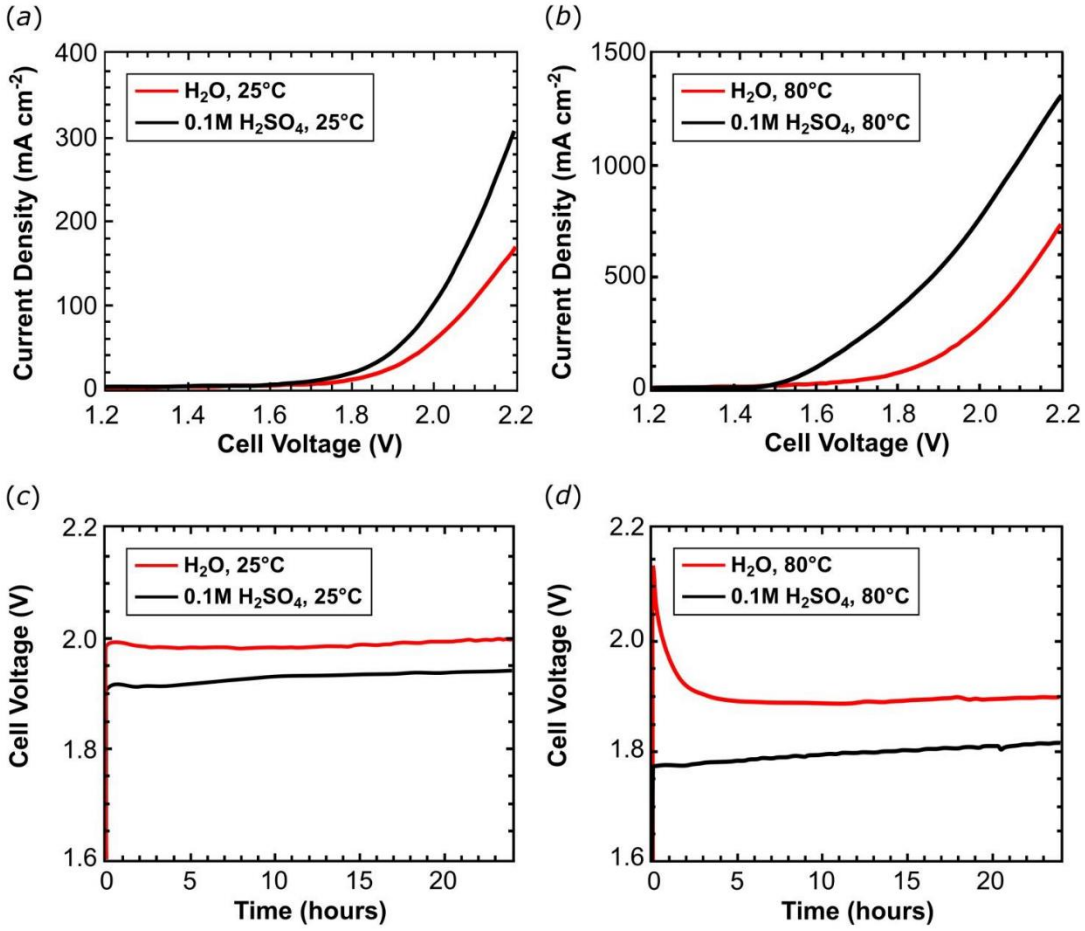

Figure 6.12: Potentiodynamic curves recorded at 25°C (a) and at 80°C (b), in acidic (black) and neutral water (red line) with a 10 mV s^{-1} scan rate. Chronopotentiometric experiments recorded at 25°C applying a 50 mA cm^{-2} current load at 80 °C (c) or applying a 400 m A cm^{-2} current load performed (d) under acidic (black line) or neutral conditions (red line).

Due to its scarcity and price, ruthenium is not suitable for being a material to be exploited on an industrial scale, and its application is only compatible with a sustainable energy management at very low metal loadings. Therefore, the amount of the ruthenium complex on the support material was reduced by 23 times to give $\mathbf{2_{dil}@C^k}$ as cathode material with a metal loading of only 0.043 mg_{Ru} cm^{-2} (0.42 μmol_{Ru} cm^{-2}). Experiments were performed at 80 °C feeding the cathode with pure water. A current density of 345.5 mA cm^{-2} was obtained at 2.2 V (Table 6-2, entry 3, and Figure 6.13a) during scan voltage tests. The current obtained is approximately half of that achieved with the $\mathbf{2@C^k}$ cathode containing 1 mg_{Ru} cm^{-2} under the same conditions (pure water at 80 °C). The cell was operated at 0.2 A cm^{-2} for 168 hours (one week) and no voltage increase was recorded (Figure 6.13b). The cell with $\mathbf{2_{dil}@C^k}$ produces 12.1 L_{H2} min^{-1} m^{-2} of hydrogen (87% faradaic efficiency), with a TON =1.3×10^6 mol_{H2} $mol_{catalyst}^{-1}$ and TOF^{24h} = 7800 mol_{H2} $mol_{catalyst}^{-1}$ h^{-1} as summarized in Table 6-2, entry 3. This activity

is very close to the 8500 mol_{H2} $mol_{catalyst}^{-1}$ h^{-1} achieved by Karunadasa.[116] The current density of **2_{dil}@C^k** (ca. 350 mA cm^{-2} at 2.2 V) is ca. 3.7 times lower than the one reported by Pushkarev *et al* (1300 mA cm^{-2}) at about the same catalyst load (ca. 0.21 µmol cm^{-2} **2_{dil}@C^k** vs. 0.16 µmol cm^{-2} reported by Pushkarev [100]). But Pushkarev's cathode shows a drop of the current density by 50 – 70 mA cm^{-2} during 24 hours of electrolysis at 2.2V. In contrast, **2_{dil}@C^k** is stable over 7 days of electrolysis at 80°C using a similar working potential (c.a. 1.95 V at 0.2 A cm^{-2} of current load).

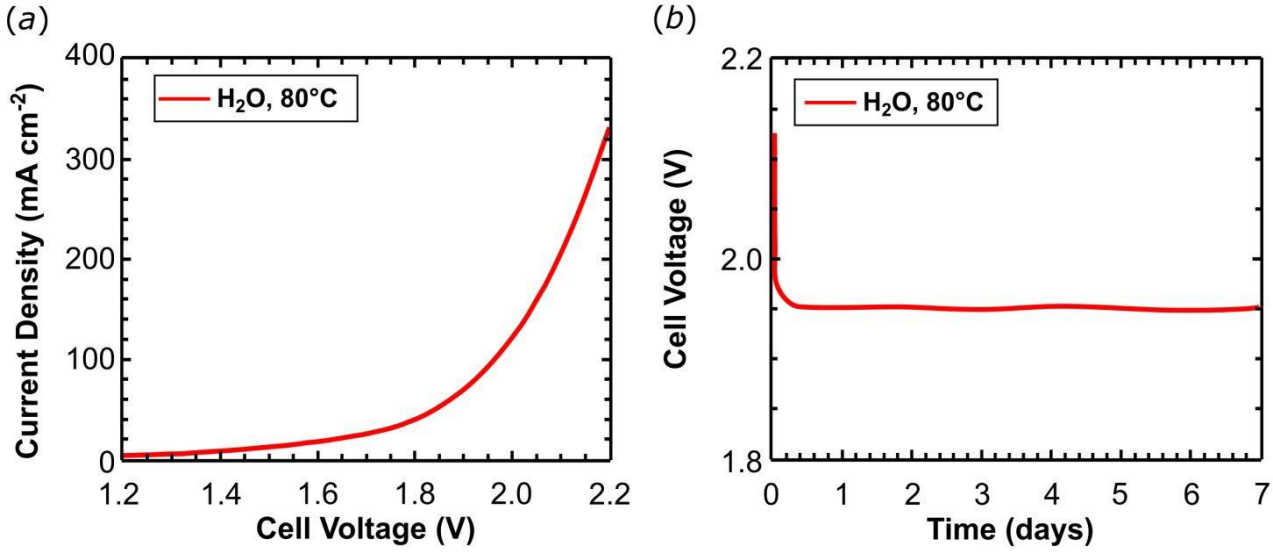

Figure 6.13: Water electrolysis in a complete cell equipped with a cathode containing a metal loading of 0.043 mg_{Ru} cm^{-2}. (a) Potentiodynamic curves recorded at 80°C and 10 mV s^{-1} scan rate. (b) Chronopotentiometric experiments recorded at 80°C at the applied current load of 200 mA cm^{-2}.

Platinum nanoparticle supported onto carbon (Pt/C) represent the state-of-the-art cathodes for hydrogen evolution in PEM electrolysis cells. Pt loadings of ca. 0.5 mg_{Pt} cm^{-2} are generally used in PEM electrolysers that operate at 2 A cm^{-2}. [117] This corresponds to ca. 140 L_{H2} min^{-1} m^{-2} and 28 L_{H2} min^{-1} g_{Pt}^{-1}. The **2_{dil}@C^k** cathode shows the same H_2 production rate of 28 L_{H2} min^{-1} g_{Ru}^{-1} if one considers that the lower operating current density is balanced by the lower metal loading.

The **2_{dil}@C^k** catalyst powder was recovered from the electrode after 168 h of operation and studied by scanning transmission electron microscopy (STEM) imaging. No visible difference was detected between the fresh **2_{dil}@C^k** cathode displayed in Figure 6.14a, and the catalyst after operation, see Figure 6.14b. This finding excludes significant decomposition which would lead to larger Ru nanoparticles. Instead, we assume that

the dinuclear ruthenium complexes appear as globular bright spots with a size of up to 5 Å.

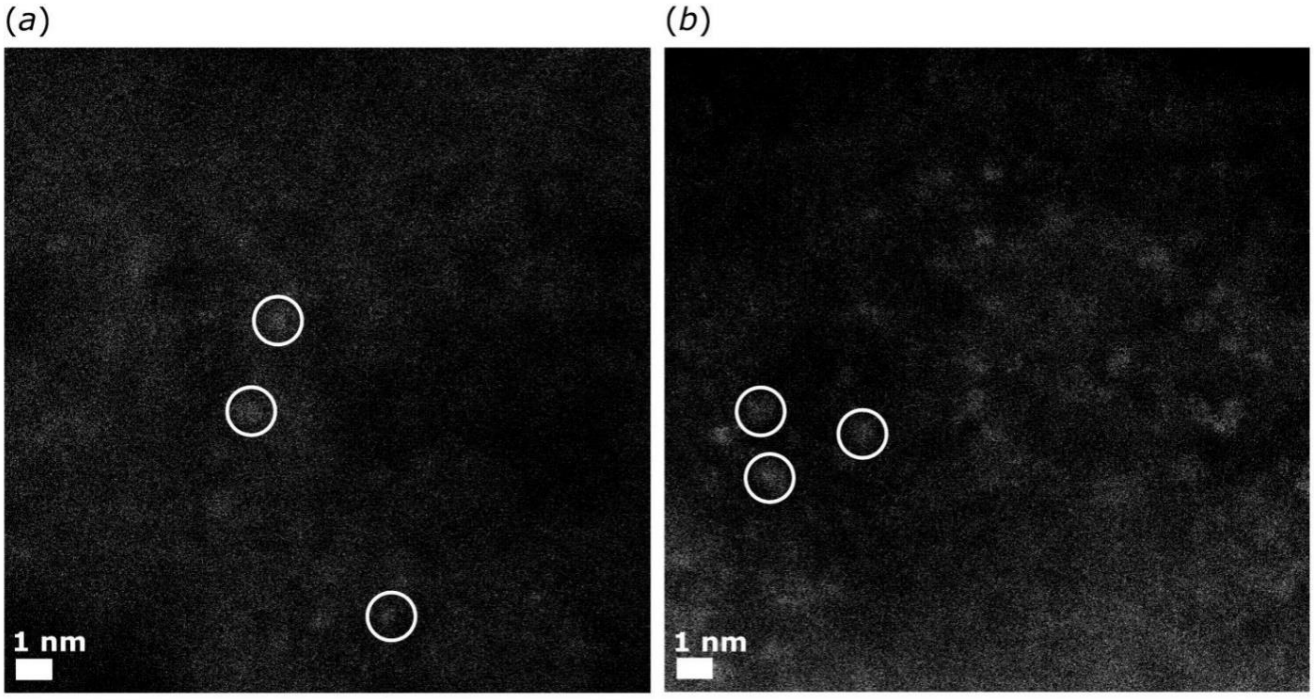

Figure 6.14: HAADF-STEM (Z contrast) images showing the presence of complex **2** molecules as bright spots. High magnification image of $\mathbf{2_{dil}@C^k}$ cathode before (a) and after (b) 7 days of water electrolysis at 80°C in neutral environment; scale bar 1 nm.

An EDXS analysis of these spots (Figure 6.15) confirms the presence of ruthenium. The Ru–Ru distance in the dinuclear Ru complexes **1**, **2**, and **3a** is about 2.7 Å (0.27 nm) and it was assumed that the few larger spots detected by high-angle annular dark-field scanning transmission electron microscopy (HAADF-STEM) may be due to co-precipitates of two or three complex molecules. However, Ru-Ru complexes, spreads well on the $\mathbf{C^k}$.

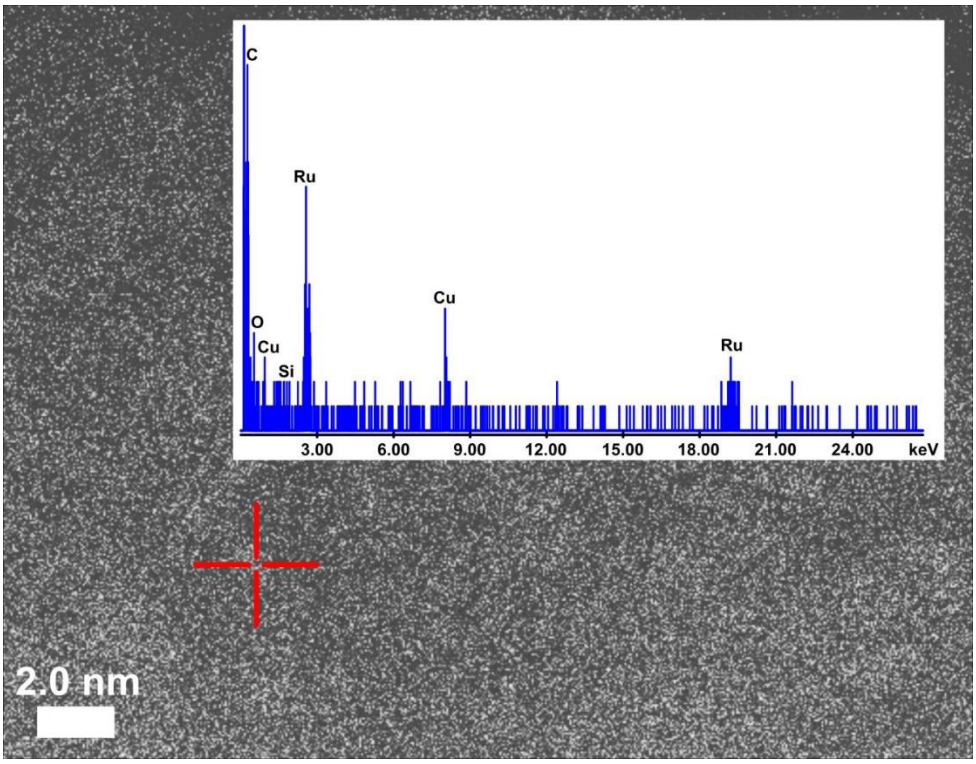

Figure 6.15: High magnification HAADF-STEM (Z contrast) image of $\mathbf{2_{dil}@C^k}$ exhaust cathode, 0.04 mg_{Ru} cm^{-2}. The insert shows the EDXS analysis of the marked spot (red cross) ascribable to the presence of Ru complex molecules.

Soluble components were extracted from the recovered electrode in deuterated acetonitrile. The NMR spectra clearly showed that the dinuclear complex $[Ru_2(ACN)(\mu\text{–}H)(Me_2dad)(dbcot)_2]^+(X^-)$ **3c** is present (Figure 6.16) providing further evidence for the catalyst stability. Inductively coupled plasma optical emission spectroscopy (ICP-OES) was used to determine possible ruthenium leaching into the aqueous phase during operation. After 24 h operation at 2 A cm^{-2} at 80 °C only a trace amount of Ru was detected (230 ppt).

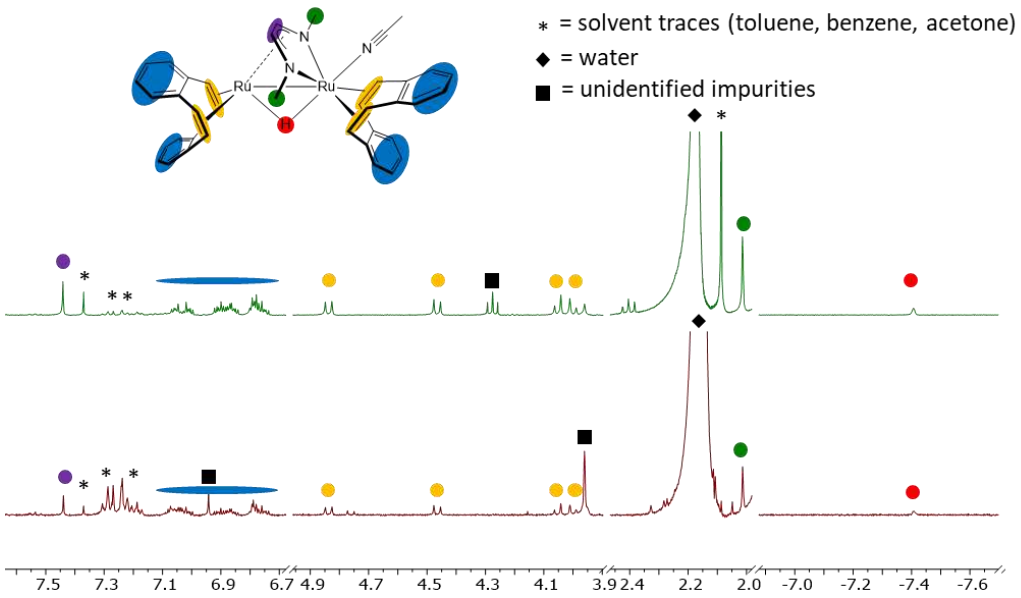

Figure 6.16: ^{1}H-NMR spectra in CD_3CN of complex (**2**) extracted from the fresh **2@C^{k}** cathode (top) and the exhaust **2@C^{k}** cathode (bottom) after 24 hours of electrolysis at pH 1 (0.1 M H_2SO_4 feeding solution). Regions that do not show any signals of interest are not indicated for clarity.

XPS analysis was performed on two different samples: (i) the pristine complex **2** and (ii) the complex extracted with acetonitrile from the **2$_{dil}$@C^{k}** powder recovered from the MEA after 7 days of electrolysis. An extraction process is required because of the limited penetration depth of XPS measurements. This makes it impossible to detect any ruthenium signal arising from the complex in the **2$_{dil}$@C^{k}** embedded in a large excess of Ketjenblack powder. Insoluble carbon black was removed by filtration and the clear solution containing the ruthenium compound was drop-casted onto a slab of gold on mica (rinsed under nitrogen flux). Figure 6.17a and Figure 6.17c depict the XPS spectra in the C1s Ru3d (area filled in green) region of the pristine complex **2** and the complex obtained after extraction of the used electrode material. Figure 6.17b and Figure 6.17d show the spectra in the N1s region. According to the literature,[118–120] the deconvolution of the peak reveals a $Ru3d_{5/2}$ signal, which corresponds to an electron deficient ruthenium species (Ru^{n+}), is found at the same binding energy of 281.4 eV for both, the pristine compound and for the recovered one. So, there is no change in the oxidation state of the Ru in the complex before and after the electrolysis. In addition, no Ru(0) was observed, whose presence would be an indication of complex decomposition to ruthenium nanoparticles. The N1s region (Figure 6.17b and Figure 6.17d) is characterized by a single component at 399.7 eV for the fresh complex and 399.8 for the recovered one. The signal is ascribed to the residual acetonitrile and to

the nitrogen centers in the central Me_2dad diazadiene ligand of the complex. The semiquantitative analysis of the surface chemical composition and the nitrogen/ruthenium ratio are reported in Table 6-3 and are in line with the compound structure.

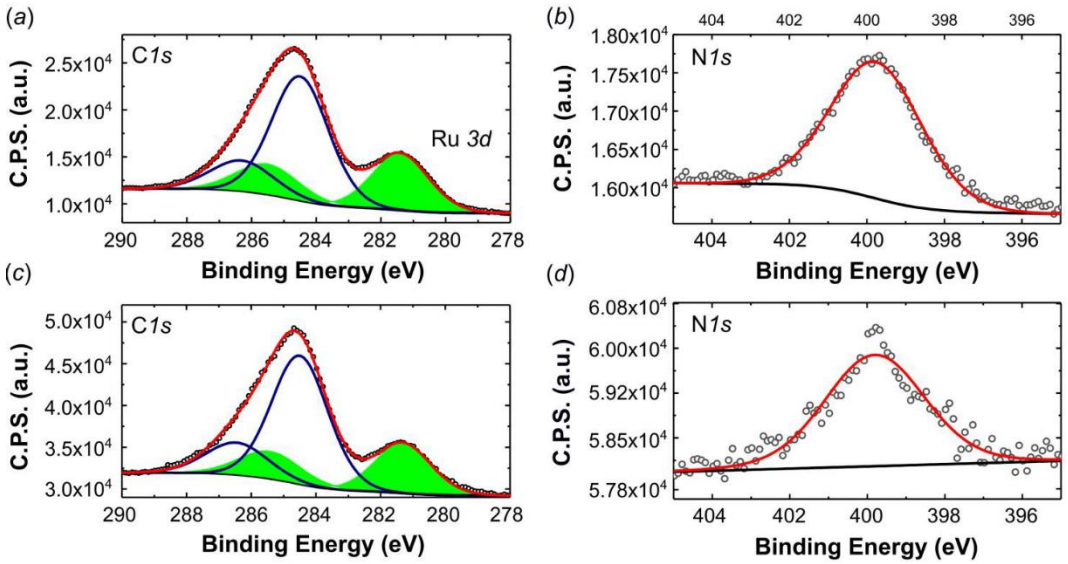

Figure 6.17: High resolution XPS spectra (a) C1s,Ru 3d and (b) N1s of pristine **2** and (c) C1s Ru 3d and (d) N1s of the complex recovered after 7 days of electrolysis.

Table 6-3: Surface composition determined by XPS analysis.

	C*1s*	**N*1s***	**Ru*3d***	**N/Ru**
Theoretical	89%	7%	5%	1.5
Pristine **2**	87.2%	7.3%	5.5%	1.3
Pristine **2** after 7 days electrolysis	87.8%	7.8%	4.5%	1.7

The measured binding energy of 281.4 eV ($Ru3d_{5/2}$) is very close to the values reported for a series of Ru^{2+} and Ru^{3+} organometallic compounds.[121] An usefull comparison of C1s Ru3d and the N1s regions of the XPS spectra was also performed (Figure 6.18) for the mononuclear Ru diazadiene complex $[K(dme)_2][Ru(H)(trop_2dad)]$ ($trop_2dad$ = 1,4-bis(5*H*-dibenzo[*a,d*]cyclohepten-5-yl)-1,4-diazabuta-1,3-diene) with compound **2,** which has a comparable coordination environment and to which a +2 oxidation state was assigned.[122] The $Ru3d_{5/2}$ peaks of compound **2** (281.4 eV) and

[K(dme)$_2$][Ru(H)(trop$_2$dad)] (281.6 eV) have the same shape and very similar binding energies. The difference in shape and binding energy related to the N1s peaks (**2**: 399.8 eV; [K(dme)$_2$][Ru(H)(trop$_2$dad)]: 400.2 eV) is not unexpected in view of the different structures of the ligands. Although these data do not allow to assign precisely the oxidation states of both Ru centers in **2**, it is assumed that they lie in between (+2) and (+3).

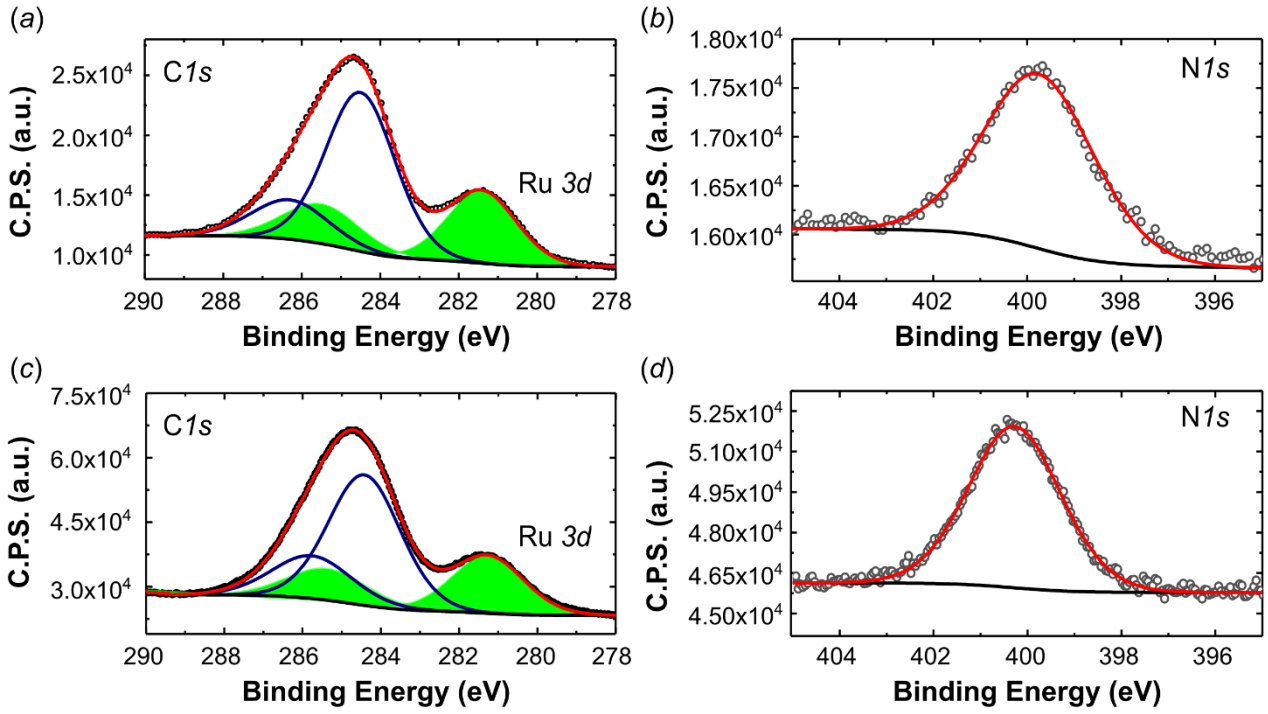

Figure 6.18: High resolution XPS spectra (a) C1s,Ru 3d and (b) N 1s of pristine **2** and (c) C1s Ru 3d and (d) N1s of the [K(dme)$_2$][Ru(H)(trop$_2$dad)] benchmarck compound.

In order to propose a possible mechanism for the catalytic HER, stoichiometric reactions were performed. In addition, DFT calculations were performed in order to support the assumptions drawn from these experiments (Figure 6.20 and Figure 6.21). The air stable complex **3b** (as well as **2** and **3c**) can be reduced by two electrons with two equivalents of KC_8 to give the anionic complex $K^+[Ru_2(\mu\text{-}H)(Me_2dad)(dbcot)_2]^-$ **4** [eq. (1) in Figure 6.20a]. This complex is rather unstable and could not be isolated. In solution and at room temperature, it converts to several ruthenium hydride complexes, which were detected in situ by multi-nuclear NMR spectroscopy (Figure 6.20c). In the presence of D_2O or EtOH[D]$_6$, the complex **4** immediately reacts to form the deuterated complex [RuD(μ–H) (Me$_2$dad)(dbcot)$_2$] (**1**[**D**]) [eq. (2) in Figure 6.20a], which supports the assignment of **4** as anionic metal localized Brønstedt-base. It is worth to notice that

in the protonation reaction only the terminal position at Ru1 is protonated/deuterated and no H/D scrambling of the bridging hydride is observed (Figure 6.19).

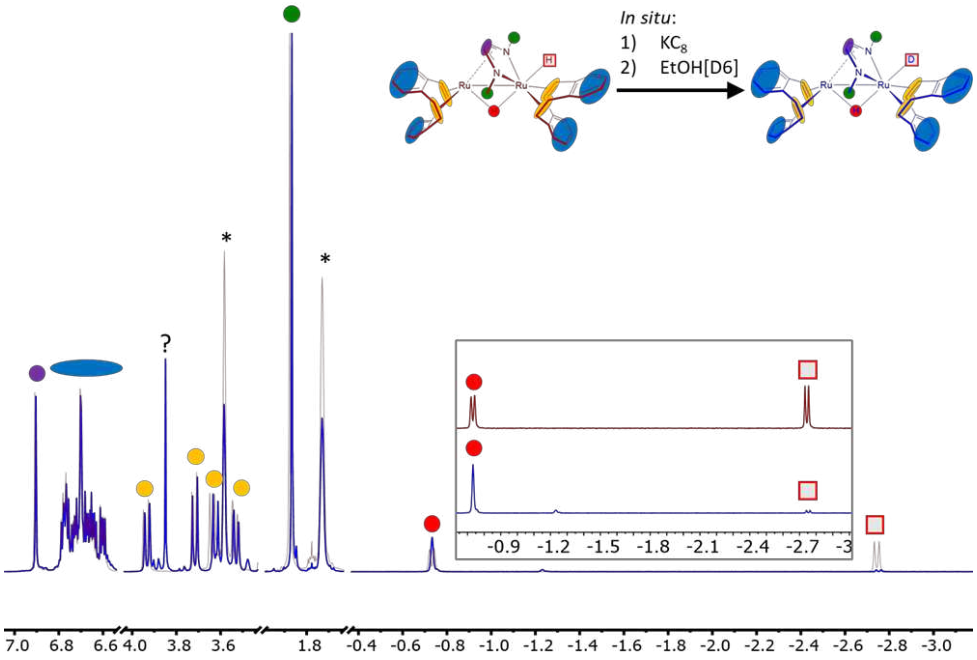

Figure 6.19: Overlaid ^{1}H-NMR spectra of [Ru_2(μ-H)H(Me_2(dad))($dbcot)_2$] **1** (red) and [Ru_2(μ-H)D(Me_2(dad))($dbcot)_2$] **1[D]** (blue).

In homogenous solution in an organic solvent, the neutral dihydride [RuH(μ–H)(Me_2dad)($dbcot)_2$] **1** (which is insoluble in water) does not react with an excess water (five equivalents). No hydrogen is evolved according to, **1** + H_2O -X → [Ru(OH)(μ–H)(Me_2dad)($dbcot)_2$] + H_2, even at 80 °C for several days, and there is no evidence for the formation of a hydroxide complex. The latter also cannot be prepared when the aquo complex **3a** is treated with KOH. However, when **1** is treated with an acid such as aqueous H_2SO_4, dihydrogen gas is evolved [detected by gas chromatography (TCD detector) in the headspace] and the hydridoaquo complex **3a** [eq. (3) in Figure 6.20a] is obtained in a clean reaction and isolated as red crystals.

Reduction of the aquo complex **3a** with two equivalents of KC_8 expectedly does not give the anionic complex **4** (as was observed with **3b**) but gives the dihydride complex **1**, which is likely the result of the immediate protonation of **4** by the water released from **3a** upon reduction. The reduction of **3b** (or **1**) to **4** and the protonation of **4** to **1** are quick at room temperature (about 10 seconds). The release of hydrogen from **1** under acidic conditions to give **3a** requires longer reaction times (20 minutes at room temperature) or elevated temperatures (10 minutes at 65 °C).

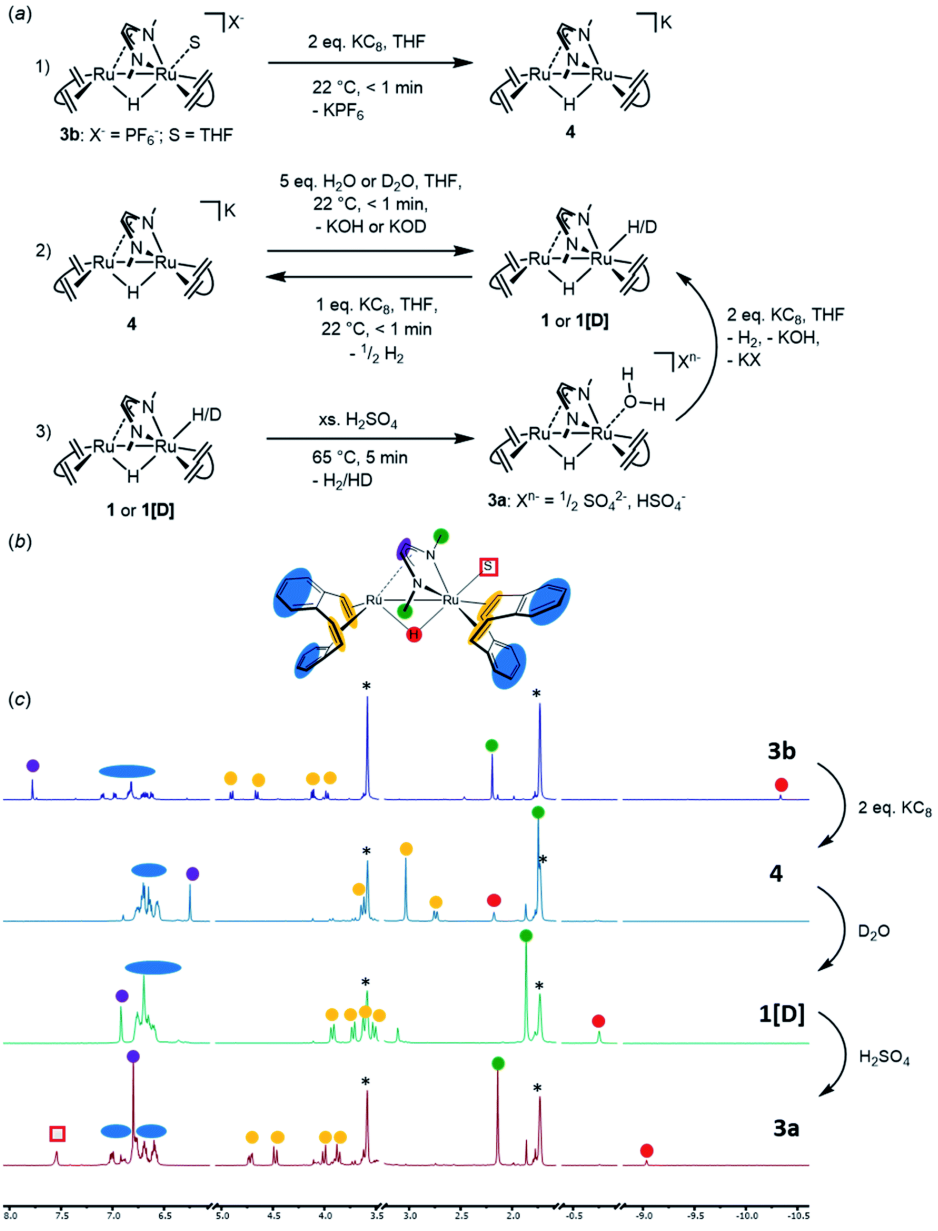

Figure 6.20: (a) Schematic presentation of stoichiometric reactions 1), 2), 3) with the complexes **3b**, **4**, **1** (or **1[D]**), respectively. These were followed by in-situ ^{1}H-NMR spectroscopy in THF[D_8]. (b) Structure of the generic complex [Ru_2(S)(μ–H)(Me_2(dad)($dbcot)_2$] (S = solvent molecule) with color coding for easier allocation of the ^{1}H-NMR signals. (c) Stack plot of ^{1}H NMR spectra taken after every indicated reaction 1) (top); 2) (middle); and 3) (bottom). The colored dots indicate the signals of the corresponding color-coded protons in the formula given in b). The red square marks the signal of the coordinated water in complex **3a**. Note that D_2O was chosen in the 2nd transformation to yield complex **1[D]** with a deuterium in terminal position.

The slowest step in the cycle, namely the conversion of **1** to **3a** under release of hydrogen, was modelled by DFT using the PBE0-D3BJ functional and the def2-SVP/def2-TZVP(Ru) basis set (Figure 6.21). Implicit solvent effects were taken into account by using the cpcm model with water as solvent and a Gaussian charge scheme. In the first step, the oxonium dihydride adduct {[Ru_2H(μ–

H)(Me$_2$dad)(dbcot)$_2$]xH$_3$O$^+$} **1-H$_3$O$^+$** (ΔG=0 kcal mol^{-1}) reacts in an exergonic reaction to the intermediate [{[Ru$_2$H(η_2–H$_2$)(Me$_2$dad)(dbcot)$_2$]xH$_2$O}$^+$ **IxH$_2$xOH$_2$** (ΔG = -6.5 kcal mol^{-1}) which is best described as a hydrated non-classical dihydrogen complex. Hence, this reaction can be seen as an intra-molecular proton transfer reaction from H$_3$O$^+$ to the terminal hydride forming a coordinated polarized H$^{\delta-}$-H$^{\delta+}$ ligand to which the H$_2$O molecule remains loosely bound via a H$_2$O$\cdots$ H$^{\delta+}$-H$^{\delta-}$- hydrogen bridge. The intramolecular displacement of H$_2$ at Ru1 by H$_2$O is an exergonic reaction (**IxH$_2$xOH$_2$** $\rightarrow$ **3a**x**H$_2$**: ΔG = -12.1 kcal mol^{-1}) but requires the surmounting of a sizable activation barrier of $\Delta G^{\#}$ = 21.1 kcal mol^{-1} at which top resides the activated complex **TS1**. According to the calculation, the H$_2$ in **3a**x**H2** forms a Van-der-Waals complex with one of the aromatic rings of the dbcot ligands. Finally, H$_2$ is released exergonically to give **3a** and H$_2$ (**3a**x**H$_2$** $\rightarrow$ **3a** + H$_2$: ΔG = -5.5 kcal mol^{-1}). Note that the reaction between the dihydride complex **1** and neutral H$_2$O to give H$_2$ and the hydroxide complex [Ru(OH)(μ–H)(Me$_2$dad)(dbcot)$_2$] is not only endergonic (ΔG = +11.1 kcal mol^{-1}) but also blocked by a prohibitively high activation barrier of $\Delta G^{\#}$ = 58.9 kcal mol^{-1} (Figure 6.22) explaining that this hydroxide complex is not experimentally observed. Overall, the calculations are in fair agreement with the experiments and show that all transformations can take place at room temperature. But specifically, hydrogen release will be significantly faster at elevated temperatures.

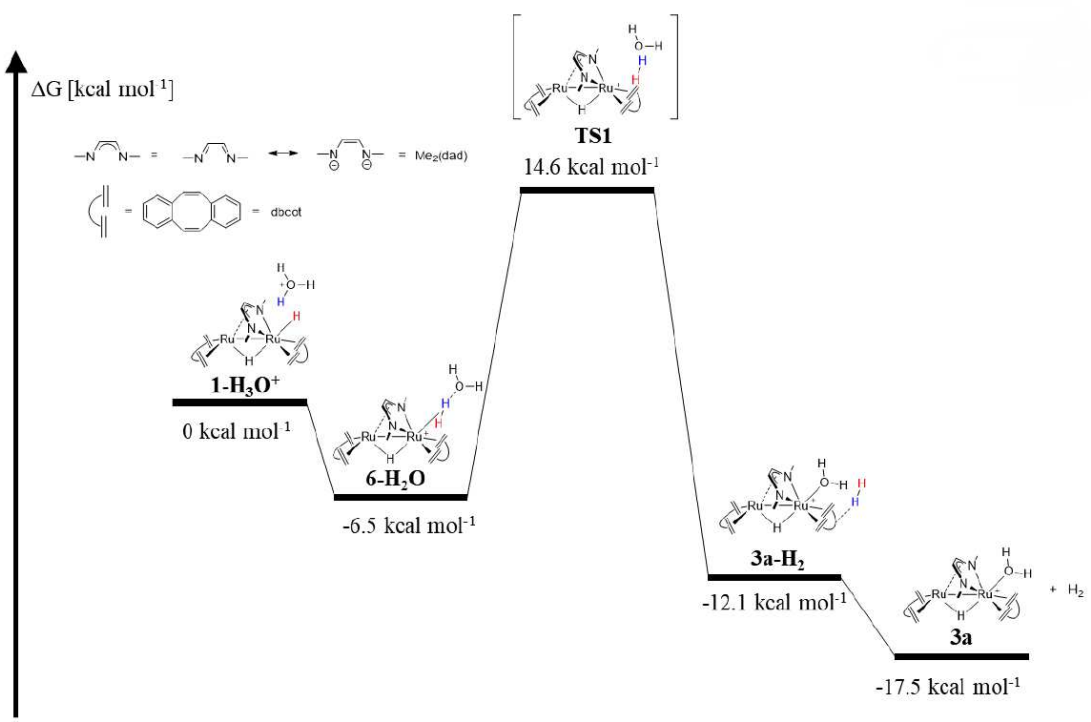

Figure 6.21: Mechanism of hydrogen evolution in acidic solution calculated by DFT (Orca 4.2.0, PBE0-D3BJ/def2-SVP/def2-TZVP(Ru), cpcm water (surfacetype vdw_gaussian)).

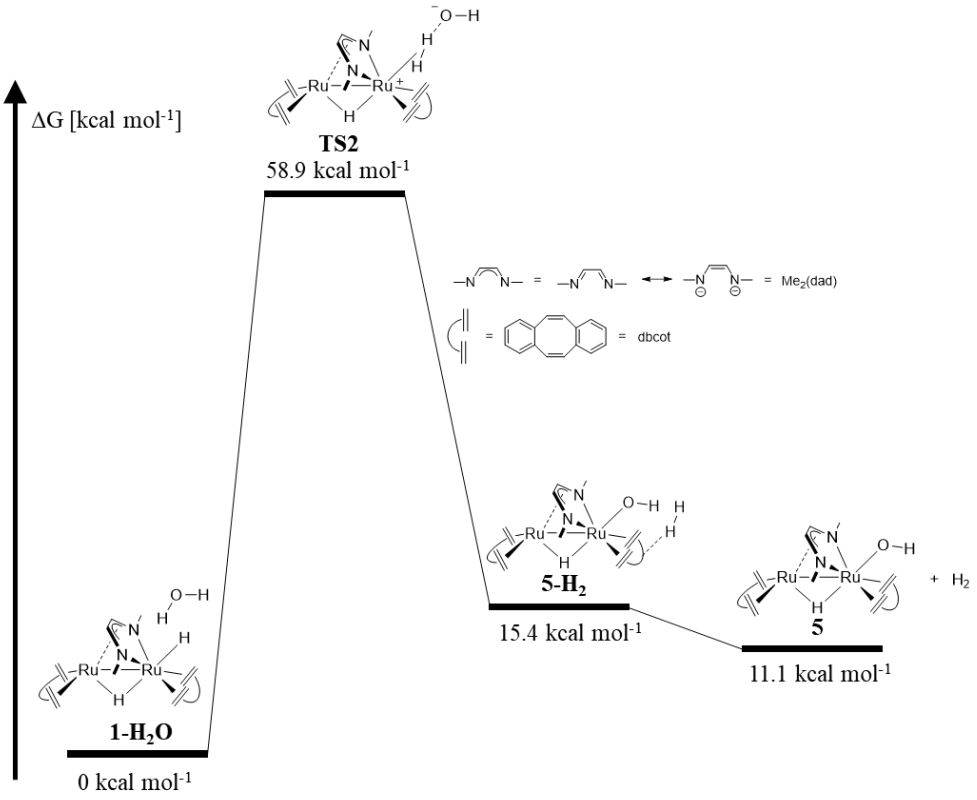

Figure 6.22: Mechanism of hydrogen evolution in neutral solution calculated by DFT (Orca 4.2.0, PBE0-D3BJ/def2-SVP/def2-TZVP(Ru), cpcm water (surfacetype vdw_gaussian)).

The rather efficient production of hydrogen in neutral bulk water with **2_{dil}@C^k** as electrocatalyst can be explained by the fact that the proton exchange membrane causes a locally more acidic environment.[123,124] Generally, the stoichiometric experiments combined with the DFT calculations are in accordance with the higher electrochemical activity of the MEA under acidic conditions. This allows to propose the simplified catalytic cycle shown in Figure 6.23 which shows some of the proposed elementary steps occurring at the electrode surface. By applying a negative potential, the precursor **2@C^k** catalyst is reduced to **4@C^k**, which in presence of a proton source, will be instantly protonated to generate **1@C^k**. In the next step, molecular hydrogen is released very likely through the formation of a non-classical hydrogen complex such as **IxH_2@C^k**. Loss of hydrogen occurs in the next step leading to the cationic hydrido-aquo complex **3a@C^k**. Reduction by two electrons from the cathode due to the applied negative applied potential will reduce **3a@C^k** and give **4@C^k** whereby the catalytic cycle is closed.

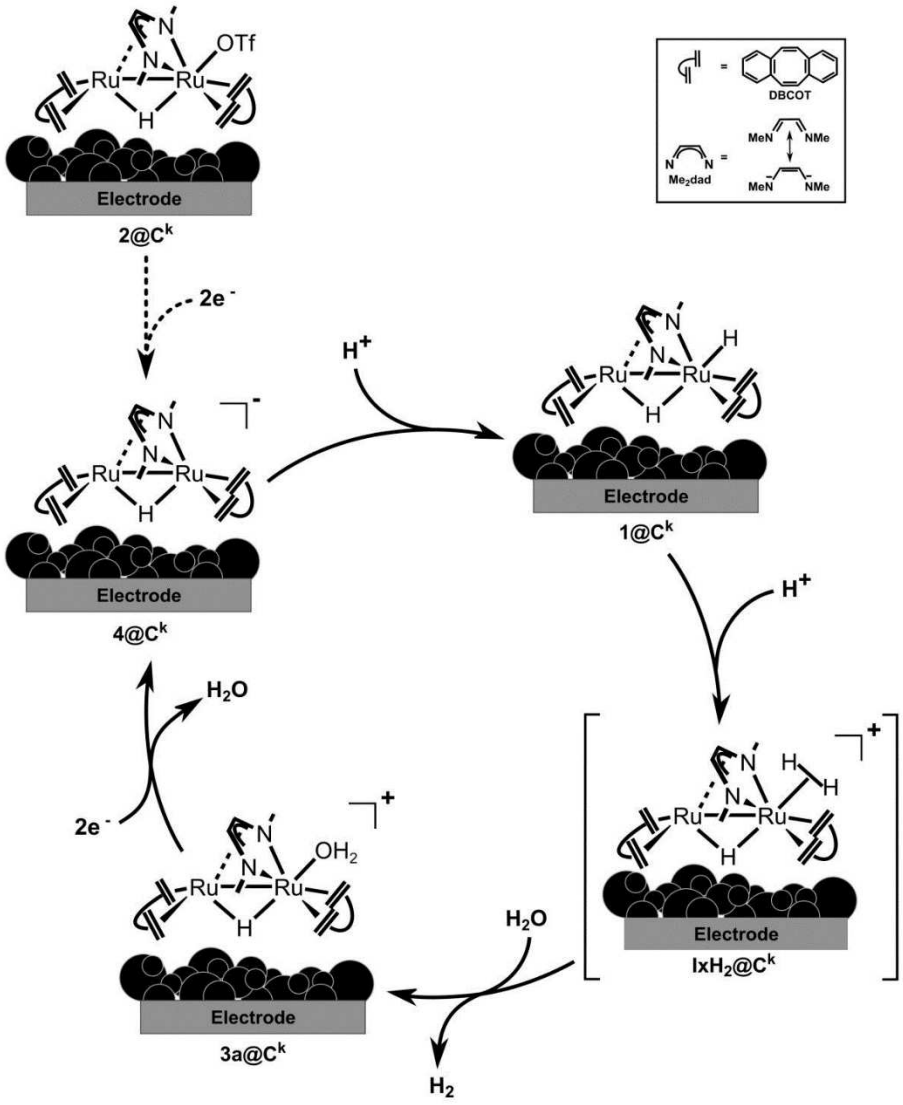

Figure 6.23: Proposed mechanism for hydrogen evolution reaction by water electrolysis occurring onto the **2@C^k** cathode within in the cell.

6.1.4 Conclusion

The dinuclear ruthenium compound, [Ru_2(OTf)(μ–H)(Me_2dad)(dbcot)$_2$] was successfully synthetized, once supported on carbon black (**2@C^k**) it showed a remarkably stability toward hydrogen evolution in a PEM electrolyser.

The development of electrodes made from molecular catalysis, may open the doors to a new class of materials with a low metal loading but very high efficiency because in principle every supported molecule may serve as active center. The stability observed for this device is remarkable high and no decomposition after operation (at 0.2 A cm^{-2}) for one week at 80 °C is observed, a finding that is unprecedented in the literature of

PEM electrolysers with carbon-adsorbed molecular catalysts. A possible explanation for this observation may be that catalytically active species like $[Ru_2(OH_2)(\mu\text{–}H)(Me_2dad)(dbcot)_2]$ **3a** do not contain any sensitive components such as phosphanes, R_3P, as ligands which are prone to chemical transformations (i.e. formation of phosphaneoxides) which lead the catalyst to a rather rapid decomposition and deactivation. Instead, the ligand framework is composed exclusively from rather stable C–C, C–N, and C–H bonds. Approximately 28 L_{H2} min^{-1} g_{Ru}^{-1} of hydrogen were evolved, with a corresponding turnover frequency of 7800 mol_{H2} $mol_{catalyst}^{-1}$ h^{-1}. Model reactions and DFT calculations give some insight about a possible mechanism for hydrogen evolution at the electrode surface and show that likely only classical organometallic reaction steps are involved. This in turn can serve as starting point to design catalysts for devices that possess higher efficiency and ideally only earth-abundant metals as active sites using the repertoire of known organometallic transformations. Further studies will be aimed to understand how the organometallic complexes interact with the interface of the conducting support material. In the electrocatalytic material **2@C^k**, only van-der-Waals interaction exist between the dinuclear Ru complexes and the carbon black (likely H···C^K interaction between the hydrogen centers of benzogroups of the dbcot ligand and conjugated p-systems in C^K); even considering these weak interactions, the performances is still excellent. Further room for improvement is believed to lie in the development of materials in which the molecular catalyst effectively couples in the conduction band of the support material.

6.2 Realization of a scale up system for water splitting with MoO_2 based cathode for HER in alkaline environment

6.2.1 introduction

H_2 produced from electrochemical water splitting powered with renewable energies (green hydrogen) is currently of great interest, driven by increasing demand for renewable energy based on clean resources.[125,126] H_2 produced from water, used for energy storage and as a clean fuel in, for example, auto traction will allow the removal of carbon from the energy equation(s).[125–127] Since the late 1950s, steam methane reforming (SMR) is dominantly used to produce H_2 followed by coal gasification and also water electrolysis (WE), although the latter only contributes 2-4 % of today's global H_2 production.[6,128,129] The cost of production of H_2 via SMR, which is in the range of 2 € per kg H_2, is economically attractive.[128] WEs can accept high current inputs per surface area, operate in dynamic modes and can be ramped up quickly, which are all requirements for storage of intermittent energy sources.[130,131] Realistic estimates of H_2 cost are greater than 3.8 € per kg H_2, making it currently uncompetitive [128]. It has been predicted with the advantages of economies of scale WE will become competitive in the future.[132,133] The components of PEM WEs are costly due to the highly corrosive environment. Due to the oxidative and acidic conditions of the anode, the bipolar plates (BPs) are typically made of costly titanium and dominate the cost making up 51 % of the stack costs, followed by the manufacturing costs of the MEA (10 %) and the cost of the cathode (9 %) and anode (8 %) current collectors. The cost of PEMWE anode catalyst and membrane are comparable at 6 and 5 %, respectively, and the cathode at 1 %. The alkaline environment of anion exchange membrane water electrolysis (AEMWE) widens the window of options in materials choices. For example, regarding the BPs switching to stainless steel,[134] and non PGM electrocatalysts are available with the potential for a large reduction in costs.[135,136] Few systems have reached a commercial scale although laboratory results are quite impressive. For example, the removal of the liquid electrolyte (usually KOH) is a significant challenge. Recently, 1 A cm^{-2} was demonstrated with a pure water feed. However, this activity was achieved with high loadings of Pt and IrO_2 catalysts.[137] And an exceptional 8 A cm^{-2} at 2 V with PGMs and 1 M KOH.[138] One of the key challenges involves developing low-cost and sustainable catalysts for both HER and OER that match the activity of PGM materials and show long-term durability at high current densities. A current density of 1 A cm^{-2}

has been achieved at a cell potential of 1.57 V with a Fe-NiMo-NH_3/NH_2 anode and a NiMo-NH_3/NH_2 cathode aided by 1M KOH and high temperature (80 °C).[139] Regarding the HER in alkaline, Pt is still the most active catalyst, however slower kinetics means high loadings are required.[140] As alternatives, intermetallic compounds of Ni and Mo including Ni_7Mo_7, Ni_3Mo and Ni_4Mo all show enhanced activity. In some cases, like $MoNi_4/MoO_2$@Ni, $MoO_{3-x}/NiMoO_4$ or Ni_4Mo, the activities are similar to Pt/C when tested in 1 M KOH. High HER activity was shown for $MoNi_4/MoO_{3-x}$ nanorod arrays grown on nickel foam and the activity was assigned to $MoNi_4$ alloy nanoparticles that grow on the surface under reductive annealing. [59] In this study, a series of Mo-Ni on Ni foam type (here named MoO_2/Ni) catalysts are prepared, and the synthesis conditions are varied to identify those producing the most active material. A volcano type curve of activity with respect to synthesis temperature exists with 600 °C the best annealing temperature. The structure of the catalyst formed at this temperature is a surface enriched with MoO_2 confirmed by XPS, SEM and HR-TEM. The activity in complete AEMWE is evaluated over 14 days of operation together with a Fe-Ni-Mo anode and a commercial AEM. Changes in the surface structure during operation are evaluated using SEM and XPS, and also metal dissolution was evaluated by SFC-ICP-MS technique. The synthesis was scaled up to prepare electrodes with an active area of 78.5 cm^2 and electrodes were employed in a 3 cell electrolyser stack.

6.2.2 Experimental

6.2.2.1 Half-cell testing

Measurements were performed as discussed in paragraph 4.2.1. Polarization (linear sweep voltammetry LSV) experiments were performed in a 0.1 M KOH solution (pH 13) saturated with hydrogen (30 minutes of pure hydrogen bubbling) at a scan rate of 1 mV s^{-1}. The hydrogen evolution reaction was evaluated by performing the scans between 0 and -0.4 V vs RHE. Electrochemical impedance spectroscopy (EIS) measures were carried out in a 0.1 M KOH solution, under an N_2 atmosphere (30 minutes of pure nitrogen bubbling), with a frequency range spanning from 100 kHz to 0.01 Hz, at a potential of 100 mV. The data and the equivalent circuit were elaborate with “Zwiev4” software.

6.2.2.2 On-line electrochemical dissolution tests

Stability of the MoO_2/Ni cathodes were investigated by on-line scanning flow cell (SFC) ICP-MS technique. This setup consists of a custom-designed and manufactured propylene carbonate scanning flow-cell (SFC)[141]. The outlet of the cell was coupled to the inlet of the ICP-MS (Perkin Elmer NexION 350X). A glassy carbon rod was used as a counter electrode that was connected to the SFC via a T connector on the inlet side. An Ag/AgCl/ 3 M KCl reference electrode (Metrohm) was connected to the cell via a capillary channel on the outlet side. The Ar-purged electrolyte flow was controlled by the peristaltic pump of the ICP-MS (Elemental Scientific, M2 pump) with an average flow-rate of 193 µl min^{-1}. Electrochemical measurements were performed in 0.05 M KOH electrolyte solution saturated with Ar. The potentials are reported against the reversible hydrogen electrode (RHE) using the aforementioned equation (see paragraph 4.2.1)

Electrocatalyst spots were drop-casted on a GC plate (SIGRADUR, A = 25 cm^2), which was used as the working electrode. Firstly, powder catalysts were recovered from nickel foam supported materials by sonicating the Ni lamina into a 2-propanol solution, then it is left to dry. MoO_2/Ni (800 °C) and $MoNiO_4$/Ni samples were not investigated, due to the impossibility of recovering the powders from Ni foam.

Inks were prepared in a vial weighing 12 mg of powder catalyst, then adding 1.2 ml of a solution of H_2O:2-propanol 3:1 (v:v) respectively and adjusting it at pH 12 and adding finally 10 µl of Nafion 5% wt. The catalyst suspension was then drop-casted (0.25 µl) onto the polished glassy carbon plate resulting in spot diameters between 1200–1500 µm. The working electrode was sitting on an XYZ translation stage (Physik Instrumente M-403), allowing rapid navigation in between samples. Electrochemical protocols were performed using a Gamry Reference 600 potentiostat. An in-house developed LabVIEW software controlled all instruments, including the stages, gas control box, force sensor, mass flow controllers and the potentiostat. ICP-MS was calibrated daily by a four-point calibration slope prepared from standard solutions (Ni, Mo – Merck Centripur). ^{58}Co and ^{103}Rh were used as internal standards. The sample and internal standard streams were merged via a Y-connector right before the nebulizer of the ICP-MS.

A protocol consistent in a series of electrochemical measures was employed in order to stress the material. Contact with the SFC was established at -0.2 V vs RHE. The

system was held at this potential for 10 min (Step I), followed by 2 cycles between -0.35 and 0.61 V RHE applying 2 mV s^{-1} scan rate (Step II). The upper potential limit for Step II was calculated considering the average values of open circuit potential (OCP) of the MoO_2/Ni series. Finally, the system was left for 5 minutes at OCP conditions in Step III.

6.2.2.3 AEM water electrolysis cell testing

Membrane electrode assemblies (MEA): 5 cm^2 cathode electrodes MoO_2/Ni, (400, 500, 600, 700 or 800 °C) and a 5 cm^2 Ni foam anode, were assembled together with a FAA-3-PK-130 membrane (Fumatech) using appropriate gaskets and graphite plates and a stainless steel Scribner testing cell (Scribner Corp. USA). A 4 Nm torque closing force was used. The same procedure was used for the electrolyser combining the cathode MoO_2/Ni (600 °C) and the anode Fe-Ni-Mo/Ni_{foam}. In all cases, the AEM was pre-activated by feeding the cells with KOH 1 M for 12 hours at 60 °C before each experiment.

Arbin Instrument) was used to control the electrolysis cell (Paragraph 6.1.2.2); a peristaltic pump (Gilson Mini Pulse) was used to feed the electrolyser with an aqueous solution of KOH (1 M) at the anode with a 1 ml min^{-1} flow rate, while no solution was fed to the cathode. The cathode compartment was connected to a Bronkhorst ELFlow flow meter in order to quantify the H_2 produced by the cell. Scan voltage curves were acquired between 0 and 2 V at a 10 mV s^{-1} scan rate. Galvanostatic experiments were performed by applying a constant current load of 0.5 A cm^{-2} to the cell and monitoring the cell voltage. The internal ohmic resistance was estimated using an external potentiometer, connected to the heads of the cell.

6.2.2.4 Zero-Gap Laboratory-Scale Anion Exchange Membrane Alkaline Water Electrolysis Stack

Ni foam and MoO_2/Ni electrodes of geometric area 78.5 cm^2 (circular shape, 10 cm diameter) were tested as cathodes in an alkaline water electrolysis cell (Figure 6.24).

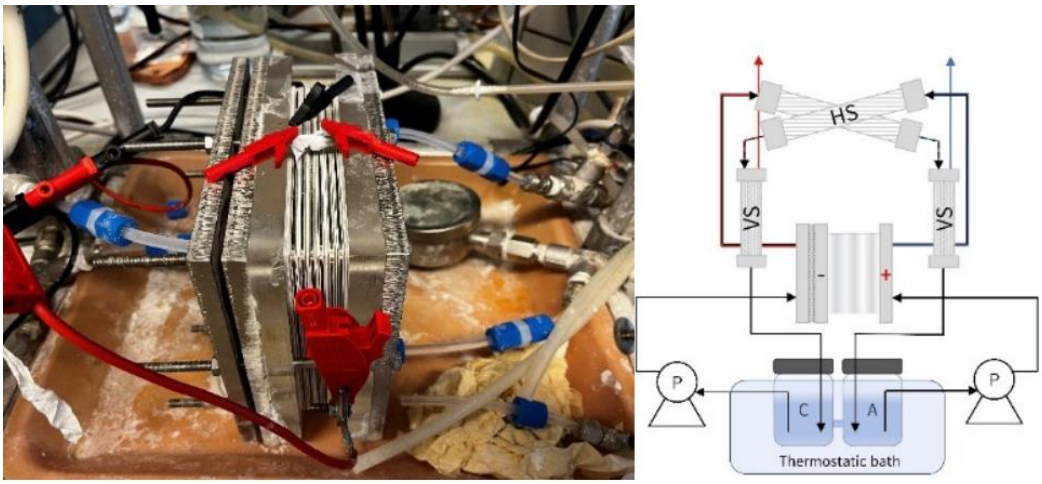

Figure 6.24: Zero-Gap Laboratory-Scale Anion Exchange Membrane Alkaline Water Electrolysis 3 cell Stack. Electrode active surface area 78.5 cm^2.

Bare Ni foam without any pretreatment was used as anode in all tests. A chlorinated block copolymer of styrene ethylenebutylene-styrene (PSEBS-CM) with 1,4-Diazabicyclo 2.2.2 octane (DABCO) functional groups was used as membrane/separator of the electrode compartments [142]. The thickness of the separator was 180 µm and 270 µm in the dry and wet states, respectively. As liquid electrolyte, 1 M KOH was used. Reservoirs of the liquid electrolyte were heated in a water bath to keep the temperature on the outlet of the cell at 25 or 40 °C, respectively. The flow rate of the liquid electrolyte was 1 cm^3 min^{-1} cm^{-2}. Before the experiments, the cell was equilibrated in several steps at current 0.8, 1.6, 3.2, 4.8 and 6.4 A for 10 minutes each. The short-term electrochemical characterization was done by means of the load curve measurement using potentiostat/galvanostat Metrohm with 20 A booster in the range of 0 –19 A with a continuous current increase of 7.6 mA s^{-1}. Stability measurement was done for 55 hours in 1 M at 25 °C. The constant current density of 0.2 A cm^{-2} was applied while the cell voltage was recorded.

Electrochemical impedance spectroscopy of the single cell of geometric area 78.5 cm^2 was measured in the frequency range 25 kHz – 0.01 Hz at maximal amplitude of perturbing signal 30 mV at cell voltages range 1.5 – 1.8 V with step of 0.05 V. The equivalent electrical circuit used for the evaluation of the measured spectra is shown in Figure 6.25.

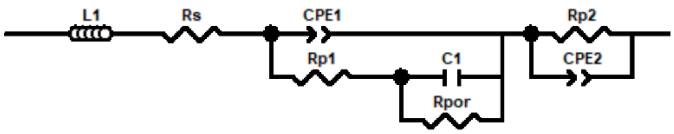

Figure 6.25: Equivalent circuit used for evaluation of the electrochemical impedance spectra of 78.5 cm^2 single cell. L – inductance, Rs – high frequency resistance, CPE1 – capacitance of the double layer of the first reaction, Rp1 – polarisation resistance of the first reaction, C1 – capacitance of the pore walls, Rpor – resistance of the pores filled with solution, CPE2 – capacitance of the double layer of the second reaction, Rp2 – polarisation resistance of the second reaction.

It was considered circuit C1, Rpor, to simulate capacitance of the pores walls and resistance of the pores filled by liquid electrolyte respectively [143,144]. Rp1, CPE1, Rp2 and CPE2 elements were then considered to be related to the electrochemical reactions. The short-stack in a bipolar configuration consisting of 3 cells was tested under the same conditions using the same equipment as for the single cell characterization [145]. EIS characterization of the short-stack was modified, due to the presence of the more cells connected in series. Each bipolar electrode was contacted by silver wires 0.3 mm thick, which allowed to measure the characteristic of each particular cell in the short-stack. In this case, working and counter electrodes were connected to terminal electrodes (which act as anode and cathode respectively), meanwhile sensing electrodes were connected to the silver wires contacting the electrodes of the particular cell. EIS was measured under the conditions of the alkaline water electrolysis in galvanostatic mode at current densities of 0.01, 0.05 and 0.1 A cm^{-2}.

The maximal amplitude was ± 5 % of the current range. The frequency range used was 40 kHz to 0.01 Hz. As EIS spectra of the short-stack showed only one time constant related to electrochemical reaction, they were evaluated based on the simplified equivalent electrical circuit, which consists of only L1, Rs, CPE1, Rp1, C1 and Rpor elements.

6.2.3 Result and discussion

6.2.3.1 Electrochemical activity for the HER

The electrocatalytic HER activity of $MoNiO_4$/Ni and the MoO_2/Ni (400, 600, 800 °C) cathodes was examined by Linear Sweep Voltammetry (LSV) in 0.1 M KOH and compared to a Pt/C reference material (Figure 6.26 a).

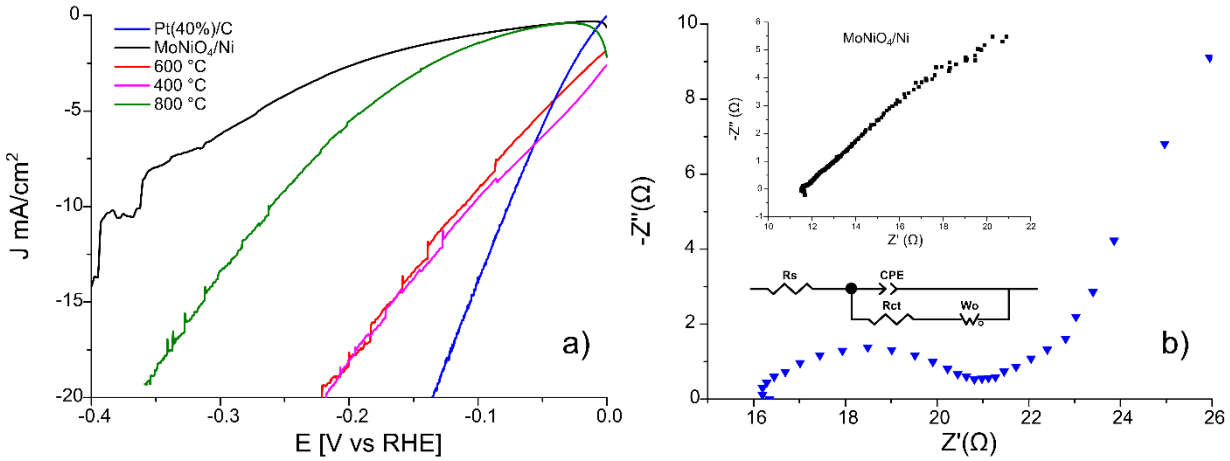

Figure 6.26: (a) LSV of $MoNiO_4$/Ni and MoO_2/Ni cathodes treated at 400, 600, 800 °C, and Pt(40%)/C as a reference. Scan from 0 to – 0.4 V vs RHE in H_2 sat 1mV/s (Pt(40%)/C at 5 mV/s), KOH 0.1 M. (b) EIS of MoO_2/Ni (600) with the equivalent circuit at -0.1 V vs RHE. Inset show the trend for $MoNiO_4$/Ni.

The precursor $MoNiO_4$/Ni produces a HER current density of -2.65 mA cm^{-2} at -200 mV (RHE) compared to -17.63 mA cm^{-2} for MoO_2/Ni (600 °C) and (-6.15 mA cm^{-2}) for MoO_2/Ni (800 °C). The change in the surface structure during reductive annealing at 600 °C that forms an enriched MoO_2 surface leads to improved activity. The sample prepared at 800 °C is less active for the HER due to a loss in overall surface area. Electrochemical Impedance Spectroscopy (ESI) (Figure 6.26 b) was used to study $MoNiO_4$/Ni and MoO_2/Ni (600 °C). The results gave a value of 4.58 Ω for charge transfer resistance (Rct) at -0.1 V vs RHE for the sample prepared at 600 °C and the intercept with the x axis at high frequency provides a solution resistance Rs of 16.16 Ω. The equivalent circuit was also extrapolated and then fitted with the experimental curve (Figure 6.27): from there the value of CPE and Walburg element were obtained (Table 6-4).

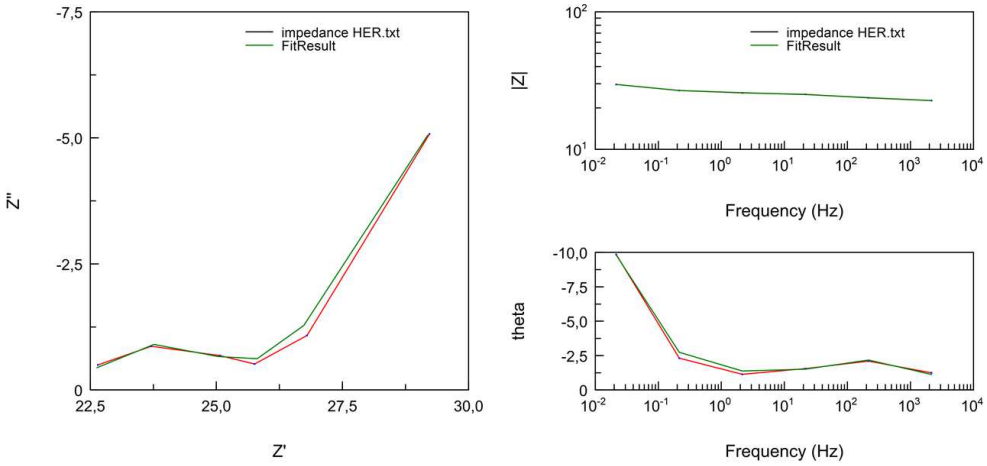

Figure 6.27: Nyquist plot and bode diagram for MoO_2/Ni (600 °C) (red line), and fitting curve for the equivalent circuit (green line), at -0.1 V vs RHE.

Table 6-4: EIS equivalent circuit's elements values.

Element	Value	Error	Error %
Rs	16.16	0.059	0.37
CPE-T	0.00073453	0.00015	20.88
CPE-P	0.68044	0.025	3.72
Rct	4.586	0.013	2.90
Wo-R	7.234	0.90	12.51
Wo-T	10.17	1.62	15.96
Wo-P	0.43101	0.027	6.35

The improved conductivity of the 600-sample can be attributed to the formation of a surface MoO_2 layer.[146] Reductive annealing of the $NiMoO_4$ nanorods on nickel foam at temperatures from 400 to 800 °C under a 5% H_2 in N_2 gas mixture results in a transformation of Mo(6+) to Mo(4+) and the segregation of a surface layer of MoO_2. The presence of Ni is confirmed by elemental analysis, however, no evidence of surface Ni_4Mo alloy formation (XPS) and no distinct Ni_4Mo surface alloy particles are observed (HR-TEM). By contrast, the surface is enriched with Mo rather than Ni. Ni XPS shows only Ni oxide hydroxide species present with no evidence of Ni(0). Other research groups using analogous synthesis conditions report the formation of individual Ni_4Mo alloy particles on the surface of MoO_2 rods and attribute increased HER activity to these sites.[147,148] The results reported here attribute activity enhancement to the formation of a MoO_2 enriched surface. It has been reported by

other groups that Ni foam supported MoO_2 nanoflowers prepared using reductive annealing at 400 °C in H_2 exhibits enhanced HER activity.[149] MoO_2 possesses high electrical conductivity because it has a distorted rutile structure [150] and its bonding involves delocalization of some of the Mo electrons in the conduction band and the nanorod-like structure has a high surface area, so there are correspondingly many active sites exposed for the HER. [151] The Ni contact with MoO_2 upraises the O 2p orbital in MoO_2, thus strengthening the hydrogen adsorption for enhanced HER kinetics.[152] Notably, Ni has been shown to play no direct role as a catalytic site but to effectively disperse and activate the oxidized catalytic Mo species.[153] Nickel acts as the adsorption site for hydrogen, while MoO_2 promotes the dissociation of water molecules and optimizes the Ni–H bond energy.[154]

6.2.3.2 Electrochemical stability characterization

By SFC-ICP-MS technique the electrochemical dissolution of Mo-Ni materials [141] were investigate. Regarding nickel, the signal was always below the detection limit (1 ppt), demonstrating that only molybdenum electrochemically dissolves under these conditions. In Step I a potential of -0.2 V vs RHE was applied in order to evaluate the dissolution during hydrogen evolution, it is worth to notice that as shown in Figure 6.28. A major contribution to the dissolution of Mo occurs for all samples initially upon contact with the electrolyte solution (known as contact peak).

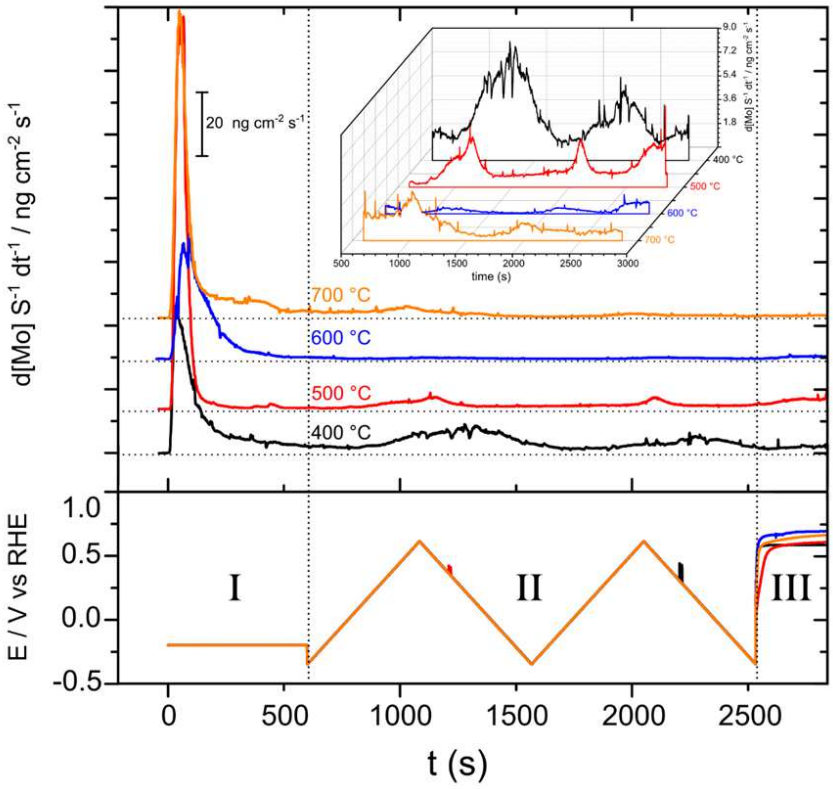

Figure 6.28: Dissolution profiles obtained by the SFC-ICP-MS technique for each sample. Top: dissolution rate as a function of time; bottom: applied potential as a function of time during the electrochemical protocol. Insert shows in detail the region from 500 s to 2900 s.

During Step II, two consecutive CVs were recorded during wide potential window in order to determine the onset of dissolution and the amount of dissolved species. From here are clearly visible two major feature related to Mo dissolution, the onset of dissolution differs for each sample (measured during the first CV) (Table 6-5). It is interesting that the highest onset belongs to the MoO_2/Ni (600 °C) sample which shows the best performance for HER and also the lowest dissolved amounts among the series (Figure 6.29). Lastly, in Step III, the working electrode is held at OCP so any Mo dissolution under these conditions arises due to corrosion occurring at the OCP (which as can be seen is at anodic potentials above 0.5 V). As reported previously, the dissolution of Mo has been shown to occur from surface Ni-Mo alloys under HER relevant conditions. Activity decrease at a positive potential due to the dissolution of Mo oxides is a cause of performance loss. This will present stability issues, especially during the intermittent operation of industrial electrolysers (the cathode potential changes in the anodic direction immediately after the electrolyser is disconnected from the power source). The results reported here show that the MoO_2 surface that forms at 600 °C during synthesis is less prone to Mo electrochemical dissolution, even though

the ratio Mo/Ni in the surface increase during annealing step (see paragraph 3.4.1). These results suggest that strategies may be developed to avoid such dissolution phenomenon by appropriate tuning of the surface speciation.

Table 6-5: Total dissolution and dissolution without contact peak, with relative E_{onset} recorded in the first CV for the MoO_2/Ni series.

	Total dissolution (ng cm^{-2})	**Dissolution (no contact peak) (ng cm^{-2})**	**E_{onset} 1° CV (V vs RHE)**
Catalyst	Mo		
400 °C	13386	7168	0.088
500 °C	10781	3618	-0.031
600 °C	6076	704	0.242
700 °C	10582	2911	0.185

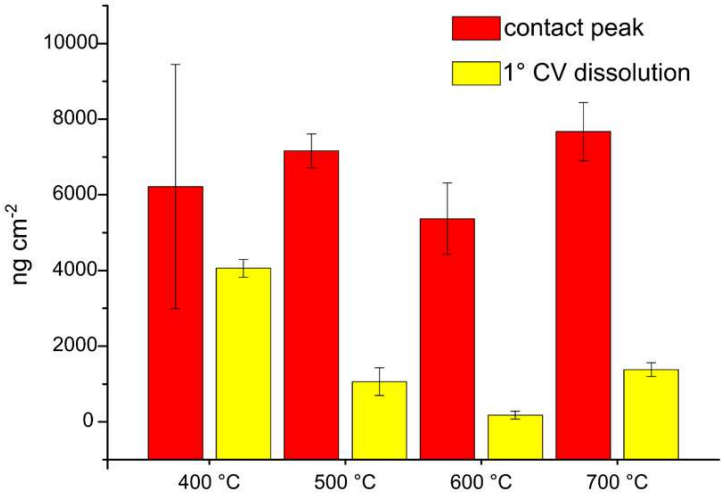

Figure 6.29: Dissolved amounts calculated by integrating the dissolution profiles of MoO_2/Ni cathodes, with error bars.

6.2.3.3 AEM water electrolysis cell testing

The 5 cm^2 MoO_2/Ni cathodes were incorporated with a commercial AEM (Fumatech FAA-3-PK-130) and a 5 cm^2 nickel foam as OER anode electrode in a water electrolysis test cell. The cell was fed with 1 M KOH on the anode side, while the cathode compartment was connected to a flow meter to monitor the H_2 produced. The

electrolysis cells were evaluated by running polarization curves from 0 to 2 V at 10 mV s^{-1}. The cell temperature was controlled at 60 °C. Higher performance may be obtained at a cell temperature of 80 °C but anion exchange membranes have limited long-term stability. Hence, it is unrealistic to run AEM-WE at temperatures above 60 °C.

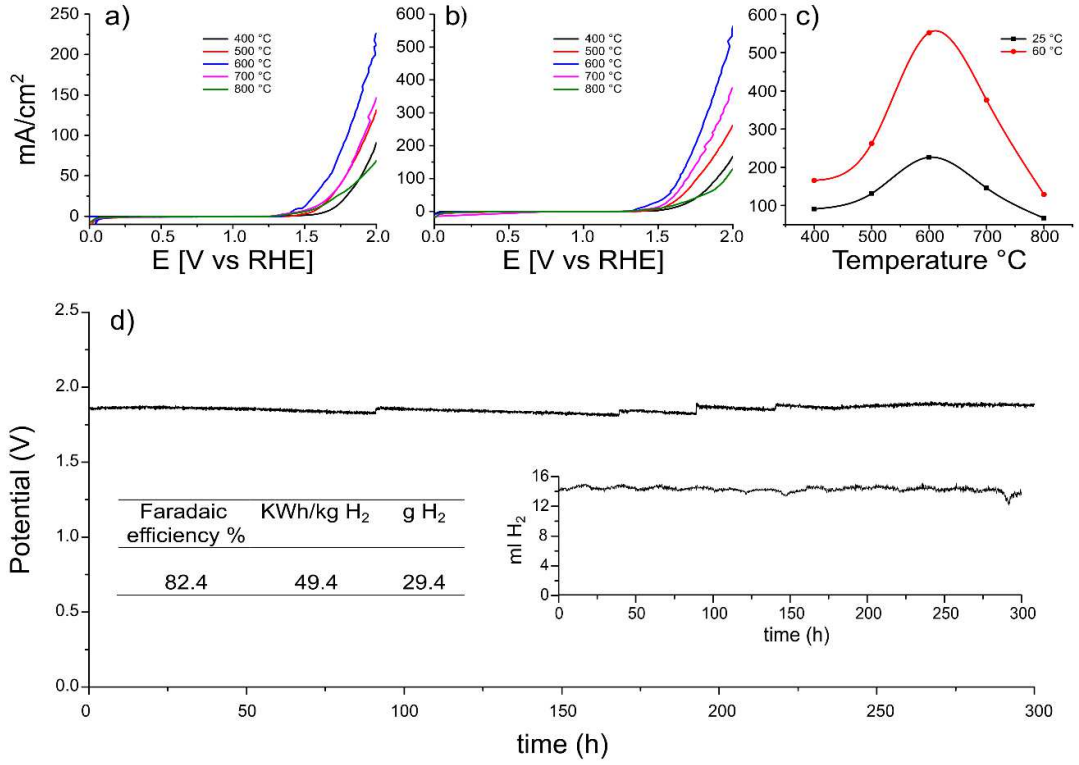

Figure 6.30: Scan voltage carried out at (a) 25 and (b) 60 °C, and the extrapolated volcano plot (c). (d) Cell voltage and H_2 production monitored at 0.5 A cm^{-2}, 60 °C, 1M KOH to anode.

The polarization curves obtained at 25 and 60 °C are shown in Figure 6.30 a-b. At both temperatures, the cathode prepared at 600 °C exhibits the highest current density reaching 0.55 A cm^{-2} at 2 V, that can be correlated to the formation of the segregated MoO_2 on the nano-rod surfaces as described in detail in the 3.4.1 section. A volcano type plot is observed when the current density recorded at 2 V is plotted against annealing temperature (Figure 6.30 c). The practical use in an industrial AEM electrolyser will require stability over many thousands of hours. To this end, we have tested the best performing cathode MoO_2/Ni (600 °C) with a Fe-Ni-Mo/Ni anode and FAA-3-PK-130 membrane in the electrolyser fed with 1 M KOH at 60 °C for two weeks. The cell was set at a constant current density of 0.5 A cm^{-2} and the cell voltage and hydrogen production were monitored over the period of the test (Figure 6.30 d). During the test, the cell voltage remained stable at around 1.85 V, with a faradaic efficiency of

82.4% (H_2 losses occur through tubing connections and gaskets) and cell voltage-based energy cost of 49.4 KWh kg^{-1} H_2.

Analysis of the cathode and anode electrodes recovered from the electrolysis cell after the two weeks test was undertaken. Cathode SEM images taken after the test, suggest a small amount of increased roughness of the rod surface as shown in Figure 6.31 (e= pre-catalysis, f= post-catalysis). Regarding the anode, SEM images show a drastic change in the structure (Figure 6.31: g= pre catalysis, h= post-catalysis), the surfaces of rods have a more “flake-structure” as a result of prolonged oxygen evolution at the anode surface. XPS analysis of the electrodes post catalysis show in the Mo and Ni spectra no significant change in the speciation of the cathode electrode (Figure 6.31 a-b, Figure 6.32 a-b). Regarding the anode, no signal for Mo is observed after the two weeks test (Figure 6.31 c-d), and the spectra of iron did not show significant difference (Figure 6.33). The surface structure contains Ni and Fe as Mo has leached out during oxygen evolution. The activity for the OER has not suffered by this change suggesting that the active sites are the Ni-Fe interface and as long as the surface area is retained, the anode activity is maintained despite the loss of surface Mo.

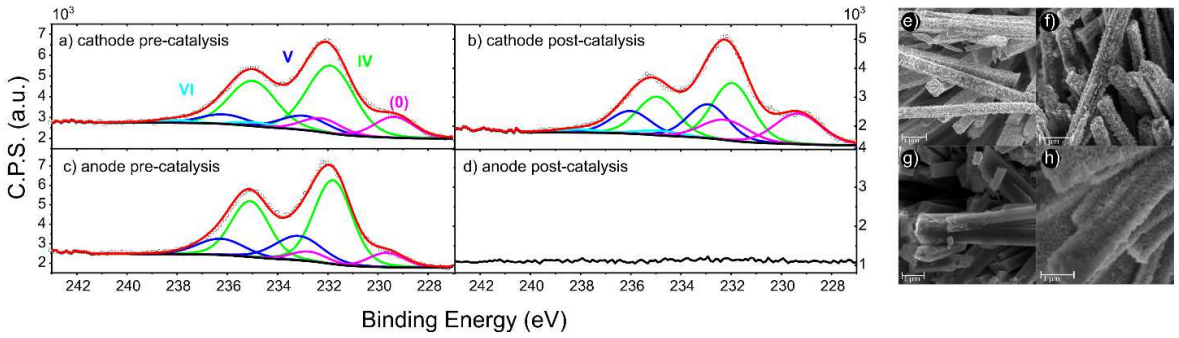

Figure 6.31: Mo XPS spectra of the MoO_2/Ni (600 °C) cathode (a) pre-catalysis, (b) post-catalysis; and Fe- Ni-Mo/Ni anode c) pre-catalysis, d) post-catalysis. SEM images of MoO_2/Ni (600 °C) (e) pre-catalysis (f) post-catalysis; and Fe-Ni-Mo/Ni g) pre-catalysis, h) post-catalysis.

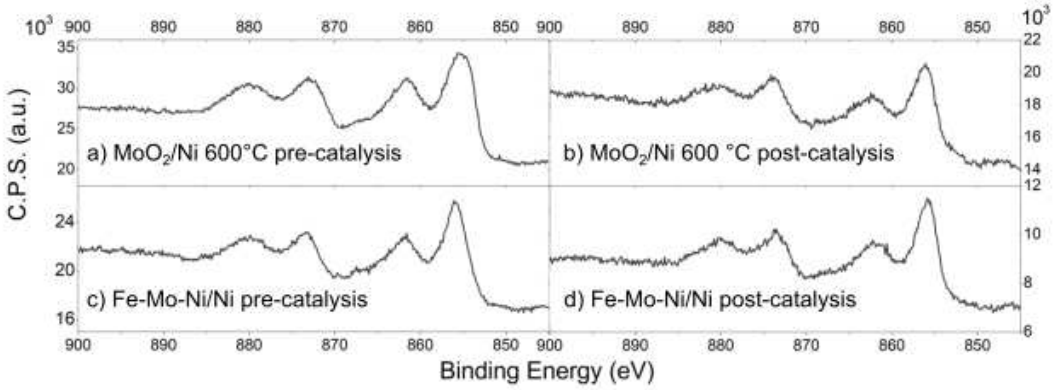

Figure 6.32: Ni 2p XPS of cathode MoO2-Ni/Ni and anode Fe-Ni-Mo/Ni, before and after 2 weeks operation.

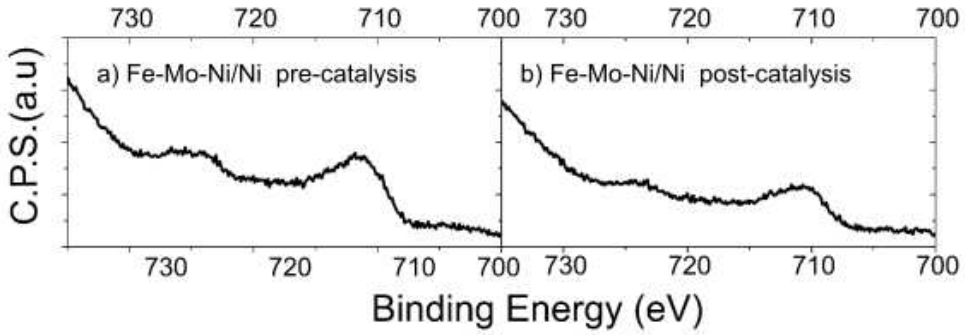

Figure 6.33: Fe 2p XPS of anode Fe-Ni-Mo/Ni before and after 2 weeks operation.

6.2.3.4 Zero-Gap Laboratory-Scale Anion Exchange Membrane Alkaline Water Electrolysis Stack

The synthetic procedure was used to prepare larger MoO_2/Ni electrodes as circular 10 cm diameter disks (geometrical area 78.5 cm^2) for incorporation in a 3 cell AEM electrolyser short stack. Firstly, a single 78.5 cm^2 electrode was tested. A comparison of the load curves measured with bare Ni foam and MoO_2/Ni cathodes is shown in Figure 6.34. The MoO_2/Ni cathode exhibits greatly enhanced performance compared to bare nickel foam. At 25 °C a current density of 230 mA cm^{-2} was achieved at cell voltages 2.28 and 2.0 V for bare and MoO_2/Ni respectively. At 40 °C performance improved for both cells. In the case of the Ni foam cathode, the cell voltage decreases approximately by 0.11 V (4.8 %), while the cell voltage with MoO_2/Ni drops by 0.14 V (7.0 %). At 40 °C MoO_2/Ni operates at a cell voltage of 0.31 V (14.3 %) lower than bare

Ni foam. This confirms the general trend of the improved performance with higher temperature and high activity of the Ni-Mo modified Ni foam for hydrogen evolution reaction. A stability test at constant current density 0.2 A cm^{-2} (25 °C) using MoO_2/Ni showed stable performance as the cell voltage increase evaluated by linear regression of the measured points was 7.4 μV $hour^{-1}$. The average value of the cell voltage was (1.948 ± 0.003) V, *i.e.* average cell voltage fluctuates by only 0.15 % during the test.

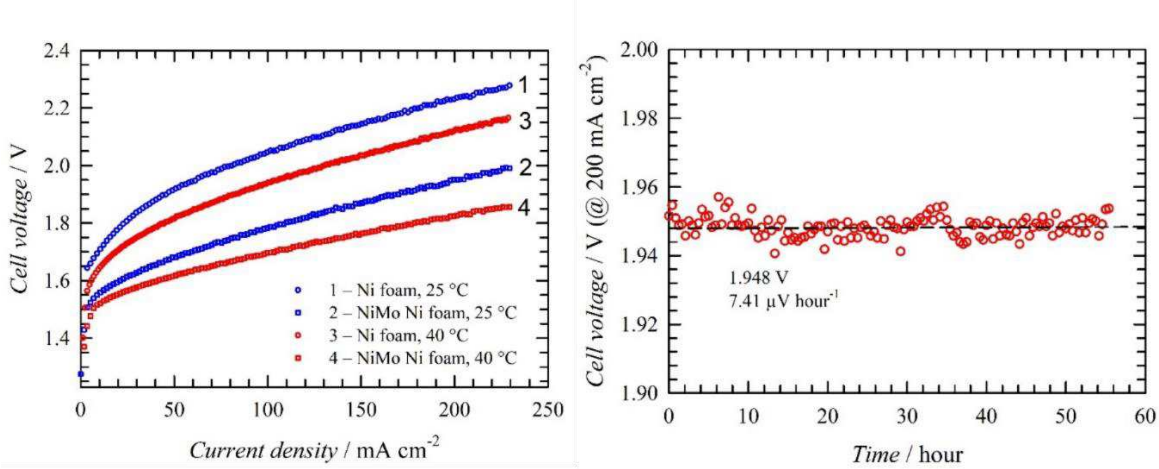

Figure 6.34: Load curves of the alkaline water electrolysis using different cathodes (blue) Nickel foam and (red) MoO_2/Ni). Ni foam anode, geometrical area 78.5 cm^2, 1 M KOH, liquid electrolyte flow rate 1 cm^3 min^{-1} cm^{-2}, at 25 °C (1 and 3) and 40 °C (2 and 4), PSEBS-CM-DABCO membrane. Stability test using MoO_2/Ni (600 °C) modified Ni foam cathode. Ni foam anode, geometrical area 78.5 cm^2, 1 M KOH, liquid electrolyte flow rate 1 cm^3 min^{-1} cm^{-2}, temperature indicated in the figure inset, PSEBS-CM-DABCO membrane, current density 200 mA cm^{-2}, temperature 25 °C.

EIS was used to characterize the single cell performance in order to gain deeper insight into the behaviour of the MoO_2/Ni (600 °C) electrode. The data obtained by EIS are summarised in Figure 6.35.

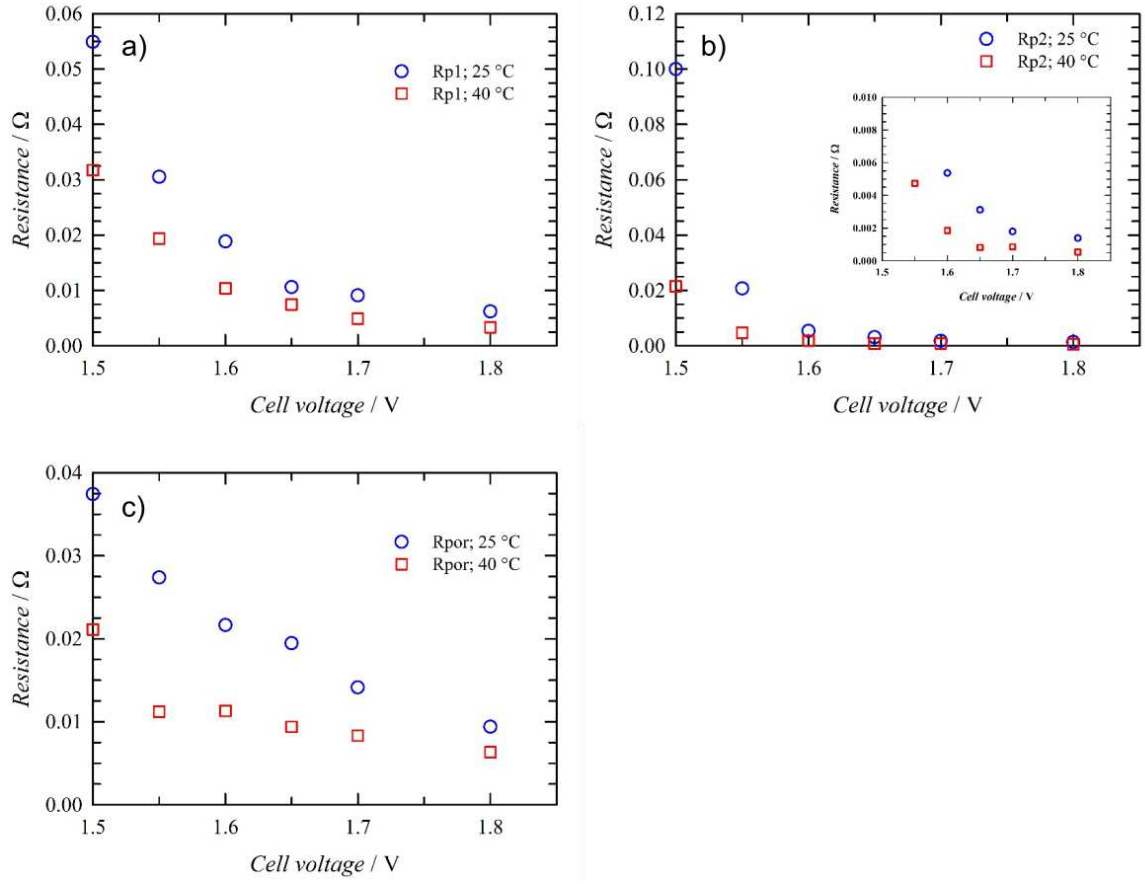

Figure 6.35: Dependence of the Rp1, Rp2 and Rpor on cell voltage evaluated from EIS data by the equivalent circuit method, cell operating temperature 25 and 40 °C. Ni Foam anode, MoO_2/Ni cathode, 78,5 cm^2 electrodes geometrical area, frequency range 25 kHz – 0,01 Hz and maximal amplitude of perturbing signal of 30 mV were used.

Based on the results shown in Figure 6.35 and due to the experimental setup used, all Rp values can be addressed to the defined phenomena. Rp1 and Rp2 values show exponential dependence on the cell voltage, identifying them as the polarization resistances of the electrochemical reactions. As the oxygen evolution reaction was in this particular case not catalyzed and because nature of the oxygen evolution reactions (more complex process with 4 electrons exchanged), higher polarization resistance (Rp1) may be assigned to the anodic reaction. Correspondingly, polarization resistance Rp2 can be assigned to the cathodic hydrogen evolution reaction. Rpor value then corresponds to the resistance of the liquid electrolyte in the pores of the Ni foam electrodes. This assignment is in agreement with the dependence of the Rpor values on the cell voltage showing linear character. In the next step, the short-stack consisting of 3 cells was assembled. The performance of the shortstack in the form of polarization curves is shown in Figure 6.36.

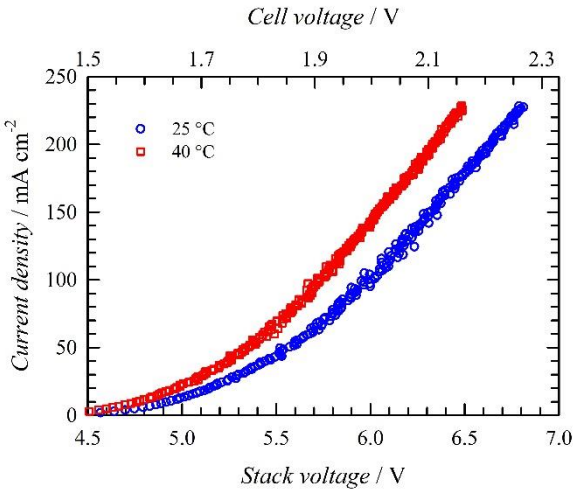

Figure 6.36: Load curves of the short-stack. Cathode: MoO_2/Ni ; Anode: Ni foam; geometrical area: 78.5 cm^2; 1 M KOH solution; flow rate: 1 cm^{-3} cm^{-2} min^{-1}; separator: PSEBS-CM-DABCO (180 µm in dry state) anion-selective polymer membrane.

Load curves recorded for the short stack indicate lower performance when compared to the single cell experiment, see Figure 6.36, which derive from stack architecture and mass transport phenomenon. In order to understand this observation, EIS of the short stack was recorded. The information obtained for the selected current densities is for average value of the cell in the shortstack summarized in Figure 6.37. Ohmic resistance per a single cell at open circuit conditions in the short stack increased from 0.011 and 0.009 Ω observed for the single cell experiment, to 0.020 and 0.016 Ω for 25 and 40 °C respectively. This observation is also confirmed by the load curve shape showing at higher current loads clear linear dependence. The reason for this consists of a more complex arrangement of the stack leading to more significant ohmic losses. In order to obtain more information on the ohmic resistance, EIS was used to determine Rs value.

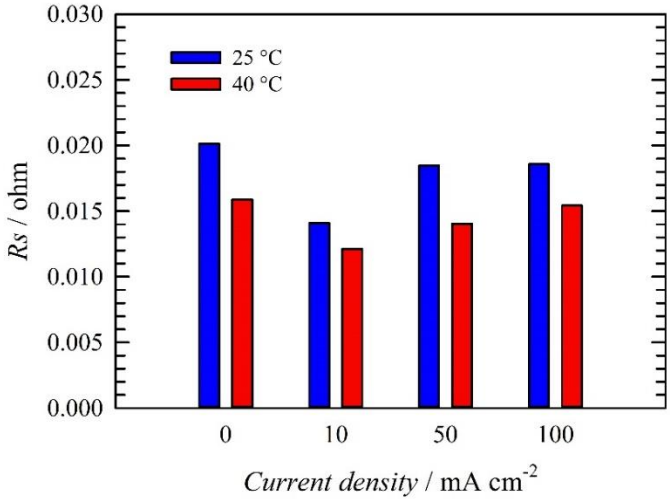

Figure 6.37: Values of the one average cell in short-stack resistance (Rs) evaluated by EIS on 3 cell shortstack under current load. Cathode: MoO_2/Ni; Anode: Ni foam; geometrical area: 78.5 cm^2; 1 M KOH solution; flow rate: 1 cm^{-3} cm^{-2} min^{-1}; separator: PSEBS-CM-DABCO (180 µm in dry state) anion-selective polymer membrane. Frequency range 40 kHz – 0.01 Hz; current amplitude ± 5 % of the current range.

From Figure 6.37, it is possible to see that Rs value increases with the current density for both temperatures. This indicates accumulation of the gaseous phase in the short-stack, which increases the ohmic resistance of the electrolyte by filling the electrodes' porous structure. At the same time, values of Rs are lower for temperature 40 °C, which is given by the higher ionic conductivity of both, liquid and polymer electrolytes. Interestingly, Rs values decreased initially under the current load. This might be due to the presence of additional transport phenomena, which are present under current load (electroosmotic flux). Rs values obtained for 50 and 100 mA cm^{-2} show the same values at the temperature of 25 °C, but a slight increase at 40 °C.

6.2.4 Conclusion

In this study, it was firstly investigated the surface nanostructure activity relationship for the alkaline hydrogen evolution reaction of MoO_2/Ni electrodes prepared by hydrothermal and reductive annealing treatment. A volcano plot of HER activity with respect to annealing temperature is obtained with the best activity shown after annealing at 600 °C. XPS, SEM and HR-TEM analyses indicate the increase in activity is associated with an enriched MoO_2 surface of the nano-rod arrays. At higher temperatures, the surface area is reduced, and HER activity is lost. The results also suggest that the Ni_4Mo alloy is not involved in the enhanced HER activity as reported

previously as this species was not found on the surface of the rods. On-line electrochemical dissolution studies have pointed out how MoO_2/Ni obtained at 600 °C exhibits improved stability compared to the other materials, due to the formation of more stable MoO_2 phases on the surface.

In the second phase of this investigation circular MoO_2/Ni cathode electrodes of 78.5 cm^2 area were prepared and incorporated in a 3 cell AEM electrolyser stack with an anion exchange membrane and Ni foam anodes. This study demonstrates that MoO_2/Ni cathodes with optimized surface structure can be readily prepared with large geometric surface areas and be employed in multi-cell AEM electrolysers. This study hence opens the door to the future application of these electrodes on an industrial scale.

7 Concluding remarks

This thesis work concerned the synthesis and the characterisation of several kinds of materials as electrocatalysts in either fuel cells or electrolyser. Transition metal nanoparticles deposited on two different supports, namely M/C and M-CeO_2/C, have been prepared and their activity towards hydrogen evolution reaction (HER) and hydrogen oxidation reaction (HOR) in alkaline media has been verified. Their activity was compared with Pd-CeO_2/C, which is prepared at the ICCOM-CNR laboratories and represents the reference anode for alkaline fuel cells. Thanks to its optimal Ru-H bond strength (65 Kcal mol^{-1}), the high roughness factor (19 mF cm^{-2}) and the high electrochemically active surface area, Ru based materials show best activity for both the reactions HOR and HER, with the exchange current (i_0) that has an average value of 106 A g_{Metal}^{-1}. From this point of view, the addition of ceria did not show any major improvements for Ru materials, only Pd, Ir and Rh are improved by the presence of cerium oxide.

Fuel cell tests have been conducted using Pd-CeO_2/C as reference anode for the HOR and for the first time, the performance of the device have been investigated using a series of different cathodes for the oxygen reduction reaction, Pd/C, Ag-Co/C Fe/C, and Pt/C. Amongst them, Fe/C is of particular interest due to its high performance, reaching a power density of 1 W cm^{-2} at 60°C.

Hydrogen evolution from water electrolysis represents the main topic of this thesis: initially a “molecular” approach is reported here, using an organometallic compound based on dinuclear Ru diazadiene olefin complex, $[Ru_2(OTf)(\mu\text{-}H)(Me_2dad)(dbcot)_2]$, supported onto carbon black (**2@C^k**). This catalyst showed good performance and stability towards HER in an acidic environment (400 mA cm^{-2}, 1.9 V), and also a remarkable turn over frequency (TOF) of 7800 mol_{H2} $mol_{catalyst}^{-1}$ h^{-1}, which is maintained over 7 days of operation. Compared to nanoparticle-based materials, it is clear that **2@C^k** is much more effective in terms of mass activity, due essentially to the fact that here each molecule represents a catalytic centre, while in the case of Ru/C for example, only the surface of the metal particles is involved in the reaction. Even though the general performance is high for a molecular compound, it is still low if compared to a material like MoO_2/Ni. It is also worth to notice that the preparation and synthesis of **2@C^k** requires a complicated multi-step synthesis and use of organic solvents.

A viable alternative to Ru complexes but also to expensive electrodes already in use in industrial electrolysers, is represented by Mo-Ni nano-rod arrays on nickel foam, namely MoO_2/Ni. Tests in an AEMWE with a Ni foam anode demonstrate a current density of 0.55 A cm^{-2} (2 V) at 60 °C and H_2 production was stable for more than 300 h (0.5 A cm^{-2}). These materials do not require precious metals, and as shown in the previous chapter the feasibility to realize a scaled-up version of these electrodes make them very attractive for industrial applications. There remain still some questions about the durability of the MEA for prolonged periods of operation due to the leakage of metals from the electrodes and the membrane stability, therefore further studies are required to address these issues, but the result obtained here are very promising.

In summary, this thesis has demonstrated how nano-engineered catalysts can play a major role in the energy transition: reducing the amount of noble metals or even the complete substitution with cheap materials is the main achievement of this work. The ultimate goal is to reduce the manufacturing costs of these electrochemical devices and make such technologies economically competitive.

8 Other instruments

X-ray powder diffraction (XRD): X-ray diffraction (XRD) scans were acquired at room temperature with a PANalytical X'PERT PRO diffractometer, employing CuKα radiation (λ= 1.54187 Å) and a PW3088/60-graded multilayer parabolic X-ray mirror for Cu radiation. The diffractograms were acquired in the 2θ range from 22.0 to 88, using a continuous scan mode with an acquisition step size of 2θ= 0.02638 and a counting time of 49.5 s. QualX2 software and the COD database were used to qualitatively assign the peaks to the structures.

Transmission electron microscopy (TEM:) analysis was carried out using a Philips CM12 microscope at an accelerating voltage of 100 kV.

(HR)-TEM: selected area electron diffraction (SAED) and STEM measurements were performed by a ZEISS LIBRA200FE instrument equipped with an Oxford (X-stream 2) EDX probe. SAED indexing was performed by CrystBox software.

SEM and EDX: samples characterization was performed using a TESCAN Gaia 3 FIB/SEM. The microscope hosts a 30 kV Triglav electron column, and a Cobra Focused Gallium Ion Beam column. SEM images of the sample surfaces were acquired using the two in-beam Secondary Electron (SE) and Back Scattered Electron (BSE) detectors. EDX maps on the cross-sections were acquired by using the instrument EDAX HI-OCTANE detector.

X-ray photo-electron spectroscopic (XPS) analyses were performed in an UHV chamber with a base pressure lower than 10-9 mbar. the chamber was equipped with non-monochromatized Al radiation (hυ = 1486.6 eV) and a hemispherical electron/ion energy analyzer (VSW mounting a 16-channel detector). The operating power of the X-ray source was 1440 W (12 kV and 12 mA) and photoelectrons were collected normal to the sample surface, maintaining the analyzer angle between analyzer axis and X-ray source fixed at 54.5°. All the samples were adsorbed on Aluminium foil and XPS spectra acquired in a fixed analyzer trans-mission mode with pass energy of 44.0 eV. The spectra were analyzed by using the CasaXPS software. Linear or Shirley functions have been used to subtract the background.

Brunauer–Emmett–Teller (BET): specific surface area of catalysts was determined by nitrogen adsorption at 77 K using a Micromeritics ASAP 2020 analyzer. The

samples were pre-treated at 30 μmHg at 393 K for 15 h. The BET surface area was calculated in the pressure range between 0.1 and 0.22p/p0 while the pore volume was calculated with the Barrett-Joiner-Halenda (BJH) method.

9 List of publications

- Integration of a Pd-CeO_2/C anode with Pt and Pt-free cathode catalysts in high power density anion exchange membrane fuel cells, H. A. Miller, M. v. Pagliaro, M. Bellini, F. Bartoli, L. Wang, I. Salam, J. R. Varcoe and F. Vizza, *ACS Appl Energy Mater*, 2020, **3**, 10209–10214

- Reshaping the Cathodic Catalyst Layer for Anion Exchange Membrane Fuel Cells: From Heterogeneous Catalysis to Homogeneous Catalysis, R. Ren, X. Wang, H. Chen, H. A. Miller, I. Salam, J. R. Varcoe, L. Wu, Y. Chen, H.-G. Liao, E. Liu, F. Bartoli, F. Vizza, Q. Jia and Q. He, *Angewandte Chemie International Edition*, 2020, anie.202012547.

- Remarkable stability of a molecular ruthenium complex in PEM water electrolysis, M. Bellini, J. Bösken, M. Wörle, D. Thöny, J. J. Gamboa-Carballo, F. Krumeich, F. Bàrtoli, H. A. Miller, L. Poggini, W. Oberhauser, A. Lavacchi, H. Grützmacher and F. Vizza, *Chem Sci*, 2022, **13**, 3748–3760.

- Improving Alkaline Hydrogen Oxidation Activity of Palladium through Interactions with Transition-Metal Oxides, M. v. Pagliaro, C. Wen, B. Sa, B. Liu, M. Bellini, F. Bartoli, S. Sahoo, R. K. Singh, S. P. Alpay, H. A. Miller and D. R. Dekel, *ACS Catal*, 2022, **12**, 10894–10904

- Probing the effect of metal-CeO_2 interactions in carbon supported electrocatalysts on alkaline hydrogen oxidation and evolution reactions, M. v. Pagliaro, M. Bellini, F. Bartoli, J. Filippi, A. Marchionni, C. Castello, W. Oberhauser, L. Poggini, B. Cortigiani, L. Capozzoli, A. Lavacchi, H. A. Miller and F. Vizza, *Inorganica Chim Acta*, 2022, **543**, 121161.

- Probing the activity and stability of MoO_2 surface nanorod arrays for hydrogen evolution in an anion exchange membrane multi-cell water electrolysis stack, F.Bartoli, M. Marelli, C. Evangelisti, L. Capozzoli, K. Bouzek, J. Hnát, G. Serrano, L. Poggini, K. Stojanovski, V. Briega-Martos, S.Cherevko, H. A. Miller, F. Vizza.
  Submitted to: Journal of Materials Chemistry A

10 References

(1) Murphy, D. J.; Hall, C. A. S. Energy Return on Investment, Peak Oil, and the End of Economic Growth. *Ann N Y Acad Sci* **2011**, *1219* (1), 52–72. https://doi.org/10.1111/j.1749-6632.2010.05940.x.

(2) EPA EPA420-F-0, 3. 2005. Agency, U. S. E. P. & United States Environmental Protection Agency. Metrics for Expressing Greenhouse Gas Emissions: Carbon Equivalents and Carbon Dioxide Equivalents.

(3) Stephenson, M. The Carbon Cycle, Fossil Fuels and Climate Change. In *Energy and Climate Change*; Elsevier, 2018; pp 1–26. https://doi.org/10.1016/B978-0-12-812021-7.00001-4.

(4) Everett, B.; Boyle, G.; Peake, S. *Energy Systems and Sustainability: Power for a Sustainable Future*, 2nd edition.; OUP Oxford, Ed.; 2011.

(5) Zini, G.; Tartarini, P. *Solar Hydrogen Energy Systems*; Springer Milan: Milano, 2012. https://doi.org/10.1007/978-88-470-1998-0.

(6) Nikolaidis, P.; Poullikkas, A. A Comparative Overview of Hydrogen Production Processes. *Renewable and Sustainable Energy Reviews* **2017**, *67*, 597–611. https://doi.org/10.1016/j.rser.2016.09.044.

(7) iea.org/reports/hydrogen. Https://Www.Iea.Org/Reports/Hydrogen.

(8) Rifkin, J. The Hydrogen Economy: The Creation of the Worldwide Energy Web and the Redistribution of Power on Earth. *Refocus* **2003**, *4* (3), 12. https://doi.org/10.1016/S1471-0846(03)80112-9.

(9) Shriver and Atkins. *Inorganic Chemistry*, 5th Edition.; Oxford University Press, Ed.; New York, 2010.

(10) Lavacchi, A.; Miller, H.; Vizza, F. *Nanotechnology in Electrocatalysis for Energy*; Springer New York: New York, NY, 2013; Vol. 170. https://doi.org/10.1007/978-1-4899-8059-5.

(11) Zhang, J.; Chen, G.; Müllen, K.; Feng, X. Carbon-Rich Nanomaterials: Fascinating Hydrogen and Oxygen Electrocatalysts. *Advanced Materials* **2018**, *30* (40), 1–22. https://doi.org/10.1002/adma.201800528.

(12) Murthy, A. P.; Theerthagiri, J.; Madhavan, J. Insights on Tafel Constant in the Analysis of Hydrogen Evolution Reaction. *Journal of Physical Chemistry C* **2018**, *122* (42), 23943–23949. https://doi.org/10.1021/acs.jpcc.8b07763.

(13) Nandikes, G.; Gouse Peera, S.; Singh, L. Perovskite-Based Nanocomposite Electrocatalysts: An Alternative to Platinum ORR Catalyst in Microbial Fuel Cell Cathodes. *Energies (Basel)* **2021**, *15* (1), 272. https://doi.org/10.3390/en15010272.

(14) Li, Y.; Li, Q.; Wang, H.; Zhang, L.; Wilkinson, D. P.; Zhang, J. Recent Progresses in Oxygen Reduction Reaction Electrocatalysts for Electrochemical Energy Applications. *Electrochemical Energy Reviews* **2019**, *2* (4), 518–538. https://doi.org/10.1007/s41918-019-00052-4.

(15) Jiang, Y.; Ni, P.; Chen, C.; Lu, Y.; Yang, P.; Kong, B.; Fisher, A.; Wang, X. Selective Electrochemical H 2 O 2 Production through Two-Electron Oxygen Electrochemistry. *Adv Energy Mater* **2018**, *8* (31), 17–19. https://doi.org/10.1002/aenm.201801909.

(16) Smolinka, T.; Ojong, E. T.; Garche, J. Hydrogen Production from Renewable Energies-Electrolyser Technologies. *Electrochemical Energy Storage for Renewable Sources and Grid Balancing* **2014**, 103–128. https://doi.org/10.1016/B978-0-444-62616-5.00008-5.

(17) Vincent, I.; Bessarabov, D. Low Cost Hydrogen Production by Anion Exchange Membrane Electrolysis: A Review. *Renewable and Sustainable Energy Reviews* **2018**, *81* (June 2017), 1690–1704. https://doi.org/10.1016/j.rser.2017.05.258.

(18) Cho, M. K.; Park, H. Y.; Lee, H. J.; Kim, H. J.; Lim, A.; Henkensmeier, D.; Yoo, S. J.; Kim, J. Y.; Lee, S. Y.; Park, H. S.; Jang, J. H. Alkaline Anion Exchange Membrane Water Electrolysis: Effects of Electrolyte Feed Method and Electrode Binder Content. *J Power Sources* **2018**, *382* (February), 22–29. https://doi.org/10.1016/j.jpowsour.2018.02.025.

(19) Breeze, P. *Power Generation Technologies*; 2005. https://doi.org/10.1016/B978-0-7506-6313-7.X5000-1.

(20) Wang, L.; Lavacchi, A.; Bevilacqua, M.; Bellini, M.; Fornasiero, P.; Filippi, J.; Innocenti, M.; Marchionni, A.; Miller, H. A.; Vizza, F. Energy Efficiency of Alkaline Direct Ethanol Fuel Cells Employing Nanostructured Palladium Electrocatalysts. *ChemCatChem* **2015**, *7* (14), 2214–2221. https://doi.org/10.1002/cctc.201500189.

(21) Wang, L. Q.; Bellini, M.; Filippi, J.; Folliero, M.; Lavacchi, A.; Innocenti, M.; Marchionni, A.; Miller, H. A.; Vizza, F. Energy Efficiency of Platinum-Free Alkaline Direct Formate Fuel Cells. *Appl Energy* **2016**, *175*, 479–487. https://doi.org/10.1016/j.apenergy.2016.02.129.

(22) Kirubakaran, A.; Jain, S.; Nema, R. K. A Review on Fuel Cell Technologies and Power Electronic Interface. *Renewable and Sustainable Energy Reviews* **2009**, *13* (9), 2430–2440. https://doi.org/10.1016/j.rser.2009.04.004.

(23) Wang, Y.-J.; Qiao, J.; Baker, R.; Zhang, J. Alkaline Polymer Electrolyte Membranes for Fuel Cell Applications. *Chem Soc Rev* **2013**, *42* (13), 5768. https://doi.org/10.1039/c3cs60053j.

(24) Merle, G.; Wessling, M.; Nijmeijer, K. Anion Exchange Membranes for Alkaline Fuel Cells: A Review. *J Memb Sci* **2011**, *377* (1–2), 1–35. https://doi.org/10.1016/j.memsci.2011.04.043.

(25) Dekel, D. R. Review of Cell Performance in Anion Exchange Membrane Fuel Cells. *J Power Sources* **2018**, *375*, 158–169. https://doi.org/10.1016/j.jpowsour.2017.07.117.

(26) Alesker, M.; Page, M.; Shviro, M.; Paska, Y.; Gershinsky, G.; Dekel, D. R.; Zitoun, D. Palladium/Nickel Bifunctional Electrocatalyst for Hydrogen Oxidation Reaction in Alkaline Membrane Fuel Cell. *J Power Sources* **2016**, *304*, 332–339. https://doi.org/10.1016/j.jpowsour.2015.11.026.

(27) Miller, H. A.; Vizza, F.; Marelli, M.; Zadick, A.; Dubau, L.; Chatenet, M.; Geiger, S.; Cherevko, S.; Doan, H.; Pavlicek, R. K.; Mukerjee, S.; Dekel, D. R. Highly Active Nanostructured Palladium-Ceria Electrocatalysts for the Hydrogen Oxidation Reaction in Alkaline Medium. *Nano Energy* **2017**, *33*, 293–305. https://doi.org/10.1016/j.nanoen.2017.01.051.

(28) Faraj, M.; Boccia, M.; Miller, H.; Martini, F.; Borsacchi, S.; Geppi, M.; Pucci, A. New LDPE Based Anion-Exchange Membranes for Alkaline Solid Polymeric Electrolyte Water Electrolysis. *Int J*

Hydrogen Energy **2012**, *37* (20), 14992–15002. https://doi.org/10.1016/j.ijhydene.2012.08.012.

(29) Wang, L.; Peng, X.; Mustain, W. E.; Varcoe, J. R. Radiation-Grafted Anion-Exchange Membranes: The Switch from Low- to High-Density Polyethylene Leads to Remarkably Enhanced Fuel Cell Performance. *Energy Environ Sci* **2019**. https://doi.org/10.1039/c9ee00331b.

(30) Antolini, E. Carbon Supports for Low-Temperature Fuel Cell Catalysts. *Appl Catal B* **2009**, *88* (1–2), 1–24. https://doi.org/10.1016/j.apcatb.2008.09.030.

(31) Bellini, M.; Pagliaro, M. v.; Lenarda, A.; Fornasiero, P.; Marelli, M.; Evangelisti, C.; Innocenti, M.; Jia, Q.; Mukerjee, S.; Jankovic, J.; Wang, L.; Varcoe, J. R.; Krishnamurthy, C. B.; Grinberg, I.; Davydova, E.; Dekel, D. R.; Miller, H. A.; Vizza, F. Palladium–Ceria Catalysts with Enhanced Alkaline Hydrogen Oxidation Activity for Anion Exchange Membrane Fuel Cells. *ACS Appl Energy Mater* **2019**, *2* (7), 4999–5008. https://doi.org/10.1021/acsaem.9b00657.

(32) Miller, H. A.; Bevilacqua, M.; Filippi, J.; Lavacchi, A.; Marchionni, A.; Marelli, M.; Moneti, S.; Oberhauser, W.; Vesselli, E.; Innocenti, M.; Vizza, F. Nanostructured Fe–Ag Electrocatalysts for the Oxygen Reduction Reaction in Alkaline Media. *J Mater Chem A Mater* **2013**, *1* (42), 13337. https://doi.org/10.1039/c3ta12757e.

(33) Guo, J.; Zhou, J.; Chu, D.; Chen, R. Tuning the Electrochemical Interface of Ag/C Electrodes in Alkaline Media with Metallophthalocyanine Molecules. *The Journal of Physical Chemistry C* **2013**, *117* (8), 4006–4017. https://doi.org/10.1021/jp310655y.

(34) Evangelisti, C.; Schiavi, E.; Aronica, L. A.; Caporusso, A. M.; Vitulli, G.; Bertinetti, L.; Martra, G.; Balerna, A.; Mobilio, S. Bimetallic Gold–Palladium Vapour Derived Catalysts: The Role of Structural Features on Their Catalytic Activity. *J Catal* **2012**, *286*, 224–236. https://doi.org/10.1016/j.jcat.2011.11.007.

(35) Bellini, M.; Folliero, M. G.; Evangelisti, C.; He, Q.; Hu, Y.; Pagliaro, M. v.; Oberhauser, W.; Marchionni, A.; Filippi, J.; Miller, H. A.; Vizza, F. A Gold–Palladium Nanoparticle Alloy Catalyst for CO Production from CO_2 Electroreduction. *Energy Technology* **2019**, *7* (4), 1800859. https://doi.org/10.1002/ente.201800859.

(36) Lenarda, A.; Bellini, M.; Marchionni, A.; Miller, H. A.; Montini, T.; Melchionna, M.; Vizza, F.; Prato, M.; Fornasiero, P. Nanostructured Carbon Supported Pd-Ceria as Anode Catalysts for Anion Exchange Membrane Fuel Cells Fed with Polyalcohols. *Inorganica Chim Acta* **2018**, *470*, 213–220. https://doi.org/10.1016/j.ica.2017.05.020.

(37) Bambagioni, V.; Bianchini, C.; Chen, Y.; Filippi, J.; Fornasiero, P.; Innocenti, M.; Lavacchi, A.; Marchionni, A.; Oberhauser, W.; Vizza, F. Energy Efficiency Enhancement of Ethanol Electrooxidation on Pd–CeO_2/C in Passive and Active Polymer Electrolyte-Membrane Fuel Cells. *ChemSusChem* **2012**, *5* (7), 1266–1273. https://doi.org/10.1002/cssc.201100738.

(38) Miller, H. A.; Lavacchi, A.; Vizza, F.; Marelli, M.; Di Benedetto, F.; D'Acapito, F.; Paska, Y.; Page, M.; Dekel, D. R. A Pd/C-CeO_2 Anode Catalyst for High-Performance Platinum-Free Anion Exchange Membrane Fuel Cells. *Angewandte Chemie International Edition* **2016**, *55* (20), 6004–6007. https://doi.org/10.1002/anie.201600647.

(39) Bellini, M.; Pagliaro, M. v.; Lenarda, A.; Fornasiero, P.; Marelli, M.; Evangelisti, C.; Innocenti, M.; Jia, Q.; Mukerjee, S.; Jankovic, J.; Wang, L.; Varcoe, J. R.; Krishnamurthy, C. B.; Grinberg, I.;

Davydova, E.; Dekel, D. R.; Miller, H. A.; Vizza, F. Palladium–Ceria Catalysts with Enhanced Alkaline Hydrogen Oxidation Activity for Anion Exchange Membrane Fuel Cells. *ACS Appl Energy Mater* **2019**, *2* (7), 4999–5008. https://doi.org/10.1021/acsaem.9b00657.

(40) Lazzarini, A.; Piovano, A.; Pellegrini, R.; Agostini, G.; Rudić, S.; Lamberti, C.; Groppo, E. Graphitization of Activated Carbons: A Molecular-Level Investigation by INS, DRIFT, XRD and Raman Techniques. *Phys Procedia* **2016**, *85*, 20–26. https://doi.org/10.1016/j.phpro.2016.11.076.

(41) Gao, T.; Yang, J.; Nishijima, M.; Miller, H. A.; Vizza, F.; Gu, H.; Chen, H.; Hu, Y.; Jiang, Z.; Wang, L.; Shuai, L.; Qiu, M.; Lei, C.; Zhang, A.; Hou, Y.; He, Q. Evidence of the Strong Metal Support Interaction in a Palladium-Ceria Hybrid Electrocatalyst for Enhancement of the Hydrogen Evolution Reaction. *J Electrochem Soc* **2018**, *165* (14), F1147–F1153. https://doi.org/10.1149/2.0351814jes.

(42) Li, Y.; Abbott, J.; Sun, Y.; Sun, J.; Du, Y.; Han, X.; Wu, G.; Xu, P. Ru Nanoassembly Catalysts for Hydrogen Evolution and Oxidation Reactions in Electrolytes at Various PH Values. *Appl Catal B* **2019**, *258*, 117952. https://doi.org/10.1016/j.apcatb.2019.117952.

(43) Pagliaro, M. V.; Bellini, M.; Bevilacqua, M.; Filippi, J.; Folliero, M. G.; Marchionni, A.; Miller, H. A.; Oberhauser, W.; Caporali, S.; Innocenti, M.; Vizza, F. Carbon Supported Rh Nanoparticles for the Production of Hydrogen and Chemicals by the Electroreforming of Biomass-Derived Alcohols. *RSC Adv* **2017**, *7* (23), 13971–13978. https://doi.org/10.1039/C7RA00044H.

(44) Eguiluz, K. I. B.; Malpass, G. R. P.; Pupo, M. M. S.; Salazar-Banda, G. R.; Avaca, L. A. Synthesis, Characterization, and Electrocatalytic Activity toward Methanol Oxidation of Carbon-Supported Pt $_x$−(RuO $_2$ −M) $_{1-x}$ Composite Ternary Catalysts (M = CeO $_2$, MoO $_3$, or PbO $_x$). *Energy & Fuels* **2010**, *24* (7), 4012–4024. https://doi.org/10.1021/ef100424m.

(45) Thanawala, S.; Georgiev, D. G.; Baird, R. J.; Auner, G. Characterization of Iridium Oxide Thin Films Deposited by Pulsed-Direct-Current Reactive Sputtering. *Thin Solid Films* **2007**, *515* (18), 7059–7065. https://doi.org/10.1016/j.tsf.2007.02.090.

(46) Chung, W.-H.; Tsai, D.-S.; Fan, L.-J.; Yang, Y.-W.; Huang, Y.-S. Surface Oxides of Ir(111) Prepared by Gas-Phase Oxygen Atoms. *Surf Sci* **2012**, *606* (23–24), 1965–1971. https://doi.org/10.1016/j.susc.2012.08.020.

(47) Nguyen, T.-S.; Postole, G.; Loridant, S.; Bosselet, F.; Burel, L.; Aouine, M.; Massin, L.; Gélin, P.; Morfin, F.; Piccolo, L. Ultrastable Iridium–Ceria Nanopowders Synthesized in One Step by Solution Combustion for Catalytic Hydrogen Production. *J. Mater. Chem. A* **2014**, *2* (46), 19822–19832. https://doi.org/10.1039/C4TA04820B.

(48) Wang, C.; Ciganda, R.; Yate, L.; Moya, S.; Salmon, L.; Ruiz, J.; Astruc, D. RhAg/RGO Nanocatalyst: Ligand-Controlled Synthesis and Superior Catalytic Performances for the Reduction of 4-Nitrophenol. *J Mater Sci* **2017**, *52* (16), 9465–9476. https://doi.org/10.1007/s10853-017-1158-7.

(49) Seo, J.; Gowda, A.; Babu, S. v. Almost Complete Removal of Ceria Particles Down to 10 Nm Size from Silicon Dioxide Surfaces. *ECS Journal of Solid State Science and Technology* **2018**, *7* (5), P243–P252. https://doi.org/10.1149/2.0131805jss.

(50) Bevilacqua, M.; Bianchini, C.; Marchionni, A.; Filippi, J.; Lavacchi, A.; Miller, H.; Oberhauser, W.; Vizza, F.; Granozzi, G.; Artiglia, L.; Annen, S. P.; Krumeich, F.; Grützmacher, H.

Improvement in the Efficiency of an OrganoMetallic Fuel Cell by Tuning the Molecular Architecture of the Anode Electrocatalyst and the Nature of the Carbon Support. *Energy Environ Sci* **2012**, *5* (9), 8608. https://doi.org/10.1039/c2ee22055e.

(51) Nguyen, T. D.; Scherer, G. G.; Xu, Z. J. A Facile Synthesis of Size-Controllable IrO2 and RuO2 Nanoparticles for the Oxygen Evolution Reaction. *Electrocatalysis* **2016**, *7* (5), 420–427. https://doi.org/10.1007/s12678-016-0321-2.

(52) Wang, T.; Xie, H.; Chen, M.; D'Aloia, A.; Cho, J.; Wu, G.; Li, Q. Precious Metal-Free Approach to Hydrogen Electrocatalysis for Energy Conversion: From Mechanism Understanding to Catalyst Design. *Nano Energy* **2017**, *42*, 69–89. https://doi.org/10.1016/j.nanoen.2017.10.045.

(53) Bellini, M.; Bevilacqua, M.; Marchionni, A.; Miller, H. A.; Filippi, J.; Grützmacher, H.; Vizza, F. Energy Production and Storage Promoted by Organometallic Complexes. *Eur J Inorg Chem* **2018**, *2018* (40), 4393–4412. https://doi.org/10.1002/ejic.201800829.

(54) Yang, X.; Gianetti, T. L.; Wörle, M. D.; van Leest, N. P.; de Bruin, B.; Grützmacher, H. A Low-Valent Dinuclear Ruthenium Diazadiene Complex Catalyzes the Oxidation of Dihydrogen and Reversible Hydrogenation of Quinones. *Chem Sci* **2019**, *10* (4), 1117–1125. https://doi.org/10.1039/C8SC02864H.

(55) Bellini, M.; Filippi, J.; Miller, H. A.; Oberhauser, W.; Vizza, F.; He, Q.; Grützmacher, H. Hydrogen and Chemicals from Renewable Alcohols by Organometallic Electroreforming. *ChemCatChem* **2017**, *9* (5), 746–750. https://doi.org/10.1002/cctc.201601427.

(56) Bellini, M.; Bevilacqua, M.; Filippi, J.; Lavacchi, A.; Marchionni, A.; Miller, H. A.; Oberhauser, W.; Vizza, F.; Annen, S. P.; Grützmacher, H. Energy and Chemicals from the Selective Electrooxidation of Renewable Diols by Organometallic Fuel Cells. *ChemSusChem* **2014**, *7* (9), 2432–2435. https://doi.org/10.1002/cssc.201402316.

(57) Annen, S. P.; Bambagioni, V.; Bevilacqua, M.; Filippi, J.; Marchionni, A.; Oberhauser, W.; Schönberg, H.; Vizza, F.; Bianchini, C.; Grützmacher, H. A Biologically Inspired Organometallic Fuel Cell (OMFC) That Converts Renewable Alcohols into Energy and Chemicals. *Angewandte Chemie International Edition* **2010**, *49* (40), 7229–7233. https://doi.org/10.1002/anie.201002234.

(58) Biesinger, M. C.; Lau, L. W. M.; Gerson, A. R.; Smart, R. St. C. The Role of the Auger Parameter in XPS Studies of Nickel Metal, Halides and Oxides. *Physical Chemistry Chemical Physics* **2012**, *14* (7), 2434. https://doi.org/10.1039/c2cp22419d.

(59) Chen, Y.-Y.; Zhang, Y.; Zhang, X.; Tang, T.; Luo, H.; Niu, S.; Dai, Z.-H.; Wan, L.-J.; Hu, J.-S. Self-Templated Fabrication of $MoNi_4/MoO_{3-x}$ Nanorod Arrays with Dual Active Components for Highly Efficient Hydrogen Evolution. *Advanced Materials* **2017**, *29* (39), 1703311. https://doi.org/10.1002/adma.201703311.

(60) Baltrusaitis, J.; Mendoza-Sanchez, B.; Fernandez, V.; Veenstra, R.; Dukstiene, N.; Roberts, A.; Fairley, N. Generalized Molybdenum Oxide Surface Chemical State XPS Determination via Informed Amorphous Sample Model. *Appl Surf Sci* **2015**, *326*, 151–161. https://doi.org/10.1016/j.apsusc.2014.11.077.

(61) Scanlon, D. O.; Watson, G. W.; Payne, D. J.; Atkinson, G. R.; Egdell, R. G.; Law, D. S. L. Theoretical and Experimental Study of the Electronic Structures of MoO_3 and MoO_2. *The*

Journal of Physical Chemistry C **2010**, *114* (10), 4636–4645. https://doi.org/10.1021/jp9093172.

(62) BARRETO, L.; MAKIHIRA, A.; RIAHI, K. The Hydrogen Economy in the 21st Century: A Sustainable Development Scenario. *Int J Hydrogen Energy* **2003**, *28* (3), 267–284. https://doi.org/10.1016/S0360-3199(02)00074-5.

(63) Sharma, S.; Ghoshal, S. K. Hydrogen the Future Transportation Fuel: From Production to Applications. *Renewable and Sustainable Energy Reviews* **2015**, *43*, 1151–1158. https://doi.org/10.1016/j.rser.2014.11.093.

(64) Shinagawa, T.; Garcia-Esparza, A. T.; Takanabe, K. Insight on Tafel Slopes from a Microkinetic Analysis of Aqueous Electrocatalysis for Energy Conversion. *Sci Rep* **2015**, *5* (1), 13801. https://doi.org/10.1038/srep13801.

(65) Cong, Y.; Yi, B.; Song, Y. Hydrogen Oxidation Reaction in Alkaline Media: From Mechanism to Recent Electrocatalysts. *Nano Energy* **2018**, *44*, 288–303. https://doi.org/10.1016/j.nanoen.2017.12.008.

(66) Rheinländer, P. J.; Herranz, J.; Durst, J.; Gasteiger, H. A. Kinetics of the Hydrogen Oxidation/Evolution Reaction on Polycrystalline Platinum in Alkaline Electrolyte Reaction Order with Respect to Hydrogen Pressure. *J Electrochem Soc* **2014**, *161* (14), F1448–F1457. https://doi.org/10.1149/2.0501414jes.

(67) Strmcnik, D.; Uchimura, M.; Wang, C.; Subbaraman, R.; Danilovic, N.; van der Vliet, D.; Paulikas, A. P.; Stamenkovic, V. R.; Markovic, N. M. Improving the Hydrogen Oxidation Reaction Rate by Promotion of Hydroxyl Adsorption. *Nat Chem* **2013**, *5* (4), 300–306. https://doi.org/10.1038/nchem.1574.

(68) Li, C.; Baek, J.-B. Recent Advances in Noble Metal (Pt, Ru, and Ir)-Based Electrocatalysts for Efficient Hydrogen Evolution Reaction. *ACS Omega* **2020**, *5* (1), 31–40. https://doi.org/10.1021/acsomega.9b03550.

(69) Gottesfeld, S.; Dekel, D. R.; Page, M.; Bae, C.; Yan, Y.; Zelenay, P.; Kim, Y. S. Anion Exchange Membrane Fuel Cells: Current Status and Remaining Challenges. *J Power Sources* **2018**, *375*, 170–184. https://doi.org/10.1016/j.jpowsour.2017.08.010.

(70) Marini, S.; Salvi, P.; Nelli, P.; Pesenti, R.; Villa, M.; Berrettoni, M.; Zangari, G.; Kiros, Y. Advanced Alkaline Water Electrolysis. *Electrochim Acta* **2012**, *82*, 384–391. https://doi.org/10.1016/j.electacta.2012.05.011.

(71) Miller, H. A.; Pagliaro, M. v.; Bellini, M.; Bartoli, F.; Wang, L.; Salam, I.; Varcoe, J. R.; Vizza, F. Integration of a Pd-CeO 2 /C Anode with Pt and Pt-Free Cathode Catalysts in High Power Density Anion Exchange Membrane Fuel Cells. *ACS Appl Energy Mater* **2020**, *3* (10), 10209–10214. https://doi.org/10.1021/acsaem.0c01998.

(72) Miller, H. A.; Bellini, M.; Dekel, D. R.; Vizza, F. Recent Developments in Pd-CeO2 Nano-Composite Electrocatalysts for Anodic Reactions in Anion Exchange Membrane Fuel Cells. *Electrochem commun* **2022**, *135*, 107219. https://doi.org/10.1016/j.elecom.2022.107219.

(73) Qin, B.; Yu, H.; Chi, J.; Jia, J.; Gao, X.; Yao, D.; Yi, B.; Shao, Z. A Novel Ir/CeO_2–C Nanoparticle Electrocatalyst for the Hydrogen Oxidation Reaction of Alkaline Anion Exchange Membrane Fuel Cells. *RSC Adv* **2017**, *7* (50), 31574–31581. https://doi.org/10.1039/C7RA03675B.

(74) Ogada, J. J.; Ipadeola, A. K.; Mwonga, P. v.; Haruna, A. B.; Nichols, F.; Chen, S.; Miller, H. A.; Pagliaro, M. v.; Vizza, F.; Varcoe, J. R.; Meira, D. M.; Wamwangi, D. M.; Ozoemena, K. I. CeO_2 Modulates the Electronic States of a Palladium Onion-Like Carbon Interface into a Highly Active and Durable Electrocatalyst for Hydrogen Oxidation in Anion-Exchange-Membrane Fuel Cells. *ACS Catal* **2022**, *12* (12), 7014–7029. https://doi.org/10.1021/acscatal.2c01863.

(75) Wang, W.; Tao, Y.; Wu, X.; Yang, L. Flower-like CeO2-Supported Small-Sized Ru Nanoparticle Hybrids for Highly Efficient Alkaline Hydrogen Evolution: Roles of Interfacial Effects. *Appl Surf Sci* **2022**, *581*, 152256. https://doi.org/10.1016/j.apsusc.2021.152256.

(76) Miller, H. A.; Vizza, F. Electrocatalysts and Mechanisms of Hydrogen Oxidation in Alkaline Media for Anion Exchange Membrane Fuel Cells; 2018; pp 79–103. https://doi.org/10.1007/978-3-319-71371-7_3.

(77) Peng, Y.; Zhang, Y.; Guo, A.; Mao, M.; Wang, Y.; Long, Y.; Fan, G. Universal Low-Temperature Oxidative Thermal Redispersion Strategy for Green and Sustainable Fabrication of Oxygen-Rich Carbons Anchored Metal Nanoparticles for Hydrogen Evolution Reactions. *Chemical Engineering Journal* **2022**, *433*, 133648. https://doi.org/10.1016/j.cej.2021.133648.

(78) Jia, N.; Martin, R. B.; Qi, Z.; Lefebvre, M. C.; Pickup, P. G. Modification of Carbon Supported Catalysts to Improve Performance in Gas Diffusion Electrodes. *Electrochim Acta* **2001**, *46* (18), 2863–2869. https://doi.org/10.1016/S0013-4686(01)00511-4.

(79) Saleh, F. S.; Easton, E. B. Assessment of the Ethanol Oxidation Activity and Durability of Pt Catalysts with or without a Carbon Support Using Electrochemical Impedance Spectroscopy. *J Power Sources* **2014**, *246*, 392–401. https://doi.org/10.1016/j.jpowsour.2013.07.109.

(80) Chae, J. E.; Lee, S. Y.; Yoo, S. J.; Kim, J. Y.; Jang, J. H.; Park, H.-Y.; Park, H. S.; Seo, B.; Henkensmeier, D.; Song, K. H.; Kim, H.-J. Polystyrene-Based Hydroxide-Ion-Conducting Ionomer: Binder Characteristics and Performance in Anion-Exchange Membrane Fuel Cells. *Polymers (Basel)* **2021**, *13* (5), 690. https://doi.org/10.3390/polym13050690.

(81) Durst, J.; Siebel, A.; Simon, C.; Hasché, F.; Herranz, J.; Gasteiger, H. A. New Insights into the Electrochemical Hydrogen Oxidation and Evolution Reaction Mechanism. *Energy Environ. Sci.* **2014**, *7* (7), 2255–2260. https://doi.org/10.1039/C4EE00440J.

(82) Mandal, M.; Huang, G.; Hassan, N. U.; Peng, X.; Gu, T.; Brooks-Starks, A. H.; Bahar, B.; Mustain, W. E.; Kohl, P. A. The Importance of Water Transport in High Conductivity and High-Power Alkaline Fuel Cells. *J Electrochem Soc* **2020**, *167* (5), 054501. https://doi.org/10.1149/2.0022005JES.

(83) Wang, Y.; Wang, G.; Li, G.; Huang, B.; Pan, J.; Liu, Q.; Han, J.; Xiao, L.; Lu, J.; Zhuang, L. Pt–Ru Catalyzed Hydrogen Oxidation in Alkaline Media: Oxophilic Effect or Electronic Effect? *Energy Environ Sci* **2015**, *8* (1), 177–181. https://doi.org/10.1039/C4EE02564D.

(84) Lu, S.; Zhuang, Z. Investigating the Influences of the Adsorbed Species on Catalytic Activity for Hydrogen Oxidation Reaction in Alkaline Electrolyte. *J Am Chem Soc* **2017**, *139* (14), 5156–5163. https://doi.org/10.1021/jacs.7b00765.

(85) Yu, H.; Davydova, E. S.; Ash, U.; Miller, H. A.; Bonville, L.; Dekel, D. R.; Maric, R. Palladium-Ceria Nanocatalyst for Hydrogen Oxidation in Alkaline Media: Optimization of the Pd–CeO2 Interface. *Nano Energy* **2019**, *57*, 820–826. https://doi.org/10.1016/j.nanoen.2018.12.098.

(86) Lima, F. H. B.; Profeti, D.; Lizcano-Valbuena, W. H.; Ticianelli, E. A.; Gonzalez, E. R. Carbon-Dispersed Pt–Rh Nanoparticles for Ethanol Electro-Oxidation. Effect of the Crystallite Size and of Temperature. *Journal of Electroanalytical Chemistry* **2008**, *617* (2), 121–129. https://doi.org/10.1016/j.jelechem.2008.01.024.

(87) Wang, Y.; Nguyen, T. S.; Liu, X.; Wang, X. Novel Palladium–Lead (Pd–Pb/C) Bimetallic Catalysts for Electrooxidation of Ethanol in Alkaline Media. *J Power Sources* **2010**, *195* (9), 2619–2622. https://doi.org/10.1016/j.jpowsour.2009.11.072.

(88) Gonçalves Biancolli, A. L.; Herranz, D.; Wang, L.; Stehlíková, G.; Bance-Soualhi, R.; Ponce-González, J.; Ocón, P.; Ticianelli, E. A.; Whelligan, D. K.; Varcoe, J. R.; Santiago, E. I. ETFE-Based Anion-Exchange Membrane Ionomer Powders for Alkaline Membrane Fuel Cells: A First Performance Comparison of Head-Group Chemistry. *J Mater Chem A Mater* **2018**, *6* (47), 24330–24341. https://doi.org/10.1039/C8TA08309F.

(89) Wang, L.; Peng, X.; Mustain, W. E.; Varcoe, J. R. Radiation-Grafted Anion-Exchange Membranes: The Switch from Low- to High-Density Polyethylene Leads to Remarkably Enhanced Fuel Cell Performance. *Energy Environ Sci* **2019**, *12* (5), 1575–1579. https://doi.org/10.1039/C9EE00331B.

(90) Jiang, L.; Hsu, A.; Chu, D.; Chen, R. Oxygen Reduction Reaction on Carbon Supported Pt and Pd in Alkaline Solutions. *J Electrochem Soc* **2009**, *156* (3), B370. https://doi.org/10.1149/1.3058586.

(91) Bellini, M.; Pagliaro, M. v.; Lenarda, A.; Fornasiero, P.; Marelli, M.; Evangelisti, C.; Innocenti, M.; Jia, Q.; Mukerjee, S.; Jankovic, J.; Wang, L.; Varcoe, J. R.; Krishnamurthy, C. B.; Grinberg, I.; Davydova, E.; Dekel, D. R.; Miller, H. A.; Vizza, F. Palladium–Ceria Catalysts with Enhanced Alkaline Hydrogen Oxidation Activity for Anion Exchange Membrane Fuel Cells. *ACS Appl Energy Mater* **2019**, *2* (7), 4999–5008. https://doi.org/10.1021/acsaem.9b00657.

(92) Thompson, S. T.; Peterson, D.; Ho, D.; Papageorgopoulos, D. Perspective—The Next Decade of AEMFCs: Near-Term Targets to Accelerate Applied R&D. *J Electrochem Soc* **2020**, *167* (8), 084514. https://doi.org/10.1149/1945-7111/ab8c88.

(93) Kleinhaus, J. T.; Wittkamp, F.; Yadav, S.; Siegmund, D.; Apfel, U.-P. [FeFe]-Hydrogenases: Maturation and Reactivity of Enzymatic Systems and Overview of Biomimetic Models. *Chem Soc Rev* **2021**, *50* (3), 1668–1784. https://doi.org/10.1039/D0CS01089H.

(94) Bigi, J. P.; Hanna, T. E.; Harman, W. H.; Chang, A.; Chang, C. J. Electrocatalytic Reduction of Protons to Hydrogen by a Water-Compatible Cobalt Polypyridyl Platform. *Chem. Commun.* **2010**, *46* (6), 958–960. https://doi.org/10.1039/B915846D.

(95) Budnikova, Y. H.; Khrizanforova, V. v. Synthetic Models of Hydrogenases Based on Framework Structures Containing Coordinating P, N-Atoms as Hydrogen Energy Electrocatalysts – from Molecules to Materials. *Pure and Applied Chemistry* **2020**, *92* (8), 1305–1320. https://doi.org/10.1515/pac-2019-1207.

(96) Ruth, J. C.; Milton, R. D.; Gu, W.; Spormann, A. M. Enhanced Electrosynthetic Hydrogen Evolution by Hydrogenases Embedded in a Redox-Active Hydrogel. *Chemistry – A European Journal* **2020**, *26* (32), 7323–7329. https://doi.org/10.1002/chem.202000750.

(97) le Goff, A.; Artero, V.; Jousselme, B.; Tran, P. D.; Guillet, N.; Métayé, R.; Fihri, A.; Palacin, S.; Fontecave, M. From Hydrogenases to Noble Metal–Free Catalytic Nanomaterials for H_2

Production and Uptake. *Science (1979)* **2009**, *326* (5958), 1384–1387. https://doi.org/10.1126/science.1179773.

(98) Ahmed, M. E.; Dey, A. Recent Developments in Bioinspired Modelling of [NiFe]- and [FeFe]-Hydrogenases. *Curr Opin Electrochem* **2019**, *15*, 155–164. https://doi.org/10.1016/j.coelec.2019.05.009.

(99) Winkler, M.; Duan, J.; Rutz, A.; Felbek, C.; Scholtysek, L.; Lampret, O.; Jaenecke, J.; Apfel, U.-P.; Gilardi, G.; Valetti, F.; Fourmond, V.; Hofmann, E.; Léger, C.; Happe, T. A Safety Cap Protects Hydrogenase from Oxygen Attack. *Nat Commun* **2021**, *12* (1), 756. https://doi.org/10.1038/s41467-020-20861-2.

(100) Pushkarev, A. S.; Pushkareva, I. v.; Solovyev, M. A.; Grigoriev, S. A.; Voloshin, Y. Z.; Chornenka, N. v.; Belov, A. S.; Millet, P.; Antuch, M.; Kalinichenko, V. N.; Dedov, A. G. Polyaromatic-Terminated Iron(Ii) Clathrochelates as Electrocatalysts for Efficient Hydrogen Production in Water Electrolysis Cells with Polymer Electrolyte Membrane. *Mendeleev Communications* **2021**, *31* (1), 20–23. https://doi.org/10.1016/j.mencom.2021.01.005.

(101) Pushkarev, A. S.; Solovyev, M. A.; Grigoriev, S. A.; Pushkareva, I. v.; Voloshin, Y. Z.; Chornenka, N. v.; Belov, A. S.; Millet, P.; Kalinichenko, V. N.; Dedov, A. G. Electrocatalytic Hydrogen Production Using the Designed Hexaphenanthrene Iron, Cobalt and Ruthenium(II) Cage Complexes as Cathode (Pre)Catalysts Immobilized on Carbonaceous Substrates. *Int J Hydrogen Energy* **2020**, *45* (49), 26206–26216. https://doi.org/10.1016/j.ijhydene.2020.02.098.

(102) Bellini, M.; Bösken, J.; Wörle, M.; Thöny, D.; Gamboa-Carballo, J. J.; Krumeich, F.; Bàrtoli, F.; Miller, H. A.; Poggini, L.; Oberhauser, W.; Lavacchi, A.; Grützmacher, H.; Vizza, F. Remarkable Stability of a Molecular Ruthenium Complex in PEM Water Electrolysis. *Chem Sci* **2022**, *13* (13), 3748–3760. https://doi.org/10.1039/D1SC07234J.

(103) Dolomanov, O. v.; Bourhis, L. J.; Gildea, R. J.; Howard, J. A. K.; Puschmann, H. *OLEX2* : A Complete Structure Solution, Refinement and Analysis Program. *J Appl Crystallogr* **2009**, *42* (2), 339–341. https://doi.org/10.1107/S0021889808042726.

(104) Sheldrick, G. M. *SHELXT* – Integrated Space-Group and Crystal-Structure Determination. *Acta Crystallogr A Found Adv* **2015**, *71* (1), 3–8. https://doi.org/10.1107/S2053273314026370.

(105) Sheldrick, G. M. A Short History of *SHELX*. *Acta Crystallogr A* **2008**, *64* (1), 112–122. https://doi.org/10.1107/S0108767307043930.

(106) Neese, F. The ORCA Program System. *WIREs Computational Molecular Science* **2012**, *2* (1), 73–78. https://doi.org/10.1002/wcms.81.

(107) Tao, J.; Perdew, J. P.; Staroverov, V. N.; Scuseria, G. E. Climbing the Density Functional Ladder: Nonempirical Meta–Generalized Gradient Approximation Designed for Molecules and Solids. *Phys Rev Lett* **2003**, *91* (14), 146401. https://doi.org/10.1103/PhysRevLett.91.146401.

(108) Weigend, F. Accurate Coulomb-Fitting Basis Sets for H to Rn. *Physical Chemistry Chemical Physics* **2006**, *8* (9), 1057. https://doi.org/10.1039/b515623h.

(109) Grimme, S.; Antony, J.; Ehrlich, S.; Krieg, H. A Consistent and Accurate *Ab Initio* Parametrization of Density Functional Dispersion Correction (DFT-D) for the 94 Elements H-Pu. *J Chem Phys* **2010**, *132* (15), 154104. https://doi.org/10.1063/1.3382344.

(110) York, D. M.; Karplus, M. A Smooth Solvation Potential Based on the Conductor-Like Screening Model. *J Phys Chem A* **1999**, *103* (50), 11060–11079. https://doi.org/10.1021/jp992097l.

(111) Barone, V.; Cossi, M. Quantum Calculation of Molecular Energies and Energy Gradients in Solution by a Conductor Solvent Model. *J Phys Chem A* **1998**, *102* (11), 1995–2001. https://doi.org/10.1021/jp9716997.

(112) Neese, F.; Wennmohs, F.; Hansen, A.; Becker, U. Efficient, Approximate and Parallel Hartree–Fock and Hybrid DFT Calculations. A 'Chain-of-Spheres' Algorithm for the Hartree–Fock Exchange. *Chem Phys* **2009**, *356* (1–3), 98–109. https://doi.org/10.1016/j.chemphys.2008.10.036.

(113) Whitten, J. L. Coulombic Potential Energy Integrals and Approximations. *J Chem Phys* **1973**, *58* (10), 4496–4501. https://doi.org/10.1063/1.1679012.

(114) Groom, C. R.; Bruno, I. J.; Lightfoot, M. P.; Ward, S. C. The Cambridge Structural Database. *Acta Crystallogr B Struct Sci Cryst Eng Mater* **2016**, *72* (2), 171–179. https://doi.org/10.1107/S2052520616003954.

(115) Hoque, M. A.; Gil-Sepulcre, M.; de Aguirre, A.; Elemans, J. A. A. W.; Moonshiram, D.; Matheu, R.; Shi, Y.; Benet-Buchholz, J.; Sala, X.; Malfois, M.; Solano, E.; Lim, J.; Garzón-Manjón, A.; Scheu, C.; Lanza, M.; Maseras, F.; Gimbert-Suriñach, C.; Llobet, A. Water Oxidation Electrocatalysis Using Ruthenium Coordination Oligomers Adsorbed on Multiwalled Carbon Nanotubes. *Nat Chem* **2020**, *12* (11), 1060–1066. https://doi.org/10.1038/s41557-020-0548-7.

(116) Brunner, F. M.; Neville, M. L.; Kubiak, C. P. Investigation of Immobilization Effects on $Ni(P_2N_2)_2$ Electrocatalysts. *Inorg Chem* **2020**, *59* (23), 16872–16881. https://doi.org/10.1021/acs.inorgchem.0c01669.

(117) Shiva Kumar, S.; Himabindu, V. Hydrogen Production by PEM Water Electrolysis – A Review. *Mater Sci Energy Technol* **2019**, *2* (3), 442–454. https://doi.org/10.1016/j.mset.2019.03.002.

(118) Elmasides, C.; Kondarides, D. I.; Grünert, W.; Verykios, X. E. XPS and FTIR Study of Ru/Al_2O_3 and Ru/TiO_2 Catalysts: Reduction Characteristics and Interaction with a Methane−Oxygen Mixture. *J Phys Chem B* **1999**, *103* (25), 5227–5239. https://doi.org/10.1021/jp9842291.

(119) Li, B.; Li, L.; Zhao, C. A Highly Stable $Ru/LaCO_3OH$ Catalyst Consisting of Support-Coated Ru Nanoparticles in Aqueous-Phase Hydrogenolysis Reactions. *Green Chemistry* **2017**, *19* (22), 5412–5421. https://doi.org/10.1039/C7GC02414B.

(120) Mazzieri, V. XPS, FTIR and TPR Characterization of Ru/Al2O3 Catalysts. *Appl Surf Sci* **2003**, *210* (3–4), 222–230. https://doi.org/10.1016/S0169-4332(03)00146-6.

(121) Morgan, D. J. Resolving Ruthenium: XPS Studies of Common Ruthenium Materials. *Surface and Interface Analysis* **2015**, *47* (11), 1072–1079. https://doi.org/10.1002/sia.5852.

(122) Rodríguez-Lugo, R. E.; Trincado, M.; Vogt, M.; Tewes, F.; Santiso-Quinones, G.; Grützmacher, H. A Homogeneous Transition Metal Complex for Clean Hydrogen Production from Methanol–Water Mixtures. *Nat Chem* **2013**, *5* (4), 342–347. https://doi.org/10.1038/nchem.1595.

(123) Ayers, K. The Potential of Proton Exchange Membrane–Based Electrolysis Technology. *Curr Opin Electrochem* **2019**, *18*, 9–15. https://doi.org/10.1016/j.coelec.2019.08.008.

(124) Zhang, B.; Fan, L.; Ambre, R. B.; Liu, T.; Meng, Q.; Timmer, B. J. J.; Sun, L. Advancing Proton Exchange Membrane Electrolysers with Molecular Catalysts. *Joule* **2020**, *4* (7), 1408–1444. https://doi.org/10.1016/j.joule.2020.06.001.

(125) Staffell, I.; Scamman, D.; Velazquez Abad, A.; Balcombe, P.; Dodds, P. E.; Ekins, P.; Shah, N.; Ward, K. R. The Role of Hydrogen and Fuel Cells in the Global Energy System. *Energy Environ Sci* **2019**, *12* (2), 463–491. https://doi.org/10.1039/C8EE01157E.

(126) Andrews, J.; Shabani, B. Re-Envisioning the Role of Hydrogen in a Sustainable Energy Economy. *Int J Hydrogen Energy* **2012**, *37* (2), 1184–1203. https://doi.org/10.1016/j.ijhydene.2011.09.137.

(127) Apostolou, D.; Enevoldsen, P.; Xydis, G. Supporting Green Urban Mobility – The Case of a Small-Scale Autonomous Hydrogen Refuelling Station. *Int J Hydrogen Energy* **2019**, *44* (20), 9675–9689. https://doi.org/10.1016/j.ijhydene.2018.11.197.

(128) Proost, J. State-of-the Art CAPEX Data for Water Electrolysers, and Their Impact on Renewable Hydrogen Price Settings. *Int J Hydrogen Energy* **2019**, *44* (9), 4406–4413. https://doi.org/10.1016/j.ijhydene.2018.07.164.

(129) SCHOOTS, K.; FERIOLI, F.; KRAMER, G.; VANDERZWAAN, B. Learning Curves for Hydrogen Production Technology: An Assessment of Observed Cost Reductions. *Int J Hydrogen Energy* **2008**, *33* (11), 2630–2645. https://doi.org/10.1016/j.ijhydene.2008.03.011.

(130) Sabihuddin, S.; Kiprakis, A.; Mueller, M. A Numerical and Graphical Review of Energy Storage Technologies. *Energies (Basel)* **2014**, *8* (1), 172–216. https://doi.org/10.3390/en8010172.

(131) Carmo, M.; Fritz, D. L.; Mergel, J.; Stolten, D. A Comprehensive Review on PEM Water Electrolysis. *Int J Hydrogen Energy* **2013**, *38* (12), 4901–4934. https://doi.org/10.1016/j.ijhydene.2013.01.151.

(132) Saba, S. M.; Müller, M.; Robinius, M.; Stolten, D. The Investment Costs of Electrolysis – A Comparison of Cost Studies from the Past 30 Years. *Int J Hydrogen Energy* **2018**, *43* (3), 1209–1223. https://doi.org/10.1016/j.ijhydene.2017.11.115.

(133) Schmidt, O.; Gambhir, A.; Staffell, I.; Hawkes, A.; Nelson, J.; Few, S. Future Cost and Performance of Water Electrolysis: An Expert Elicitation Study. *Int J Hydrogen Energy* **2017**, *42* (52), 30470–30492. https://doi.org/10.1016/j.ijhydene.2017.10.045.

(134) Ayers, K. E.; Anderson, E. B.; Capuano, C.; Carter, B.; Dalton, L.; Hanlon, G.; Manco, J.; Niedzwiecki, M. Research Advances towards Low Cost, High Efficiency PEM Electrolysis. *ECS Trans* **2010**, *33* (1), 3–15. https://doi.org/10.1149/1.3484496.

(135) Miller, H. A.; Bouzek, K.; Hnat, J.; Loos, S.; Bernäcker, C. I.; Weißgärber, T.; Röntzsch, L.; Meier-Haack, J. Green Hydrogen from Anion Exchange Membrane Water Electrolysis: A Review of Recent Developments in Critical Materials and Operating Conditions. *Sustain Energy Fuels* **2020**, *4* (5), 2114–2133. https://doi.org/10.1039/C9SE01240K.

(136) Grigoriev, S. A.; Fateev, V. N.; Bessarabov, D. G.; Millet, P. Current Status, Research Trends, and Challenges in Water Electrolysis Science and Technology. *Int J Hydrogen Energy* **2020**, *45* (49), 26036–26058. https://doi.org/10.1016/j.ijhydene.2020.03.109.

(137) Lindquist, G. A.; Oener, S. Z.; Krivina, R.; Motz, A. R.; Keane, A.; Capuano, C.; Ayers, K. E.; Boettcher, S. W. Performance and Durability of Pure-Water-Fed Anion Exchange Membrane

Electrolysers Using Baseline Materials and Operation. *ACS Appl Mater Interfaces* **2021**, *13* (44), 51917–51924. https://doi.org/10.1021/acsami.1c06053.

(138) Chen, N.; Paek, S. Y.; Lee, J. Y.; Park, J. H.; Lee, S. Y.; Lee, Y. M. High-Performance Anion Exchange Membrane Water Electrolysers with a Current Density of 7.68 A Cm $^{-2}$ and a Durability of 1000 Hours. *Energy Environ Sci* **2021**, *14* (12), 6338–6348. https://doi.org/10.1039/D1EE02642A.

(139) Chen, P.; Hu, X. High-Efficiency Anion Exchange Membrane Water Electrolysis Employing Non-Noble Metal Catalysts. *Adv Energy Mater* **2020**, *10* (39), 2002285. https://doi.org/10.1002/aenm.202002285.

(140) Yang, Y.; Peltier, C. R.; Zeng, R.; Schimmenti, R.; Li, Q.; Huang, X.; Yan, Z.; Potsi, G.; Selhorst, R.; Lu, X.; Xu, W.; Tader, M.; Soudackov, A. v.; Zhang, H.; Krumov, M.; Murray, E.; Xu, P.; Hitt, J.; Xu, L.; Ko, H.-Y.; Ernst, B. G.; Bundschu, C.; Luo, A.; Markovich, D.; Hu, M.; He, C.; Wang, H.; Fang, J.; DiStasio, R. A.; Kourkoutis, L. F.; Singer, A.; Noonan, K. J. T.; Xiao, L.; Zhuang, L.; Pivovar, B. S.; Zelenay, P.; Herrero, E.; Feliu, J. M.; Suntivich, J.; Giannelis, E. P.; Hammes-Schiffer, S.; Arias, T.; Mavrikakis, M.; Mallouk, T. E.; Brock, J. D.; Muller, D. A.; DiSalvo, F. J.; Coates, G. W.; Abruña, H. D. Electrocatalysis in Alkaline Media and Alkaline Membrane-Based Energy Technologies. *Chem Rev* **2022**, *122* (6), 6117–6321. https://doi.org/10.1021/acs.chemrev.1c00331.

(141) Schalenbach, M.; Speck, F. D.; Ledendecker, M.; Kasian, O.; Goehl, D.; Mingers, A. M.; Breitbach, B.; Springer, H.; Cherevko, S.; Mayrhofer, K. J. J. Nickel-Molybdenum Alloy Catalysts for the Hydrogen Evolution Reaction: Activity and Stability Revised. *Electrochim Acta* **2018**, *259*, 1154–1161. https://doi.org/10.1016/j.electacta.2017.11.069.

(142) Hnát, J.; Plevová, M.; Žitka, J.; Paidar, M.; Bouzek, K. Anion-Selective Materials with 1,4-Diazabicyclo[2.2.2]Octane Functional Groups for Advanced Alkaline Water Electrolysis. *Electrochim Acta* **2017**, *248*, 547–555. https://doi.org/10.1016/j.electacta.2017.07.165.

(143) Girault, P.; Grosseau-Poussard, J. L.; Dinhut, J. F.; Marechal, L. Influence of a Chromium Ion Implantation on the Passive Behaviour of Nickel in Artificial Sea-Water: An EIS and XPS Study. *Nucl Instrum Methods Phys Res B* **2001**, *174* (4), 439–452. https://doi.org/10.1016/S0168-583X(00)00686-8.

(144) Lasia, A. Modeling of Impedance of Porous Electrodes; 2008; pp 1–71. https://doi.org/10.1007/978-0-387-49582-8_3.

(145) Hnát, J.; Kodým, R.; Denk, K.; Paidar, M.; Žitka, J.; Bouzek, K. Design of a Zero-Gap Laboratory-Scale Polymer Electrolyte Membrane Alkaline Water Electrolysis Stack. *Chemie Ingenieur Technik* **2019**, *91* (6), 821–832. https://doi.org/10.1002/cite.201800185.

(146) Krstajić, N.; Popović, M.; Grgur, B.; Vojnović, M.; Šepa, D. On the Kinetics of the Hydrogen Evolution Reaction on Nickel in Alkaline Solution. *Journal of Electroanalytical Chemistry* **2001**, *512* (1–2), 16–26. https://doi.org/10.1016/S0022-0728(01)00590-3.

(147) Zschech, E.; Topal, E.; Kutukova, K.; Gluch, J.; Löffler, M.; Werner, S.; Guttmann, P.; Schneider, G.; Liao, Z.; Timoshenko, J. Multi-Scale Microscopy Study of 3D Morphology and Structure of MoNi4/MoO2@Ni Electrocatalytic Systems for Fast Water Dissociation. *Micron* **2022**, *158*, 103262. https://doi.org/10.1016/j.micron.2022.103262.

(148) Zhang, J.; Wang, T.; Liu, P.; Liao, Z.; Liu, S.; Zhuang, X.; Chen, M.; Zschech, E.; Feng, X. Efficient Hydrogen Production on MoNi4 Electrocatalysts with Fast Water Dissociation Kinetics. *Nat Commun* **2017**, *8* (1), 15437. https://doi.org/10.1038/ncomms15437.

(149) Jin, Y.; Shen, P. K. Nanoflower-like Metallic Conductive MoO_2 as a High-Performance Non-Precious Metal Electrocatalyst for the Hydrogen Evolution Reaction. *J Mater Chem A Mater* **2015**, *3* (40), 20080–20085. https://doi.org/10.1039/C5TA06018D.

(150) Horkans, J.; Shafer, M. W. An Investigation of the Electrochemistry of a Series of Metal Dioxides with Rutile-Type Structure: MoO2, WO 2, ReO2, RuO2, OsO2, and IrO2. *J Electrochem Soc* **1977**, *124* (8), 1202–1207. https://doi.org/10.1149/1.2133528.

(151) Yang, T.; Xu, Y.; Lv, H.; Wang, M.; Cui, X.; Liu, G.; Jiang, L. Triggering the Intrinsic Catalytic Activity of Ni-Doped Molybdenum Oxides via Phase Engineering for Hydrogen Evolution and Application in Mg/Seawater Batteries. *ACS Sustain Chem Eng* **2021**, *9* (38), 13106–13113. https://doi.org/10.1021/acssuschemeng.1c05184.

(152) Liu, X.; Ni, K.; Niu, C.; Guo, R.; Xi, W.; Wang, Z.; Meng, J.; Li, J.; Zhu, Y.; Wu, P.; Li, Q.; Luo, J.; Wu, X.; Mai, L. Upraising the O 2p Orbital by Integrating Ni with MoO_2 for Accelerating Hydrogen Evolution Kinetics. *ACS Catal* **2019**, *9* (3), 2275–2285. https://doi.org/10.1021/acscatal.8b04817.

(153) Bau, J. A.; Kozlov, S. M.; Azofra, L. M.; Ould-Chikh, S.; Emwas, A.-H.; Idriss, H.; Cavallo, L.; Takanabe, K. Role of Oxidized Mo Species on the Active Surface of Ni–Mo Electrocatalysts for Hydrogen Evolution under Alkaline Conditions. *ACS Catal* **2020**, *10* (21), 12858–12866. https://doi.org/10.1021/acscatal.0c02743.

(154) He, B.; Liu, F.; Liu, Y.; Yan, S. Development of G-C3N4 Activated Hollow Carbon Spheres with Good Performance for Oxygen Reduction and Selective Capture of Acid Gases. *Electrochim Acta* **2019**, *324*, 134869. https://doi.org/10.1016/j.electacta.2019.134869.

Acknowledgments

I wish to thank the Institute of Chemistry of the Organometallic Compounds (ICCOM) of the National Research Council of Florence where I had the opportunity to experience. I would like to express my sincere gratitude to my tutor and director of the Institute Dr. Francesco Vizza, who gave me the opportunity to join his research group and carry out my thesis work.

I am thankful to my other tutor and scientific advisor, Dr. Hamish Miller, for the continuous support during my Ph.D and related research, for his patience and help in these three years of research and in writing this thesis. A special mention to my colleagues Marco Bellini and Maria Pagliaro who always helped me and have always been kind to me. I express the same feelings to all my colleagues and co-workers of the research group, Dr. Andrea Marchionni, Dr. Jonathan Filippi, Dr. Werner Oberhauser.

I also thank all the people in Helmholtz Institute Erlangen-Nürnberg (HI-ERN), for their help during my stay in Germany. Danke schön!

Finally, I would like to thank all my friends and my family, for their continued support over the years.